Tidal flat landscape formation and evolution

Summary

Tidal flat landscape formation and evolution are closely related to the biotic and abiotic processes that take place in the intertidal environments. Extensive studies have been carried out on the relevant agents such as hydrodynamics, sediment transport and the related ecosystem (vegetation and benthic communities) dynamics. However, the feedback mechanism among multiple agents is complex and many key aspects are currently understudied. In times of accelerating global change, knowledge of the mechanisms that drive tidal flat evolution is of great importance to ecosystem conservation and restoration. This thesis addresses the currently understudied subjects related to intertidal hydrodynamic processes as well as the intertidal landscape developments, which are of great economic and ecological importance.

Tidal flat landscape formation and evolution

Zhan Hu

胡 湛

Tidal flat landscape formation and evolution

Proefschrift

ter verkrijging van de graad van doctor

aan de Technische Universiteit Delft,

op gezag van de Rector Magnificus Prof. ir. K.C.A.M. Luyben,

voorzitter van het College voor Promoties,

in het openbaar te verdedigen op Maandag 8 juni 2015 10.00 uur

door

Zhan HU

Bachelor in Hydraulic Engineering, Hohai University, China

geboren te Xianfeng, China

This dissertation has been approved by the:

Promotors: Prof.dr.ir. M.J.F. Stive

Prof.dr. T.J. Bouma

Prof.dr.ir. Z.B. Wang

Composition of the doctoral committee:

Rector Magnificus

Prof.dr.ir. M.J.F. Stive	TU Delft, promotor
Prof.dr. T.J. Bouma	RU Groningen/ NIOZ, promotor
Prof.dr.ir. Z.B. Wang	TU Delft/ Deltares, promotor

Independent members:

Prof.dr.ir. J.C. Winterwerp	TU Delft/ Deltares
Prof.dr.ir. A.J.H.M. Reniers	TU Delft
Prof.dr. S. Temmerman	University of Antwerp, Belgium
Dr.ir. M. Zijlema	TU Delft

substitute member:

Prof.dr.ir. A.W. Heemink	TU Delft

Abstract

Tidal flat landscape formation and evolution are closely related to the biotic and abiotic processes that take place in the intertidal environments. Extensive studies have been carried out on the relevant agents such as hydrodynamics, sediment transport and the related ecosystem (vegetation and benthic communities) dynamics. However, the feedback mechanism among multiple agents is complex and a great number of its key aspects are currently understudied. In times of accelerating global change, fundamental knowledge of the mechanisms that drive tidal flat evolution is of great importance to ecosystem conservation and restoration.

Wave damping by vegetation in coastal wetlands is one of the most relevant and interesting study fields. This topic has gained a lot of attention because of the potential value of applying vegetated wetlands for coastal protection. Recent studies have shown that saltmarsh plants are effective in dissipating wave energy, even under storm surge conditions. However, this dissipation process is still not well understood due to the complex water motion inside vegetation structures. For instance, wave dissipation by vegetation in combined current and wave flows is not well studied. Most studies ignored the effect of tidal currents on wave attenuation and two existing studies have drawn contradictive conclusions as to whether tidal currents enhance or suppress wave dissipation. The effect of tidal currents can be important as it may influence the effectiveness of using vegetated areas for coastal defence. To gain insights into the role of tidal currents in vegetation induced wave dissipation, a flume experiment has been conducted to quantify wave dissipation in a mimicked vegetation patch with and without following currents (i.e. current velocity in the same direction as the wave propagation) (Chapter 2). It is found that the wave damping capacity of the tested mimics can be either enhanced or suppressed by the presence of following currents, depending on the ratio between the imposed current velocity and the horizontal component of the wave orbital velocity amplitude. Furthermore, we applied a unique method to measure the vegetation drag coefficient in pure wave and in combined current-wave conditions. One result is an empirical relation between the drag coefficient and the Reynolds number, which can be useful to numerical modelling. Finally, an analytical model was formulated to explain the effect of following currents in wave dissipation by integrating the insights gained in drag coefficient and in-canopy velocity observations.

Saltmarsh and mangrove ecosystems establishment is another important aspect related to intertidal landscape development. There is growing evidence that hydrodynamic processes play an important role in vegetation development patterns. However, the insight into the governing processes is still insufficient, which hinders the success of conservation and restoration of such coastal wetlands. To explicitly include the vegetation establishment processes and the role of hydrodynamics in them, a saltmarsh establishment model was formulated based on the 'Window of Opportunity' (WoO) concept (Chapter 3). This concept illustrates that successful seedling establishment, following initial settlement, requires a sufficiently long period (as a WoO) with limited physical disturbance. By quantifying the occurrence of a WoO, we may explain observed marsh establishment patterns. The original WoO approach considers tidal inundation as the only disturbance to the marsh establishment, whereas disturbance from other hydrodynamic forcing was excluded. To evaluate the importance of hydrodynamic forcing as disturbance to the marsh colonization, two saltmarsh establishment models have been formulated. In one model, the spatial and temporal variations in hydrodynamic forcing are taken into account, whereas the other saltmarsh establishment model has been built based on the original WoO framework, i.e. excluding the disturbance from hydrodynamic forcing. These two models are tested against the data from a monitored marsh area in the Westerschelde Estuary, the Netherlands. The results show that the model including hydrodynamic forcing has a higher prediction accuracy of saltmarsh establishment in space and in time than the other model, thus highlighting the importance of hydrodynamic forcing in saltmarsh formation. Furthermore, this model is used to predict the extent of saltmarsh establishment on schematized tidal flats. The prediction shows that tidal flat morphology can significantly influence the elevation range and the corresponding width for saltmarsh establishment in an intertidal environment,, which provides suggestions for saltmarsh management.

Continuously changing hydrodynamics induce short-term (daily) bed-level changes on the tidal flats. Observing these bed-level changes is the key to pinpointing the effect of changing hydrodynamics and to understand their role in sediment transport and related ecological processes. However, conventional manual bed-elevation measurements tend to be discontinuous, due to the labor involved, and are not efficient for high frequency monitoring. The existing automated methods for continuous monitoring are either too expensive to allow spatial applications with multiple units or they are not accurate enough. In light of this, a novel instrument, called the SED-sensor (Surface Elevation Dynamics sensor), is developed to provide continuous monitoring with a high vertical resolution (2 mm) (Chapter 4). The sensors are

designed as stand-alone units. This excludes the need for external data logging and power supply, which reduces production and operation cost. Good agreement is obtained by comparing the SED-sensor measurement with precise manual measurements using Sedimentation Erosion Bars. Moreover, the data collected by SED-sensors at two contrasting sites demonstrates how these instruments can be used for monitoring short-term bed-level dynamics and pinpointing the effect of changing hydrodynamic forcing herein.

In Chapter 5, the effect of changing hydrodynamic forcing on tidal flat morphology is systematically explained by a model based on a dynamic equilibrium theory. The essence of this theory is the assumption that a uniform bed shear stress distribution on tidal flats leads to a morphologic equilibrium. On real tidal flats, however, the hydrodynamic forces vary continuously, both in space and in time. Hence, the theoretical equilibrium is never achieved. It is not clear how this theory can be applied for realistic morphodynamic predictions with varying forces. In light of this, a morphological model has been formulated based on the dynamic equilibrium theory and its core assumption with uniform bed shear stress. Other than the original static equilibrium model, this model explicitly accounts for the spatiotemporal variations in hydrodynamic forcing. The long-term morphological predictions of this model have been compared qualitatively with previous process-based models. The short-term morphodynamic predictions were evaluated quantitatively against measurements (by SED-sensors) along a tidal flat cross-section in the Westerschelde Estuary. The good model performance indicates the usefulness of the model and the validity of the dynamic equilibrium theory under realistic forcing conditions.

This thesis addresses the currently understudied subjects related to intertidal hydrodynamic processes as well as the intertidal landscape developments, which are of great economic and ecological importance. The insights and findings gathered in this thesis may improve: 1) estimation of wave dissipation capacity in coastal wetlands; 2) understanding the spatial and temporal patterns of saltmarsh establishment; 3) monitoring bed-level changes on tidal flats; 4) predicting long-term and short-term tidal flat morphodynamic evolutions. Finally, recommendations for intertidal ecosystem management strategies and further research are given at the end of this thesis.

Samenvatting

De vorming en ontwikkeling van schorren en slikken zijn nauw verbonden met de biotische en abiotische processen die in het intergetijdengebied plaats vinden. Belangrijke processen, zoals hydrodynamische processen, sediment transport en vestiging en ontwikkeling van een ecosysteem (vegetatie en bentische gemeenschappen), zijn uitgebreid bestudeerd. De terugkoppeling tussen processen is echter complex en vele dominante aspecten daarvan zijn vooralsnog onvoldoende bestudeerd. In tijden van steeds snellere globale veranderingen, is diepgaande kennis van de mechanismes die de ontwikkeling van schorren en slikken bepalen van groot belang voor behoud en herstel van het ecosysteem.

Golfdemping door vegetatie in ondiepe kustgebieden is één van de meest relevante en interessante onderwerpen van onderzoek en krijgt steeds meer aandacht vanwege de potentie van begroeiing van deze gebieden voor bescherming van de kust. Recente studies hebben aangetoond dat, ook tijdens stormcondities, planten op schorren golfenergie effectief kunnen dissiperen. Het verband tussen dit proces en de complexe beweging van het water binnen de vegetatie is echter niet geheel duidelijk. Zo is golfdemping door vegetatie bij een combinatie van golven en stroming niet goed bestudeerd. In de meeste studies blijft het effect van de getijstroming op golfdemping achterwege en twee bestaande studies spreken elkaar tegen in de conclusie of golfdemping door stroming wordt versterkt of juist onderdrukt. Het effect van getijstroming kan van belang zijn waar het van invloed is op de effectiviteit van het gebruik van vegetatie als kustbescherming. Om inzicht te krijgen in de rol van getijstroming in golfdemping door vegetatie, is een experiment uitgevoerd in een laboratoriumgoot met nagebootste vegetatie, met en zonder stroming in de richting van golfvoortplanting (Hoofdstuk 2). Gebleken is dat de golfdempende capaciteit van de nagebootste vegetatie zowel kan toenemen als verminderen door de aanwezigheid van stromingen met de golf mee, afhankelijk van de verhouding tussen de toegepaste stroomsnelheid en de amplitude van de horizontale component van de orbitaalsnelheid van de golven. Tevens hebben we een unieke methode toegepast om de sleep-coëfficiënt van de vegetatie te meten bij alleen golven en bij een combinatie van golven en stroming. Een van de resultaten is een empirische relatie tussen de sleep-coëfficiënt en het Reynolds getal. Dat kan nuttig zijn voor numerieke modellering. Tenslotte is een analytisch model geformuleerd om het effect op golfdemping te verklaren van de stroming met de golf mee door het verkregen inzicht in de sleep-coëfficiënt te integreren met waarnemingen aan de stroomsnelheid binnen de vegetatie.

De vorming van een ecosysteem van schorren of mangroves is een ander belangrijk aspect van de ontwikkeling van het intergetijdengebied.. Er zijn steeds meer aanwijzingen, dat hydrodynamische processen een belangrijke rol spelen bij ontwikkeling van vegetatie. Er is echter onvoldoende inzicht in de dominante processen en dit vormt een belemmering voor het succes van behoud en herstel van zulke kustgebieden.

Om het proces van vestiging van vegetatie en de rol van waterbeweging daarbij expliciet in rekening te kunnen brengen, is een model voor het ontstaan van schorren geformuleerd op basis van het "Window of Opportunity" (WoO) concept. (hoofdstuk 3). Dit concept houdt in dat voor een succesvolle vestiging van zaailingen een voldoende lange periode van rust (als een 'WoO') en zo min mogelijk fysieke verstoring noodzakelijk is. Door het bestaan van een 'WoO' te kwantificeren, kunnen we waargenomen patronen in de vorming van schorren mogelijk verklaren. In de oorspronkelijke 'WoO' methode is overstroming door het getij de enige verstoring bij de vorming van schorren. Verstoringen door andere hydrodynamische forcering zijn uitgesloten. Om het belang van hydrodynamische forcering als verstoring van de kolonisatie van slikken te evalueren, zijn twee modellen voor de ontwikkeling van schorren geformuleerd. In het ene model worden variaties in hydrodynamische forcering met de tijd meegenomen, terwijl het andere model voor de ontwikkeling van schorren uitgaat van de oorspronkelijke WoO aanpak zonder verstoring door hydrodynamische forcering. Deze twee modellen zijn getoetst aan waarnemingen van een schorrengebied in de Westerschelde in Nederland. Uit de resultaten blijkt dat het model met hydrodynamische forceringen de groei van schorren in ruimte en tijd nauwkeuriger voorspelt dan het andere model. Dit resultaat benadrukt het belang van de hydrodynamische forcering bij de vorming van schorren. Dit model is bovendien gebruikt om de mate van groei van schorren op slikken met een geschematiseerde vorm te voorspellen. De voorspelling laat ziet dat de morfologie van slikken een significante invloed kan hebben op de hoogte waarop nieuwe schorren worden gevormd en op de breedte waarover dit gebeurt in een intergetijdengebied. Suggesties voor het beheer van schorren kunnen hieruit afgeleid worden.

Voortdurend veranderende hydrodynamische processen veroorzaken op korte termijn (dagelijkse) veranderingen in het bodemniveau van slikken. Waarneming van deze veranderingen in het niveau van de bodem vormt de sleutel tot het duiden van het effect van veranderende hydrodynamische processen en in het begrijpen van sediment transport en daaraan gerelateerde ecologische processen. Conventionele handmatige meting van het bodemniveau is echter arbeidsintensief en vaak niet continu. Het is daarom niet geschikt voor hoogfrequente meting.

Bestaande geautomatiseerde methoden voor continue meting zijn, of te duur voor ruimtelijke toepassingen met meerdere instrumenten, of ze zijn niet nauwkeurig genoeg. Met het oog hierop is een nieuw instrument ontwikkeld, de SED-sensor ("Surface Elevation Dynamics" sensor), voor continue meting met een hoge verticale resolutie (2 mm) (hoofdstuk 4). De sensoren zijn ontworpen als autonome eenheden. Hierdoor is geen externe gegevensregistratie en elektriciteitstoevoer nodig, waardoor kosten voor productie en exploitatie beperkt blijven. Metingen met de SED-sensor blijken goed overeen te komen met nauwkeurige handmatige metingen met behulp van een peilstok ("Sedimentation Erosion Bars"). Bovendien laten metingen met SED-sensoren op twee contrasterende locaties zien hoe deze instrumenten kunnen worden gebruikt voor het registreren van de korte-termijn dynamiek van de bodem en tevens het vaststellen van de rol die veranderende hydrodynamische forceringen hierin spelen.

In hoofdstuk 5 wordt het effect van veranderende hydrodynamische forceringen op de morfologie van slikken systematisch verklaard door een model dat gebaseerd is op een theorie van dynamisch evenwicht. Centraal in deze theorie staat de aanname dat een uniforme verdeling van de bodemschuifspanning op slikken leidt tot een morfologisch evenwicht. Echter, in werkelijkheid variëren de hydrodynamische condities op slikken continu, zowel in tijd als in ruimte. Vandaar dat het theoretisch evenwicht nooit wordt bereikt. Het is niet duidelijk hoe deze theorie toegepast kan worden om realistische morfodynamische voorspellingen te maken met variabele forcering. In het licht hiervan is een morfologisch model geformuleerd op basis van de dynamische evenwichtstheorie en de bijbehorende essentiële vooronderstelling. Anders dan in het originele stationaire evenwichtsmodel, houdt dit model expliciet rekening met de ruimtelijke en temporele variaties van de hydrodynamische forcering. De lange termijn morfologische voorspellingen van dit model zijn kwalitatief vergeleken met eerdere procesgebaseerde modellen. De lange-termijn morfodynamische voorspellingen zijn kwantitatief vergeleken met de metingen (met SED-sensoren) in een dwarsdoorsnede van een slik in de Westerschelde. De goede prestatie van het model toont het nut van het model en van de geldigheid van de dynamische evenwichtstheorie onder realistische omstandigheden aan.

Dit proefschrift gaat in op vooralsnog onvoldoende bestudeerde onderwerpen die gerelateerd zijn aan hydrodynamische processen en de verwante landschapsdynamiek van het intergetijdengebied, die van groot economisch en ecologisch belang zijn. De inzichten en bevindingen die in dit proefschrift verzameld zijn, kunnen leiden tot een verbetering van: 1) de schatting van het golfdempend vermogen van schorren, 2) begrip en inzicht in patronen van vorming

van schorren, in ruimte en tijd , 3) het meten van veranderingen van het bodemniveau van slikken, en 4) het voorspellen van lang- en kort termijn morfodynamisch gedrag van slikken. Tot slot worden aan het einde van dit proefschrift aanbevelingen gedaan voor strategieën voor het beheer van ecosystemen en voor nader onderzoek.

This samenvatting was translated by Mariette van Tilburg and Tjerk Zitman.

Contents

Chapter 1

Introduction

1.1 Context

Tidal flat and hydrodynamic forces

Tidal flats are often found in bays, bayous, lagoons, and estuaries. They are flooded by tide on a daily basis. The upper part of tidal flats is often occupied by mature salt marshes or mangroves forests. On the seaward side of the persistent vegetation areas, there often is a pioneer area for new vegetation colonization. The lower tidal flat generally remains 'bare' in that it is unvegetated, but contains benthic fauna buried in the sediment (Figure 1.1). The landward and seaward boundary of tidal flats is often a sea dike for flood defense and a tidal channel for navigation, respectively.
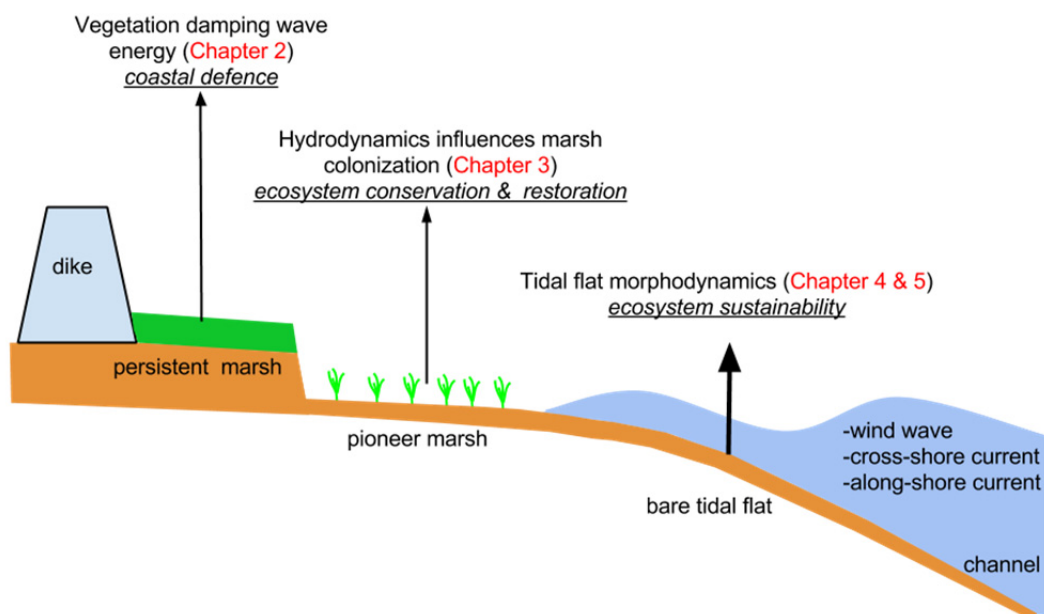
Figure 1.1 schematized tidal flat and thesis outline. The text above the vertical arrows states the subject and the significance (underlined) of each chapter.

Intertidal habitats are of great ecological importance as they host numerous species of vegetation and wildlife (Costanza et al., 1997; Martínez et al., 2007). They are also of high economic importance, as vegetated intertidal areas can stabilize shorelines and provide protection for large coastal populations (Barbier et al., 2008; Borsje et al., 2011; Bouma et al., 2014; Temmerman et al., 2013). Because of the numerous ecosystem services (supporting, provisioning, regulating and cultural) provided by tidal flats, they are very valuable to coastal communities (Barbier et al., 2008).

In the intertidal environment, hydrodynamic forcing is an important physical driver, which shapes the tidal flat morphology and participates in relevant ecological processes (Roberts et al., 2000; Balke et al., 2014, 2013b; Bouma et al., 2001). The main hydrodynamic forces experienced by tidal flats are: 1) the tide; 2) the wind waves; 3) the wind-induced circulation; 4) the density-driven circulation; 5) the surficial drainage process (Eisma, 1998; Le Hir et al., 2000). The hydrodynamics on tidal flats can be complex. In this study, we mainly focus on the forces induced by tidal currents and wind waves, which are the two primary mechanisms related to sediment dynamics and ecological processes.

Coastal protection value of vegetated wetlands

Figure 1.2 Wave propagation in a saltmarsh field, image from NOAA

Coastal population has been growing over the last few decades and such a trend is expected to continue in the future (Small and Nicholls, 2003). In the era of climate changes with increasing sea level rise and storminess (Woodruff et al., 2013; Donat et al., 2011), the large coastal communities are facing increasing risk of flood disasters. For effective and sustainable coastal protections, it has been proposed to integrate vegetated wetlands as a part of the protection

scheme, as natural saltmarshes and mangrove forests are now recognized as potential barriers to erosive hydrodynamic forces (Barbier et al., 2008; Temmerman et al., 2013). Even under storm surge conditions, saltmarsh canopies have shown their effectiveness in attenuating wave energy (Pinsky et al., 2013; Möller et al., 2014).

Recently, a 'Building with Nature' program has been initiated in the Netherlands (Waterman et al., 2010; van Slobbe et al., 2013). Pilot coastal protection projects in sandy and muddy environments have been carried out. These projects have attracted attention from both research and social communities (for details www. Ecoshape.nl). The core philosophy of Building with Nature is to create a win-win situation that benefits both ecosystem sustainability and infrastructure development (e.g. cost-effective defense) (Waterman et al., 2010; Temmerman et al., 2013). Integrating saltmarshes into general coastal protection schemes is well in-line with the 'Building with Nature' philosophy, which implies that we can provide an alternative coastal protection measure by preserving coastal ecosystems.

Coastal wetlands conservation and restoration

Despite the importance of intertidal wetlands, 25-50% of the world wetland area has been lost due to direct human conversion for economic development (Pendleton et al., 2012; Kirwan and Megonigal, 2013; Ma et al., 2014). Apart from the direct losses, intertidal habitats also face long-term loss due to climate changes, e.g. sea level rise and the associated 'coastal squeeze' effect (Kirwan and Temmerman, 2009; Doody, 2004). 'Coastal squeeze' can arise in coastal wetlands when the high water mark is fixed by dikes and the low water mark migrates landwards in response to sea level rise (Pontee, 2013). Finally, coastal wetlands may also become starved of sediment caused by dam construction in major rivers (Yang et al., 2006). Due to the area decline, tidal flat ecosystem services can be substantially compromised.

There is a growing need to preserve and restore coastal ecosystems. For saltmarsh systems, common practice for restoration is de-embankment of the previously reclaimed land (Bakker et al., 2002; Wolters et al., 2008). However, the marsh restoration projects at many sites are considered not very successful as they generally contain less than 50% of the target species (Wolters et al., 2005). For mangrove restoration, attempts have been made to plant mangrove propagules in reserved rehabilitation areas (Ellison, 2000; Lewis III, 2005; Primavera and Esteban, 2008). However, those attempts often had little success. For instance, the survival

rates of the planted mangroves in Philippines were only 10–20 %, which lead to substantial investment losses (Primavera and Esteban, 2008).

Tidal flat morphodynamics

Long-term stability of coastal wetlands is related to the overall morphological development of both vegetated and bare tidal flats (van de Koppel et al., 2005; Mariotti and Fagherazzi, 2010). The morphology of intertidal areas is constantly reworked by the hydrodynamic forces (Friedrichs, 2011; Green and Coco, 2014), and further influenced by many other factors such as: external sediment supply and biostabilisation/bioturbation (Murray et al., 2008; Corenblit et al., 2011; Passarelli et al., 2014).

Saltmarshes carry a clear imprint of biogeomorphic feedback mechanism: marsh vegetation mitigates hydrodynamic forces, and helps to stabilize the seabed and promote sedimentation; the damped hydrodynamic forces and stabilized seabed in turn benefit marsh developments (see Fagherazzi et al., 2012 for a review). This positive feedback between biological and physical processes plays a key role in the marsh system persistence and its landscape evolution. In vertical direction, the two-way biogeomorphic feedback in saltmarshes allows them to actively adapt to the increasing sea level rise and avoid drowning (Kirwan and Megonigal, 2013).

In lateral direction, however, saltmarshes often show cyclic behavior over a decadal or longer timescale (Yapp et al., 1916; van de Koppel et al., 2005; Van der Wal et al., 2008). The cyclic behavior can be described as: seedling establishment – expansion – cliff initiation – erosion. In this cycle, the seedling establishment and the cliff initiation are recognized as two important tipping points that shift marsh systems from one phase to another. The triggers of these tipping points are closely related to the (bio)morphodynamics that takes place near the boundary between vegetated and bare tidal flats (Bouma et al., submitted). For example, the cliff initiation is the tipping point that causes the onset of continuous marsh erosion (Marani et al., 2011). It is likely induced by the difference between a stable marsh surface and an adjacent dynamic surface in non-vegetated areas. The other tipping points (from erosion to expansion) is the seedling establishment on the bare tidal flat, which is also governed by the morphodynamics at the marsh boundary (Balke et al., 2014). Therefore, to understand the marsh dynamics in the lateral direction, the knowledge of the morphodynamics near the marsh boundary is of great importance. Especially, the dynamics on the bare tidal flat close to the

mature marsh (i.e. pioneer marsh area in Figure 1.1) should be included in the analysis of marsh lateral behaviors.

1.2 Problem definition and objectives

Wave dissipation by vegetation in complex flows

The wave damping capacity of a vegetated area can be quantified by numerical models (Mendez and Losada, 2004; Suzuki et al., 2012; Loon-Steensma et al., 2014). Some vegetation properties (height, stem density and diameter) and wave conditions (wave height and period) can be accounted for explicitly in these models (Mendez and Losada, 2004; Suzuki et al., 2012; Maza et al., 2015; Liu et al., 2015). However, the hydrodynamics in vegetated wetlands can be complex with great spatial and temporal variations (Nepf, 2011, 2012). There is large uncertainty in determining the vegetation drag coefficient in varying flow conditions, which is directly related to the wave dissipation capacity assessment (Pinsky et al., 2013). Furthermore, the existing studies often assess the vegetation-induced wave dissipation only in simplified pure wave conditions. However, for the common combined wave-current conditions, our capability to estimate the vegetation wave damping capacity is still limited (Nepf, 2012; Hu et al., 2014). Large coastal populations and hinterlands can be at risk if the wave damping capacity of coastal wetlands is overestimated. Better understanding of the wave dissipation processes in complex flow conditions is needed for a better estimation.

In this thesis, the related research objectives are:

1) Understand the role of tidal currents in vegetation-induced wave dissipation.
2) Determine the vegetation drag coefficient in various flow conditions.

Bottlenecks to saltmarsh establishment

For effective saltmarsh conservation and restoration, we need sufficient understanding of the critical processes limiting coastal ecosystem establishment. The valuable lesson learned from previous projects is that successful restoration requires both available target species and favorable environmental conditions (Balke et al., 2014; Winterwerp et al., 2013; Wolters et al., 2008). It has been reported that on landscape scale, different hydrodynamic regimes may influence salt marsh developments (Callaghan et al., 2010). However, little is known on the detailed mechanisms that enable/disable seeding initial establishment.

Recently, the Window of Opportunity (WoO) concept has been proposed to explain and predict vegetation initial establishment patterns in various disturbance-driven environments (Balke et al., 2014, 2013b, 2011). It depicts that successful seedling establishment requires a sufficient long period with limited physical disturbance (as a WoO) after the initial settlement on the bare sediment. The occurrence of a WoO can be quantified for the prediction of vegetation establishment patterns.

For the sake of simplicity, tidal inundation was considered as the only physical disturbance influencing saltmarsh establishment in the original WoO framework (Balke et al., 2014). The potential disturbance from hydrodynamic forces was excluded. However, if hydrodynamic forcing is important for marsh establishment, the extent for marsh establishment can be strongly affected by the tidal flat morphology. This implies that altering tidal flat morphology can affect marsh conservation and restoration outcomes.

In this thesis, the related research objectives are:

3). Test the importance of hydrodynamic forcing disturbance in seedling establishment prediction.
4). Illustrate the effect of tidal flat morphology on seedling establishment extent.

Tidal flats never in equilibrium

Friedrichs and Aubrey (1996) assumed that a morphological equilibrium (no net sediment transport) is reached on tidal flats if the maximum bottom shear stress in a tidal cycle is spatially uniform. In reality, the bottom shear stress (BSS) varies continuously both in space and in time. Hence, natural tidal flats may never be in a static equilibrium, but constantly adjust their morphology according to the varying forces and other biotic/abiotic drivers.

Knowledge of the frequent bed-level changes on bare flats is important both for assessing sediment transport processes and for understanding cyclic saltmarsh dynamics (Bouma et al., submitted). High frequency bed-level monitoring with a fine resolution is thus needed for hypothesis testing and validating morphological models. However, conventional manual bed-elevation measurements tend to be discontinuous and generally cannot provide high temporal resolutions due to the labor involved. Existing automated methods for continuous monitoring are either limited in accuracy or are too expensive to allow spatial applications with multiple units. In view of this, we developed a novel instrument called SED-sensor (Surface Elevation Dynamics sensor) for continuous monitoring with a high vertical resolution (2 mm). The

standalone design of the sensor excludes the need for external data logging and a power supply system. The unit cost and the deployment labor are reduced accordingly, which facilitates applications with multiple units.

In this thesis, the research objectives related to this novel instrument are:

5). Test the performance of the new SED-sensors against precise manual measurements

6). Demonstrate how the SED-sensors can be used for measuring short-term bed-level dynamics and for pinpointing the role of hydrodynamic forcing herein

Building on the assumption and analytical solution in (Friedrichs and Aubrey, 1996), Friedrichs (2011) formulated a dynamic equilibrium theory, which systematically explains the tidal flat morphodynamic response to tidal current and wave forcing. A number of field and modeling studies have shown that the tidal flat morphology qualitatively agrees with the analytical models. However, this assessment of the theory is largely empirical and indirect since the analytical profiles were derived assuming a uniform BSS distribution, a condition that rarely exists on actual tidal flats. Additionally, the analytical model cannot be applied for morphological predictions in general cases with varying BSS. In this thesis, we developed a model based on the dynamic equilibrium theory. Different from the original analytical model, this model explicitly accounts for the BSS spatiotemporal variations to predict morphodynamics on bare tidal flats.

In this thesis, the research objectives related to this modeling studies are:

7) Test the dynamic equilibrium theory in general conditions (with varying forcing) using the new morphological model.

8) Demonstrate how to apply the dynamic equilibrium theory for realistic morphological prediction.

1.3 Outline

This thesis focuses on the key hydrodynamic processes in intertidal areas (e.g. wave dissipation by vegetation) as well as the related intertidal landscape formation and evolution mechanisms.

In chapter 2, the often-overlooked effect of tidal currents on wave dissipation by vegetation is investigated (Figure 1.1). In chapter 3, the role of hydrodynamic disturbances on the salt-marsh initial establishment is illustrated in a mechanistic manner (Figure 1.1). Chapter 4 in-

troduces novel SED-sensors, which are designed for high-resolution stand-alone bed-level monitoring. Such a sensor can be a useful tool to study the role of hydrodynamics on the sediment dynamics in the intertidal and other areas. The observed bed-level dynamics can be the consequence of stabilizing and destabilizing biogeomorphologic processes. In Chapter 5, the role of intertidal hydrodynamics on tidal flat morphology is studied. The original ESTMORF (ESTuariene MORFologie; in Dutch) model is modified to incorporate a dynamic equilibrium theory (Proposed by Friedrichs, 2011). The modified model can be applied for both long-term and short-term tidal flat morphodynamics under various hydrodynamic forcing conditions, which also is a convenient framework to include more biogeomorphologic processes.

Chapter 2, 3, 4 and 5 can be regarded as standalone papers with specific aims and conclusions. In Chapter 6, a synthesis combines relevant discussions and the most important findings in the previous chapters. Finally, recommendations for future studies are also given in the last chapter.

Chapter 2

Laboratory study on wave dissipation by vegetation in combined current-wave flow

Zhan Hu, Tomohiro Suzuki, Tjerk Zitman, Wim Uijttewaal, Marcel Stive
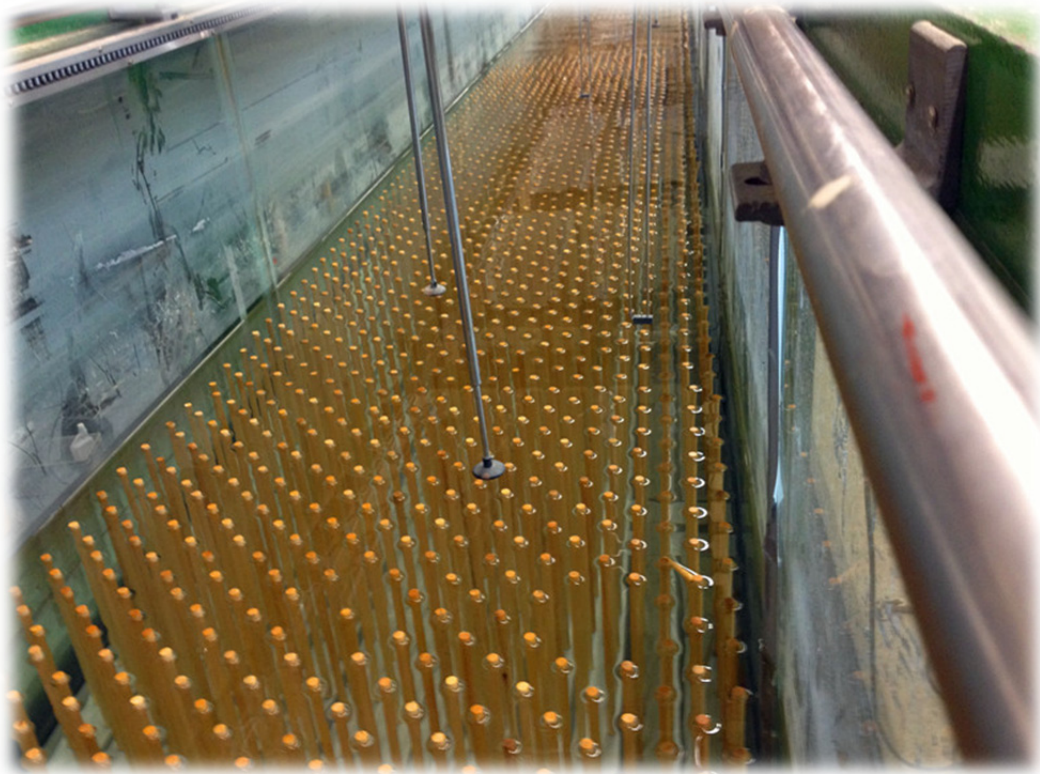
Abstract

Coastal wetlands such as salt marshes and mangroves provide valuable ecosystem services including coastal protection. Many studies have assessed the influence of plant traits and wave conditions on vegetation-induced wave dissipation, whereas the effect of tidal currents is often ignored. To our knowledge, only two studies investigated wave dissipation by vegetation with the presence of following currents (current velocity is in the same direction as wave propagation) (Li and Yan, 2007; Paul et al., 2012). However, based on independent experiments, they have drawn contradictive conclusions whether steady currents increase or decrease wave attenuation. We show in this paper that this inconsistency may be caused by a difference in ratio of imposed current velocity to amplitude of the horizontal wave orbital velocity. We found that following currents can either increase or decrease wave dissipation depending on the velocity ratio, which explains the seeming inconsistency in the two previous studies. Wave dissipation in plant canopies is closely related to vegetation drag coefficients. We apply a new approach to obtain the drag coefficients. This new method eliminates the potential errors that are often introduced by the commonly used method. More importantly, it is capable of obtaining the vegetation drag coefficient in combined current-wave flows, which is not possible for the commonly used calibration method. Based on laboratory data, we propose an empirical relation between drag coefficient and Reynolds number, which can be useful for numerical modeling. The characteristics of drag coefficient variation and in-canopy velocity dynamics are incorporated into an analytical model to help understand the effect of following currents on vegetation-induced wave dissipation.

Highlights

- Steady currents can either enhance or suppress vegetation-induced wave dissipation depending on the ratio between the imposed current velocity and the amplitude of wave horizontal orbital velocity
- A directly measuring method was applied to obtain vegetation drag coefficients in pure wave and current-wave flows
- Co-occurring currents decrease vegetation drag coefficients
- Wave-induced period-averaged velocity is important in understanding wave dissipation

2.1 Introduction

Coastal wetlands such as salt marshes and mangroves are important habitats for various plant and animal species. They also serve as buffers against erosive waves in coastal areas. The upstanding vegetation in coastal wetlands can significantly attenuate wave energy (Anderson et al., 2011), which can reduce the energy load on dikes and stabilize seabed (Callaghan et al., 2010; Shi et al., 2012). The possibility of integrating these natural habitats in coastal protection schemes has been subject of discussion (e.g. Borsje et al., 2011).

Previous laboratory and field measurements have shown that wave energy dissipation by vegetation (hereafter referred as WDV) is affected by both canopy traits and incident wave conditions (e.g. Koftis et al., 2013; Jadhav et al., 2013; Yang et al., 2012; Ysebaert et al., 2012; Bradley and Houser, 2009; Möller, 2006). It is generally agreed in the previous studies that a higher vegetation density, a lower submergence ratio (the ratio of water depth h to canopy height h_v.) and stiffer plant stems lead to higher WDV (e.g. Bouma et al., 2005; Paul et al., 2012; Huang et al., 2011).

In most previous studies, the possible influence of background currents on WDV was not considered due to its complexity. However, it is often the case that when the tide penetrates the coastal wetlands during flooding phase, wind waves propagate in the same direction as the tidal currents. Using the waves as a reference, we designate such currents as following currents. The presence of following currents can affect the wave-damping capacity of vegetation. To our knowledge, Li and Yan (2007) and Paul et al. (2012) were the only two studies that conducted flume experiments and investigated the effect of following currents on WDV. Li and Yan (2007) concluded that following currents promoted WDV. They further demonstrated that WDV increased linearly with the velocity ratio α, defined as the ratio between imposed current velocity and amplitude of horizontal orbital velocity, i.e. U_c/U_w. Paul et al. (2012), on the other hand, found that tidal currents can strongly reduce the wave-damping capacity of their tested mimic canopies. The two studies gave contradicting conclusions about the effect of following currents on WDV. However, the α tested in the two studies was in a different range. The α tested in Li and Yan (2007) was 1.5-3.5, while in Paul et al. (2012) it was less than 0.5. Nevertheless, these two studies suggest that, firstly, the effect of a following current on WDV may depend on the α rather than on the magnitude of U_c alone and, secondly, it depends on α whether following currents enhance or suppress WDV. Therefore, sys-

tematic tests over a wide range of α are needed to properly identify the effect of following currents on WDV.

WDV is primarily induced by work done by drag force acting on the plant stems. A bulk drag coefficient (C_D) was introduced in previous modeling studies to account for the uncertainties lying in the plant-induced drag force F_D (e.g. Dalrymple et al., 1984; Mendez and Losada, 2004; Suzuki et al., 2011). Choosing C_D values is important to WDV prediction. However, the selection of C_D values for a natural vegetation meadow is challenging as it is affected by a number of factors. Specifically, C_D is closely related to the Reynolds number (Re), since it is profoundly influenced by the turbulence in canopies. Various empirical relations between C_D and Re have been proposed for vegetation in pure current or pure wave conditions (Nepf, 2011). Relations between C_D and the Keulegan-Carpenter number ($KC=U_w*T/b_v$, where T is the wave period and b_v is the plant stem diameter) have also been suggested in previous studies (Jadhav et al., 2013; Mendez and Losada, 2004). Moreover, the determination of C_D can be further complicated by the canopy stem density, plant morphology and stem stiffness (Nepf, 2011). Lastly, when a pure wave flow shifts to a combined current-wave flow, we expect the C_D value varies accordingly. However, to our knowledge, the characteristics of vegetation drag coefficient in a combined current-wave flow have not yet been clarified.

In previous studies, C_D values for pure wave conditions have commonly been obtained by calibrating numerical models against observed WDV without measuring the actual force on plants (e.g. Bradley and Houser, 2009; Mendez and Losada, 2004; Koftis et al., 2013; Jadhav et al., 2013). In the case of a following current, this procedure may be inappropriate. The reason for this is that the existing models are intended to quantify WDV in pure wave conditions. As the effect of currents on WDV is not clear, the extension of these models to current-wave conditions may be invalid. Moreover, this method has two shortcomings. Firstly, the accuracy of the C_D values greatly depends on the quality of the model calibration against the measurements. The derived C_D value is unreliable when the correlation between the observations and modeling results is poor. Secondly, it is often assumed that the measured wave energy loss is solely induced by vegetation drag. Other dissipative processes, such as bed friction and wave breaking, are not explicitly considered but lumped into the vegetation drag, which can lead to an overestimated C_D.

Other than the calibration approach, C_D values can also be obtained via a more direct method. Infantes et al. (2011) measured the total force (F) and impact velocity on sea grass seedlings

in pure current and pure wave conditions and derived C_D directly from the original Morison Equation (Morison et al., 1950). They applied this method to compare the tolerance of different sea grass species to water motion. This direct method can help us to understand WDV processes by providing accurate C_D values that eliminate potential modeling errors. Furthermore, this method can be applied to plant canopies in combined current-wave flows since the Morison Equation still holds in such conditions (Sumer and Fredsøe, 2006; Zhou and Graham, 2000). This direct measuring method provides a way to obtain C_D values for vegetation in current-wave conditions, which is not possible for the commonly used calibration method.

Apart from the drag coefficient, insight in the flow structures inside the canopy is required for a proper understanding of WDV (Lowe et al., 2007). Compared to the extensive studies on unidirectional flow passing vegetated canopies, the flow structure for waves has been less studied (Lowe et al., 2005). In recent investigations a non-zero mean current velocity has been found in the vegetation canopies when the flow is driven purely by waves (Luhar et al., 2010; Pujol et al., 2013). The impact of this mean velocity on nutrient uptake and sediment transport has been identified, but its influence on WDV is not clear.

In this study, flume experiments with stiff plant mimics were carried out with a wide range of the ratio α to explore the effect of following currents on WDV. A direct force measurement method was applied to quantify C_D coefficients in both pure wave and current-wave flows. Vertical velocity profiles were also measured and the impact of a wave-induced mean current on WDV was illustrated. The insights of drag coefficients and velocity measurements were incorporated in an analytical model to explain the observed variation of WDV with α.

2.2 Methods

2.2.1 Flume setup

Experiments with plant mimics were conducted in a wave flume of the Fluid Mechanics Laboratory at Delft University of Technology. The wave flume is 40 m long and 0.8 m wide (schematized in Figure 1a). A wave generator with an active wave absorption system is placed at one side of the flume (left in Figure 2.1a). Imposed currents were in the same direction as the wave propagation. Hereafter, the direction of wave propagation is defined as '*positive*' and the opposing direction is defined as '*negative*'.
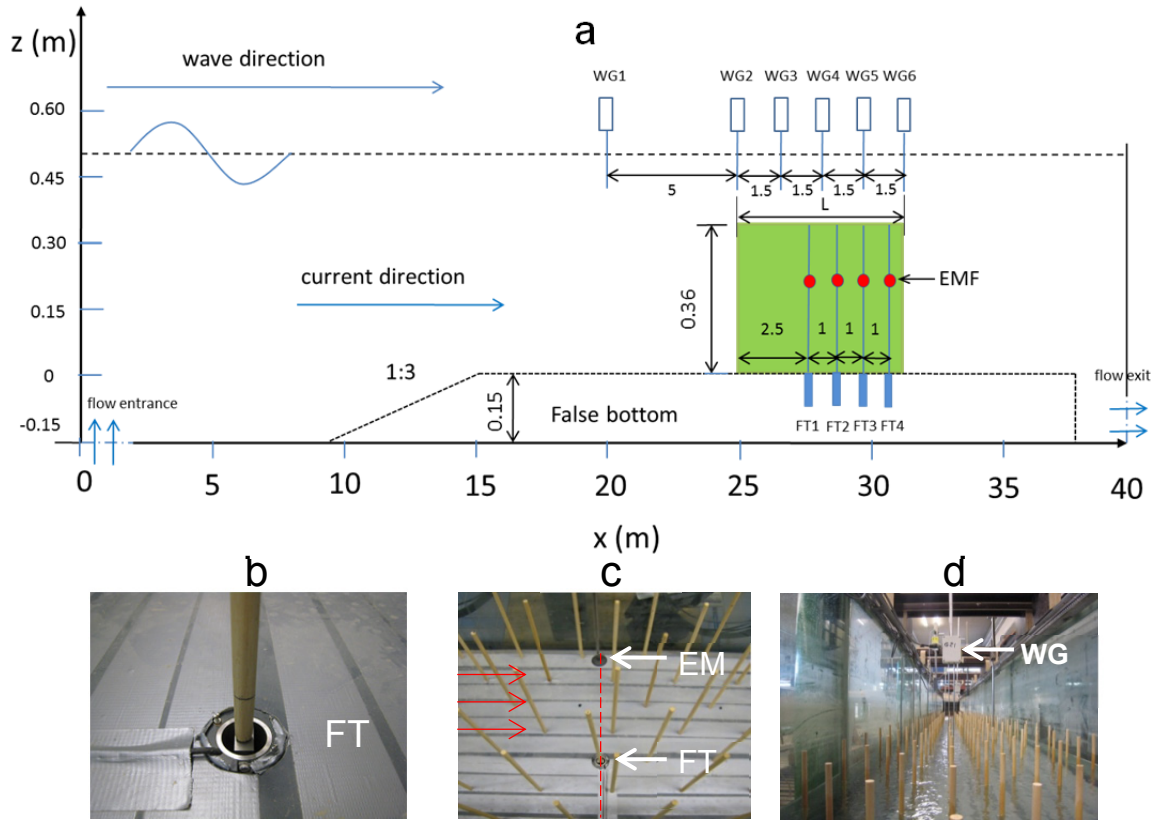
Figure 2.1 Wave flume setup. (a) schematic flume configuration and instruments deployment; (b) Force transducer in the flume bed; (c) EMF and Force transducer at the same cross section in the flume, the following current flows from the left to the right indicated by the three parallel arrows; (d) mimic plants canopy (low mimic stems density); WG1-WG6 stands for wave gauges, EMF stands for electromagnetic flow meter, FT1-FT4 stands for force transducers and L=6 m is the length of the mimic plant canopy

The mimic canopies were constructed by putting stiff wooden rods (Figure 2.1d) in holes drilled in the false bottom (Figure 2.1a). The height of the rods was 0.36 m and their diameter was 0.01 m. The canopy was 6 m long and 0.8 m wide and the stems were distributed uniformly in space. Three mimic stems densities (N), namely 62, 139 and 556 stems/ m², were constructed by putting corresponding number of rods into the plates with drilled holes (Figure 2.2). The three stem densities are denoted as VD1, VD2 and VD3, respectively. Control tests (VD0) were carried out with no mimic stems in the flume to measure the wave height reduction by the friction of flume bed and sidewalls. Two water depths were chosen to form emergent and submerged canopies. The water levels were at z=0.25m and z=0.50 m respectively. The corresponding submergence ratios (h/h_v) were 1 and 1.39.
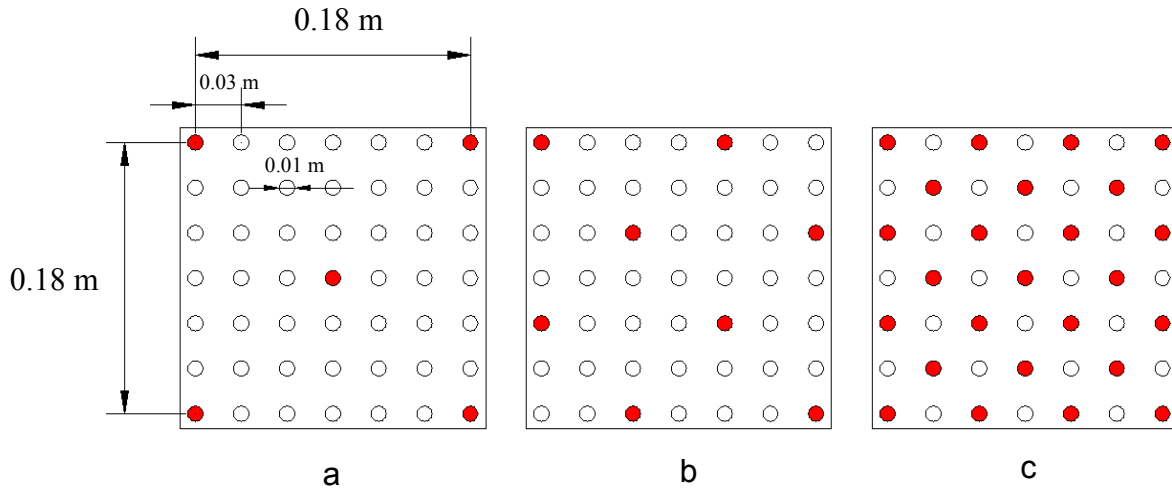
Figure 2.2 Wave flume setup. (a) schematic flume configuration and instruments deployment; (b) Force transducer in the flume bed; (c) EMF and Force transducer at the same cross section in the flume, the following current flows from the left to the right indicated by the three parallel arrows; (d) mimic plants canopy (low mimic stems density); WG1-WG6 stands for wave gauges, EMF stands for electromagnetic flow meter, FT1-FT4 stands for force transducers and L=6 m is the length of the mimic plant canopy

The force *F* on 4 individual stems in the mimic canopies was measured by 4 force transducers (Figure 2.1a). These stems are identical to the ones in the mimic canopies. The bottom end of each these stems was attached to a force transducer by a screw which was fixed inside the stems (Figure 2.1b). In the flume, the force transducers were mounted into the false bottom to avoid disturbance of the flow (Figure 2.1b). The force transducers were developed by Delft Hydraulics (Delft, The Netherlands). Tests with known weights revealed that the voltage output of the transducers varies linearly with the force exerted on them with an estimated accuracy of 1%. In the tests, these forces ranged from -1.8 N to 1.8 N (where the sign refers to the direction of the force). This covers the working range of the transducers in the experiment (-0.3 N to 1.0 N). Data was sampled at 1000 Hz in order to capture the variation of *F* within a wave period (1 s - 2.5 s). The force transducers had been used before in studies that compared the tolerance of seedlings to the drag force induced by currents or waves (Infantes et al., 2011; Bouma et al., 2005). A detailed description of the force transducers can be found in Bouma et al., (2005).

The instantaneous horizontal velocity (*u*) was measured by 4 EMFs (electromagnetic flow manufacture meters), which were made by Delft Hydraulics. Velocity (*u*) was measured at the same wave flume cross sections as the force transducers, to obtain the in-phase data (Figure 2.1c). With different water depth, *u* was measured at mid depth. To obtain velocity profiles,

the EMFs probes were moved vertically. In emergent canopy cases the velocity was measured at $z = 0.025$ m, 0.075 m, 0.125 m and 0.175 m. For submerged canopy cases, u was measured at $z = 0.05$ m, 0.15 m, 0.25 m, 0.30 m, 0.325 m, 0.375 m, 0.40 m and 0.45 m. Note that the measurement resolution was refined near the top of the canopy ($z = 0.36$ m). Six capacitance-type wave gauges made by Delft Hydraulics (WG1-WG6) were installed in the flume to measure the wave height (see Figure 2.1a and Figure 2.1d). WG1 was placed at $x = 20$ m, which was 5 m in front of the canopy. WG2-WG6 were placed 1.5 m apart from each other in the canopy, starting at $x = 25$ m. The output of EMF and WG were also in voltage, which can be converted to velocity and water level by linear regression relations. The accuracy of the EMFs and WGs was 1% and 0.5% respectively (Delft Hydraulics, 1990; Delft Hydraulics, year unknown).

Table 2.1 Test conditions

Source	Plant mimics type	Water depth (h) /plants height (m)	Mimic stems density (N) (stems/m^2)	Wave height (H) (m)	Wave period (T) (s)	Wave case name	Current velocity (U_C) (m/s)
present study	Stiff wooden rods	0.25 / 0.36	62 / 139 / 556	0.04	1.0	wave0410[a]	0 / 0.05 / 0.15 / 0.20
			62 / 139 / 556	0.04	1.2	wave0412	0 / 0.05 / 0.15 / 0.20
			62 / 139 / 556	0.06	1.0	wave0610	0 / 0.05 / 0.15 / 0.20
			62 / 139 / 556	0.06	1.2	wave0612	0 / 0.05 / 0.15 / 0.20
			62 / 139 / 556	0.08	1.2	wave0812	0 / 0.05 / 0.15 / 0.20
			62 / 139 / 556	0.08	1.5	wave0815	0 / 0.05 / 0.15 / 0.20
			62 / 139 / 556	0.10	1.5	wave1015	0 / 0.05 / 0.15 / 0.20
		0.50 / 0.36	62 / 139 / 556	0.04	1.0	wave0410	0 / 0.05 / 0.15 / 0.20/ 0.30
			62 / 139 / 556	0.06	1.2	wave0612	0 / 0.05 / 0.15 / 0.20/ 0.30
			62 / 139 / 556	0.08	1.4	wave0814	0 / 0.05 / 0.15 / 0.20/ 0.30
			62 / 139 / 556	0.10	1.6	wave1016	0 / 0.05 / 0.15 / 0.20/ 0.30
			62 / 139 / 556	0.12	1.6	wave1216	0 / 0.05 / 0.15 / 0.20/ 0.30
			62 / 139 / 556	0.12	1.8	wave1218	0 / 0.05 / 0.15 / 0.20/ 0.30
			62 / 139 / 556	0.15	1.6	wave1516	0 / 0.05 / 0.15 / 0.20/ 0.30
			62 / 139 / 556	0.15	1.8	wave1518	0 / 0.05 / 0.15 / 0.20/ 0.30
			62 / 139 / 556	0.15	2.0	wave1520	0 / 0.05 / 0.15 / 0.20/ 0.30
			62 / 139 / 556	0.18	2.2	wave1822	0 / 0.05 / 0.15 / 0.20/ 0.30
			62 / 139 / 556	0.20	2.5	wave2025	0 / 0.05 / 0.15 / 0.20/ 0.30
Li and Yan (2007)	Semi-rigid rubber rods	0.15 / 0.25	1111[b]	0.04/ 0.05/ 0.07	0.7/0.9/1.1	-	0.18/0.27/0.32
Paul et al. (2012)	Flexible poly ribbon	0.30 / (0.15 & 0.30)	500/ 2000[c]	0.1	1	-	0 / 0.10

[a] The case name is created using a combination of incident wave height 0.04 m and wave period 1.0 s, namely wave0410.

[b] Mimic stem diameter tested in Li and Yan, (2007) is 6-8 mm. Hence, the frontal area per canopy volume ($N*b_v$ as in Nepf, 2011) is 6.67 m^{-1} -8.89 m^{-1}, which is comparable to that of the VD3 tests (5.56 m^{-1}) in the present study.

[c] The width of the flexible mimics in the experiment was 0.2 cm. Hence, the frontal area per canopy volume in their test is 1.00 m^{-1} and 4.00 m^{-1} respectively, which is comparable to that of VD2 and VD3 test (1.39 m^{-1} and 5.56 m^{-1} respectively) in the present study. The tests with stiff mimics in their test were excluded from comparison since their densities were not comparable to the present study.

In total, 314 tests were carried out with 3 different mimic stem densities, 2 water depths and various wave-current conditions (Table 1). The considered velocity ratio α was in the range of 0-5.4. For the emergent canopies, 7 different wave conditions were tested in combination with 4 steady current velocities (including the tests when $U_c = 0$ m/s). In the submerged canopies, 11 wave conditions were tested in combination with 5 steady current velocities. For the sake of simplicity, only monochromatic waves are the in this experiment. Hereafter, the subscript '*pw*' stands for pure wave conditions and subscript '*cw*' stands for combined current-wave conditions. It was noted that the wave height could be reduced when waves propagate in the same direction as current velocity due to the Doppler Effect (Demirbilek et al. 1996). To compensate for such loss, the incident wave height was amplified in current-wave cases to maintain the targeted wave height. The difference in wave height was less than 3% between the tests with different current velocities.

2.2.2 Data analysis

2.2.2.1 Velocity data analysis

The measured instantaneous horizontal flow velocity (m/s) can be expressed as:

$$u(t) = U_{mean} + U_w \sin(\omega t) + U' \quad (2.1)$$

where, ω is the wave angular frequency (Hz), t is time (s), U' stands for turbulent velocity fluctuations (m/s) and U_w is the amplitude of the horizontal wave orbital velocity (m/s), defined as

$$U_w = \frac{1}{2}(u_{max} - u_{min}) \qquad (2.2)$$

where u_{max} and u_{min} are the peak flow velocities (m/s) in the positive and negative direction in a wave period, respectively. U_{mean} is the wave-averaged velocity (m/s) and can be defined as (e.g. Pujol et al., 2013):

$$U_{mean} = \frac{\omega}{2\pi} \int_{-\pi/\omega}^{\pi/\omega} u \, dt \qquad (2.3)$$

Note that U_{mean} is not equal to the imposed steady velocity U_c. The difference between the two is that U_{mean} is the period-averaged velocity of pure wave or current-wave flow whereas

U_c is not influenced by wave motions, and is equal to the time-mean velocity of unidirectional flow passing a canopy. Representative velocity data of the total mimic canopy can be obtained by spatially averaging the data from the 4 locations in the mimic canopy (Figure 2.1a).

Previous studies found that C_D was closely related to the Reynolds number (Re) (-) (reviewed in Nepf, 2011). In this study, it is defined using a characteristic velocity U_{max} (m/s):

$$Re = \frac{U_{max}b_v}{v} \qquad (2.4)$$

Where $v=10^{-6}$ m²/s is the kinematic viscosity, U_{max} equals to the spatially averaged U_w for the pure wave conditions or spatially averaged $U_{mean} + U_w$ for current-wave conditions, respectively. Mendez et al., (1999) proposed a modified Reynolds number (Re*) (-), according to:

$$Re^* = \frac{U^*_{max}b_v}{v} \qquad (2.5)$$

where U^*_{max} equals to the U_w in front of the tested canopy (x = 25 m in our experiments) at the top of the mimic stems.

2.2.2.2 C_D quantification by direct force measurement

Assuming the plant mimics are similar to an array of rigid piles, the Morison Equation (Morison et al., 1950) can be applied to quantify the total force on them:

$$F = F_D + F_M = \frac{1}{2}\rho C_D h_v b_v u(t)|u(t)| + \frac{1}{4}\rho C_M \pi h_v b_v^2 \frac{\partial u(t)}{\partial t} \qquad (2.6)$$

where F_D is the drag force (N), F_M is the inertial force (N), ρ is fluid mass density (kg/m³), h_v is the height of vegetation in water (m), b_v is the plant stem diameter (m) and C_D the drag coefficient (-). Furthermore, C_M is the inertia coefficient (-), equals to 2 for circular cylinders (Dean and Dalrymple, 1991). It is noted that F_M has no contribution to the WDV (Dalrymple et al. 1984). That is because the work performed by F_M per wave period equals zero. This holds for both pure wave and current-wave conditions. Hence, the work done by F_D in a wave period is equal to that done by F. Therefore, a period-averaged C_D can be obtained by quantifying the work done by F in a wave period. Hence:

$$C_D = \frac{2\int\limits_{-\pi/\omega}^{\pi/\omega} F_D u \, dt}{\int\limits_{-\pi/\omega}^{\pi/\omega} \rho h_v b_v u^2 |u| \, dt} = \frac{2\int\limits_{-\pi/\omega}^{\pi/\omega} F u \, dt}{\int\limits_{-\pi/\omega}^{\pi/\omega} \rho h_v b_v u^2 |u| \, dt} \quad (2.7)$$

A space-averaged C_D can be derived by averaging the data from the 4 locations in the canopy (Figure 2.1a).

2.2.3 Wave dissipation models

2.2.3.1 Wave dissipation model for pure wave cases

Applying the Morison Equation and linear wave theory, Dalrymple et al., (1984) described monochromatic wave propagation in a plant canopy on a plain bed as:

$$K_v = \frac{H}{H_0} = \frac{1}{1 + \beta D} \quad (2.8)$$

$$\beta = \frac{4}{9\pi} C_D b_v N H_0 k \frac{\sinh^3 kh_v + 3\sinh kh_v}{(\sinh 2kh + 2kh)\sinh kh} \quad (2.9)$$

where K_v is the relative wave height, H is the wave height (m) at distance D (m) in a canopy, H_0 is the wave height at the edge of the canopy, k is the wave number (m^{-1}). For pure wave cases, C_D is derived commonly by inverting Equation 2.9, provided that β (m^{-1}) has been obtained by fitting the Equation 2.8 to measured WDV (e.g. Bradley and Houser, 2009; Jadhav et al., 2013).

To exclude the possible influence of bed and sidewall friction, the wave height reduction measured in the control tests (VD0) is subtracted from the one observed in the tests with mimics canopies (Augustin et al., 2009).

Wave height reduction per unit length of a plant canopy (ΔH) is derived as:

$$\Delta H = \frac{H_0 - H_{out}}{L} \quad (2.10)$$

where H_{out} is the wave height at the end of the mimic canopy (m) and L is the length of the canopy. To exclude the possible influence of bed and sidewall friction, the wave height reduc-

tion measured in the control tests (VD0) is subtracted from the one observed in the tests with mimics canopies (Augustin et al., 2009).

2.2.3.2 Analytical model for wave dissipation in current-wave flows

We propose a simple analytical model to better understand the effect of steady currents on WDV. This model is based on the following assumptions:

1) velocity u is uniform over the water depth;
2) turbulent velocity fluctuations (U' in Equation 2.1) are neglected;
3) the instantaneous horizontal orbital velocity is $U_w sin(\omega t)$;
4) for current-wave conditions, the period-averaged velocity equals the imposed current velocity, i.e. $U_{mean} = U_c$. Thus, the total instantaneous $u(t) = U_c + U_w sin(\omega t)$;
5) C_D and U_w do not vary when flow changes from pure wave conditions to current-wave conditions.

Based on the above assumptions, the period-averaged wave energy dissipation rate per unit area ε is expressed as follows.

For pure wave conditions:

$$\varepsilon_{pw} = \frac{\omega}{2\pi} \int_{-\pi/\omega}^{\pi/\omega} NF_D U_w \sin(\omega t) dt = \frac{\omega}{4\pi} \int_{-\pi/\omega}^{\pi/\omega} \rho C_D Nb_v h_v \left| U_w \sin(\omega t) \right| (U_w \sin(\omega t))^2 dt = \frac{2}{3\pi} \rho C_D Nb_v h_v U_w^3 \quad (2.11)$$

For current-wave conditions:

$$\varepsilon_{cw} = \frac{\omega}{2\pi} \int_{-\pi/\omega}^{\pi/\omega} NF_D (U_c + U_w \sin(\omega t)) dt = \frac{\omega}{4\pi} \int_{-\pi/\omega}^{\pi/\omega} \rho C_D Nb_v h_v \left| U_c + U_w \sin(\omega t) \right| (U_c + U_w \sin(\omega t))^2 dt$$

$$= \begin{cases} \frac{1}{2\pi} \rho C_D Nb_v h_v [\sin^{-1}(\frac{|U_c|}{U_w})(2|U_c|U_c^2 + 3|U_c|U_w^2) + \frac{1}{3}(4U_w^2 + 11U_c^2)(\sqrt{U_w^2 - U_c^2})] & |U_c| < U_w \\ \frac{1}{4} \rho C_D Nb_v h_v (2|U_c|U_c^2 + 3|U_c|U_w^2) & |U_c| \geq U_w \end{cases} \quad (2.12)$$

ε_{cw} is derived from the current-wave interaction, which can be divided into the wave induced energy dissipation rate ε_{cw_w} and the current induced energy dissipation rate ε_{cw_c} (Li and Yan, 2007):

$$\varepsilon_{cw\_c} = \frac{1}{2}\rho C_D N b_v h_v |U_c| U_c^2 \qquad (2.13)$$

Therefore, the ratio of ε_{cw_w} and ε_{pw} is:

$$f(\alpha) = \frac{\varepsilon_{cw\_w}}{\varepsilon_{pw}} = \frac{\varepsilon_{cw} - \varepsilon_{cw\_c}}{\varepsilon_{pw}} = \begin{cases} \frac{3}{4}\sin^{-1}(|\alpha|)(2|\alpha|\alpha^2 + 3|\alpha|) + \frac{1}{4}(4+11\alpha^2)\sqrt{1-\alpha^2} - \frac{3\pi}{4}|\alpha|\alpha^2 & |\alpha| < 1 \\ \frac{9\pi}{8}|\alpha| & |\alpha| \geq 1 \end{cases} \qquad (2.14)$$

where $\alpha = U_c/U_w$. ε is proportional to the square of wave height. ΔH_{pw} is the reduced wave height per unit length of mimic canopies in pure wave conditions and ΔH_{cw} is that in current-wave conditions. Considering the different magnitudes of length scales, the relative wave height decay r_w can be derived as:

$$r_w = \frac{\Delta H_{cw}}{\Delta H_{pw}} = \sqrt{\frac{\varepsilon_{cw\_w}}{\varepsilon_{pw}}} \qquad (2.15)$$

However, our assumptions may be restrictive. Certain modifications may be necessary when applying this model for realistic conditions.

2.3   Results

2.3.1 Wave dissipation by mimic vegetation canopies

The measured K_v in pure wave conditions is shown in Figure 2.3a. The tested canopies were VD2 and VD3. The tested wave condition was wave0410. With the same wave condition, a higher WDV was found in the mimic canopy with a higher mimic stem density and a lower submergence ratio. β can be derived by fitting Equation 2.8 to the measured K_v. Subsequently, the obtained β can be substituted into Equation 2.8 to describe the WDV (dashed line in Figure 2.3a).

The effect of currents can be identified by comparing the WDV with different imposed current velocities (U_c) (Figure 2.3b). The test shown in Figure 2.3b was carried out in emergent conditions. The canopy stem density was VD3. Four steady currents, namely $U_c = 0$, 0.05 m/s, 0.15 m/s and 0.20 m/s, were imposed in combination with the same wave condition

(wave0610). The corresponding α were 0, 0.6, 2.8 and 4.4, respectively. For the case with a relatively small α (α= 0.6), the K_v along the canopy is higher than the one found in pure wave condition, thus a lower WDV. When the α is larger (α =2.8), the K_v is lower than that of the pure wave conditions, i.e. higher WDV. The WDV further increases when the α rises from 2.8 to 4.4.
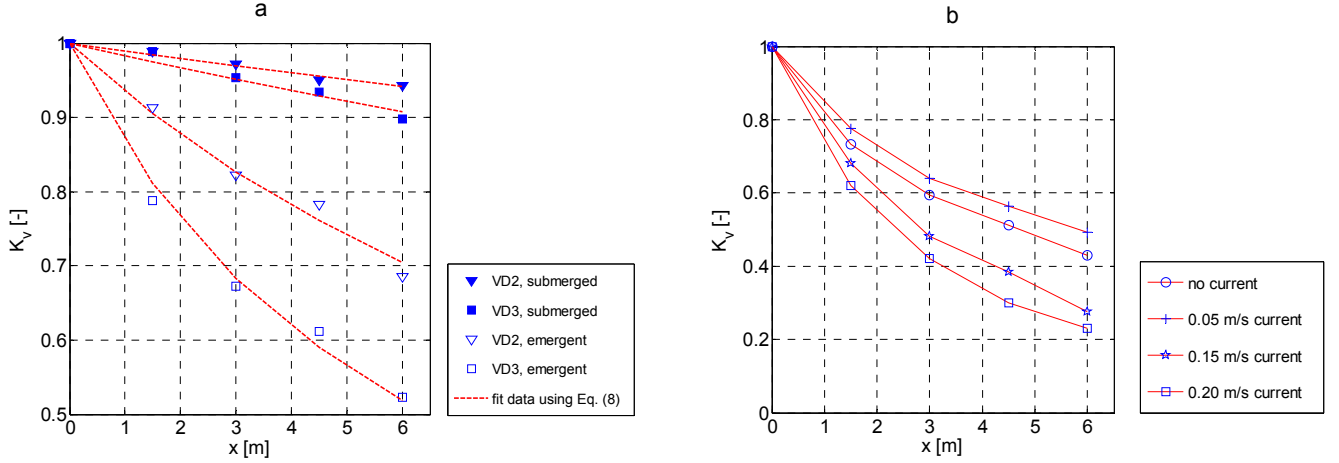
Figure 2.3 Damping coefficient (K_v) evolution in mimic canopies. (a) the effect of mimic stems density and submergence ratio on K_v; (b) the effect of different imposing current velocities on K_v

The effect of the steady currents on WDV can be further evaluated by comparing the r_w. If it is larger than 1, it means the WDV is increased with the presence of following currents. If it is less than 1, then WDV is reduced when following currents occur. The relation between the r_w and α is shown in Figure 2.4. It shows that WDV in all the tests is influenced by following currents except the tests at the transition points, where the r_w=1. Thus, the WDV is the same as it is in pure wave conditions. In different test conditions, transition points vary from 0.65 to 1.25. When the value of α is less than its value at the transition points, r_w is less than 1. Thus, the following currents decrease the WDV. In this range of α, r_w reaches its minimum when α is around 0.5. Subsequently, it starts increasing with α. When α exceeds the value at the transition points, r_w>1. It means that in this range of α, the presence of currents increases the WDV. Therefore, the following currents can either increase or decrease WDV depending on α. Even though all the cases share the same general pattern, there are differences between the cases with different test conditions. Data from the VD1 canopy is more scattered than others. The minimum r_w ratios are lower in submerged canopies than that in emergent canopies.
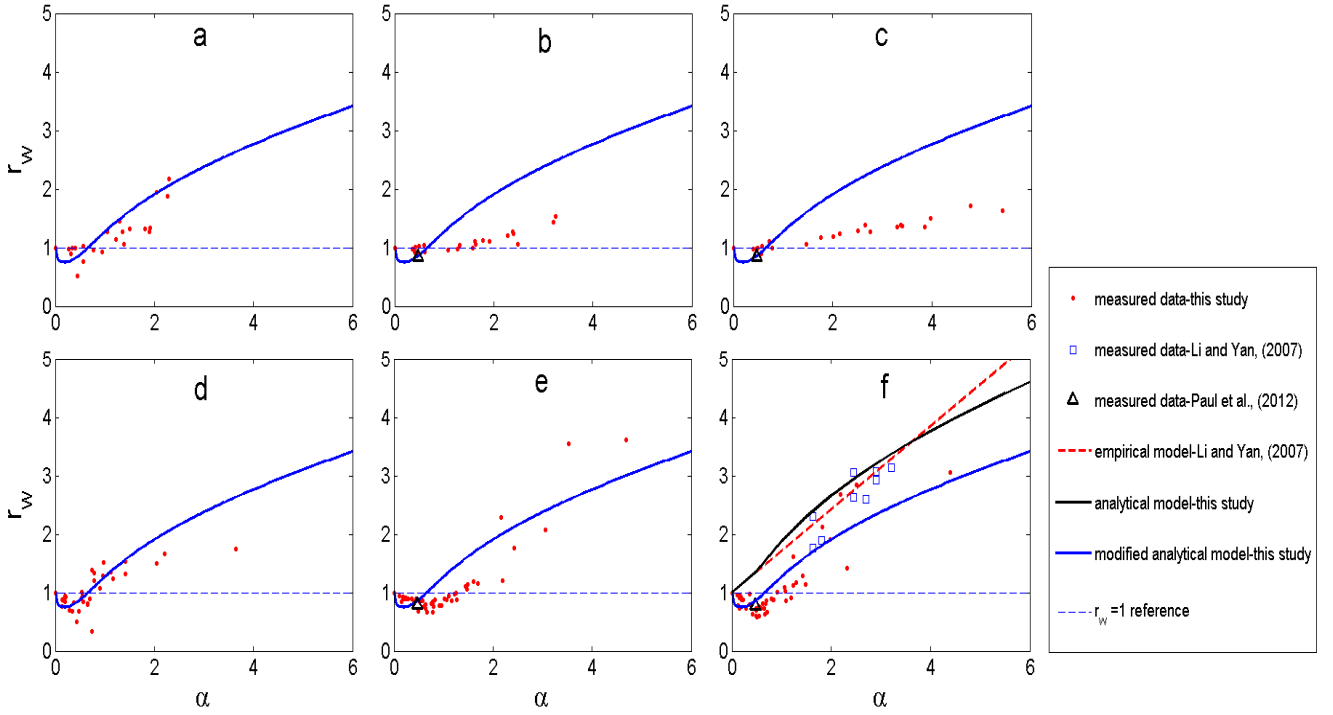
Figure 2.4 Variation r_w with velocity ratios α. (a), (b), (c) are emergent canopy with mimic stems density VD1, VD2 and VD3 respectively; (d), (e), (f) are submerged canopy with mimic stems density VD1, VD2 and VD3 respectively.

Data obtained with comparable conditions in Paul et al. (2012) and Li and Yan (2007) are also plotted in Figure 2.4. When the value of α is less than that at the transition point, our measurement result is similar to that of Paul et al. (2012), who evaluated the WDV with a α value (0.47) lower than the transition point. However, when α is lower than the transition point, our result of r_w is less than the prediction of an empirical model in Li and Yan (2007). The model predicts that r_w is larger than 1 for all α (Figure 2.4f). When α is high (> 1.6), our measurement result is close to the experimental data and the model prediction of Li and Yan (2007). The Equation describing the empirical model was not given in Li and Yan (2007), but its outcome was provided as a plot, which was adapted in Figure 2.4f.

The prediction obtained with our analytical model (outlined in section 2.3.2) is also plotted in Figure 2.4f. Similar to the empirical model in Li and Yan (2007), the analytical model predicts that WDV increases monotonically with the velocity ratio α, which overestimates the WDV when α is small. To improve the model prediction, two modifications of the model are made:

1). the drag coefficient in current-wave cases is a proportion of that in pure wave cases, i.e. $C_{D\_cw}=0.66*C_{D\_pw}$. Such a ratio was derived from drag coefficient measurements (see Figure 2.6).

2). in pure wave cases, the time-mean velocity (U_{mean}) is nonzero (see Figure 2.7). U_{mean} is in the negative direction and U_{mean}/U_w = -0.2 .Such a value is determined by averaging ratios measured in all the pure wave cases. in current-wave cases, U_{mean} is suppressed by wave motions (see Figure 2.8). It is smaller than the imposed current velocity without wave influence (U_c) i.e. $U_{mean}/U_w - U_c/U_w$ = -0.2. Such a value is determined by averaging the difference measured in all the current-wave cases.

With these two modifications, Equation 2.14can be rewritten as:

$$f'(\alpha) = \begin{cases} 1 & \alpha = 0 \\ 0.66 \dfrac{f(\alpha - 0.2)}{f(-0.2)} & \alpha > 0 \end{cases} \qquad (2.16)$$

The result of this modification is shown in Figure 2.4f. It appears that the modified analytical model is able to reproduce the general non-monotonic variation of r_w.

2.3.2 Drag coefficient quantification

2.3.2.1 Time dependent drag force and drag coefficient

The time dependent F_D can be derived from in-phase data of F and u obtained at same cross-sections of the flume (Equation 2.6). Figure 2.5 shows the time-varying F and u at x = 29.5 m in the wave flume. The tests concern the submerged VD3 canopy in combination with the wave case wave1216. Figure 2.5a and Figure 2.5b show that the measured oscillating u and F_D are generally in phase. The time lag between the two is very small (ca. 0.05 s). Figure 2.5a further shows that u is asymmetric in the pure wave case. The period-averaged velocity (U_{mean}) is in negative direction. In the case with a small imposed current velocity (U_c = 0.05 m/s), the small U_c counteracts the period-averaged negative velocity and results in a more symmetric u, i.e. U_{mean} is close to zero. A larger U_c (0.15 m/s) can shift the overall u further towards the positive direction and results in a positive U_{mean}. The magnitudes of F_D with different following currents vary according to that of u (Figure 2.5b).
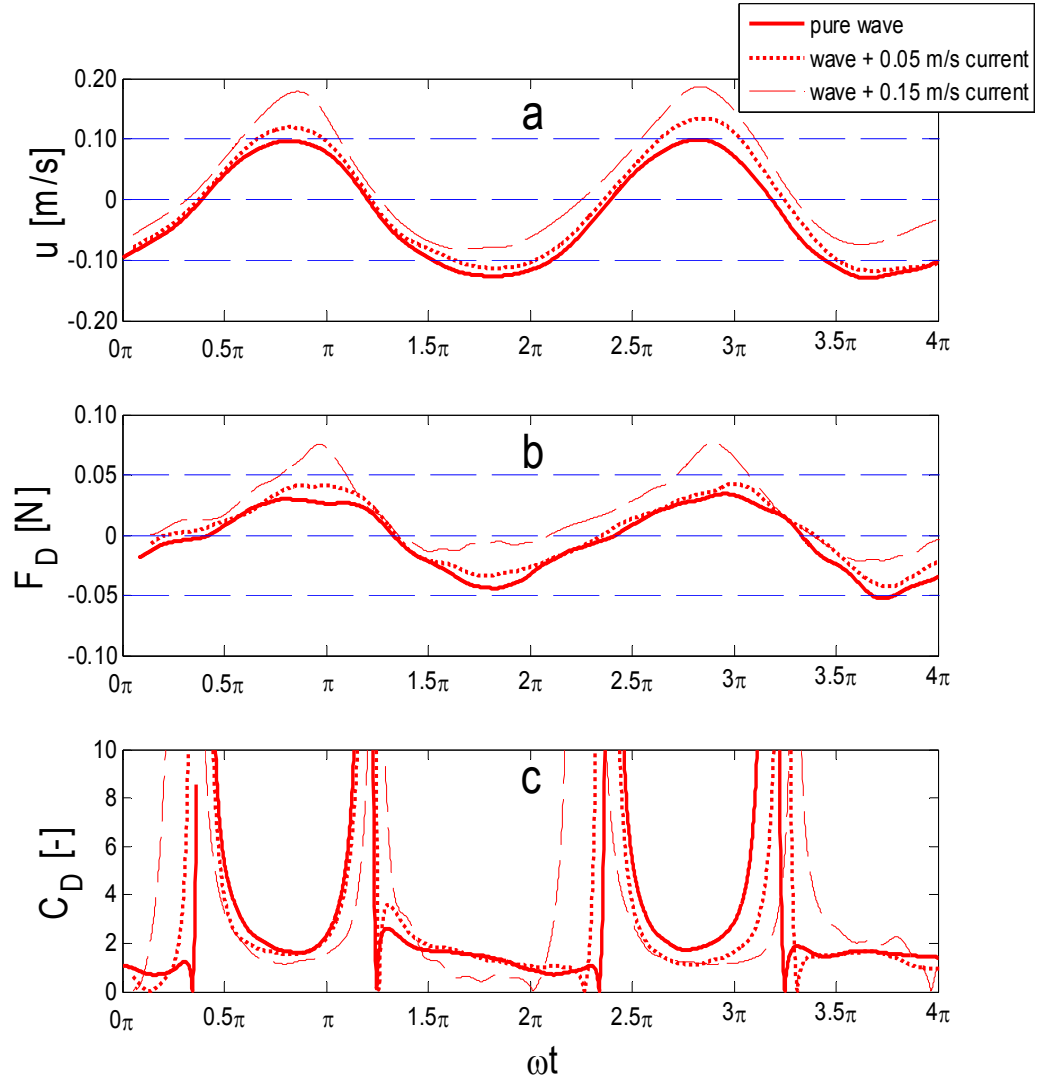
Figure 2.5 Temporal variation of (a) velocity, (b) drag force and (c) drag coefficient with different imposed current velocities

Figure 2.5c shows that the time dependent C_D varies with u and F_D accordingly. When u is near its crest or trough, the time-dependent C_D is relatively constant. However, when u is small, the time dependent C_D is unrealistically high because the velocity is approaching zero. It is also noted that the time dependent C_D can drop to zero when F_D is weak. Figure 2.5c further demonstrates that the pure wave case is generally associated with a comparatively large C_D and an increase in U_c generally leads to a decrease of C_D.

2.3.2.2 Period-averaged drag coefficients

Previous study has indicated that the period-averaged C_D is closely related to the Reynolds number (reviewed in Nepf, 2011). Figure 2.6 shows the relation between C_D and two Reyn-

olds numbers, namely Re and Re*. These two Reynolds numbers are defined in Equation 2.4 and 2.5 respectively.

The C_D values presented in Figure 2.6a are obtained in pure wave conditions by using the calibration approach (Equation 2.8 and 2.9). Generally, C_D decreases with Re*, but the data points are scattered. The empirical relationship between C_D and Re* given by Mendez et al. (1999) is also plotted in Figure 2.6a. Despite the scattering, the C_D obtained from the calibration approach is in the same range as estimated by the empirical relationship:

$$C_D = 0.08 + (\frac{2200}{Re^*})^{2.2} \qquad 200 < Re^* < 15500 \qquad (2.17)$$
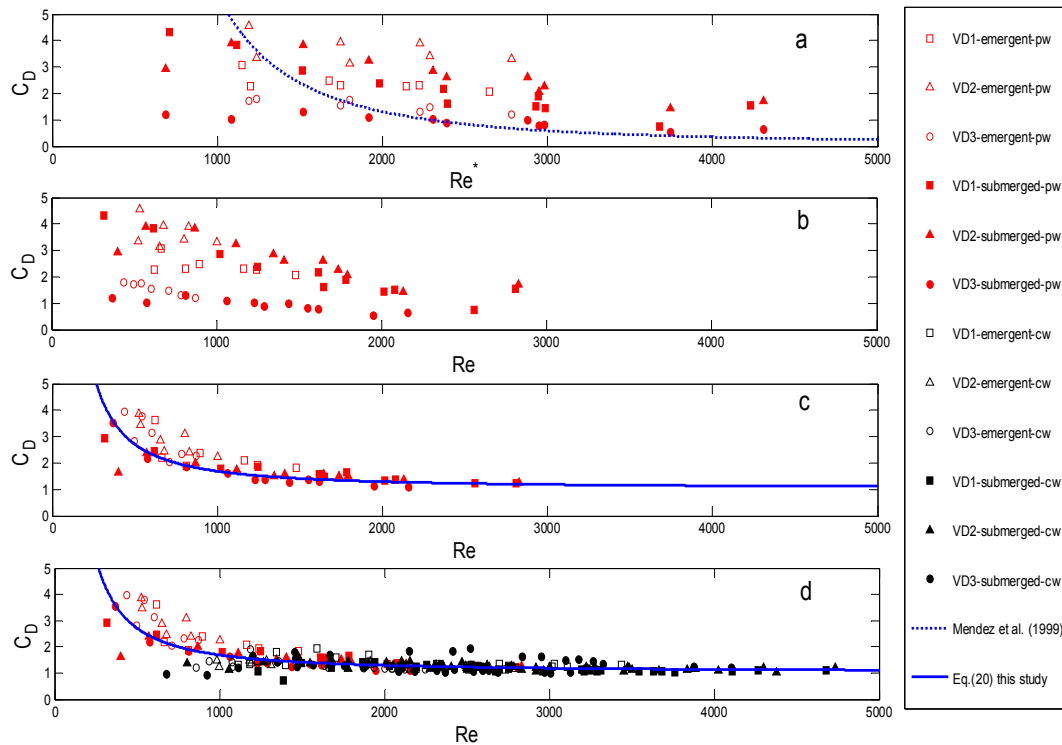
Figure 2.6 Relation between Re and period-averaged C_D (a) C_D in pure wave conditions derived by the calibration approach (using Equation 2.8 and 2.9) as a function of Re*; (b) C_D in pure wave conditions derived by the calibration approach as a function of Re; (c) C_D in pure wave conditions derived by the direct force measurement approach as a function of Re; (d) C_D in pure wave and current-wave conditions derived by the direct force measurement approach as a function of Re; In the legend, 'pw' stands for pure wave conditions and 'cw' stands for current wave conditions

Figure 2.6b shows the C_D derived from the calibration approach as a function of Re. It is clear that the data is less scattered compared to that in Figure 2.6a. The declining pattern of C_D with

increasing Re is also more apparent. The C_D derived from emergent canopies is comparable to that from submerged canopies. It is noted that the submergence ratio has a minor effect on the variation of C_D with Re.

Figure 2.6c shows the C_D values derived from the direct force measurements (Equation 2.7) for pure wave cases, as a function of Re. They were spatially averaged using 3 out of 4 locations that had simultaneous F and u measurements. FT2 failed during the experiment (see Figure 2.1a) and it was excluded from the data analysis. It is clear that the derived C_D values share a similar decreasing pattern as that derived from the calibration approach. Specifically, when 300<Re<1000, the C_D drops quickly from around 4.0 to 1.7. When Re>1000, the reduction of C_D with increasing Re becomes mild. Similar to the calibration approach, the submergence ratio hardly affects the C_D pattern. Emergent canopy cases generally had lower values of Re, which resulted in higher C_D values. Submerged canopy cases generally had higher values of Re, thus lower C_D values. It is evident that this direct measuring method leads to less scattering between C_D from different mimic stems densities.

The main advantage of applying the direct measuring approach is that it can be used to derive the C_D in current-wave flows. Figure 2.6d presents the C_D values from both current-wave cases and pure wave cases (listed in Table 1). It shows that the typical decreasing pattern of C_D still holds in current-wave conditions. Compared to the pure wave cases, the current-wave cases were inherently associated with higher Re because of the superimposed current U_c. Consequently, the higher Re leads to lower C_D values in the current-wave cases. Particularly, when 600<Re<1400, the presence of currents can significantly decrease C_D. When Re>1000, however, for both pure wave and current-wave conditions the C_D value has a very gentle declining trend and the difference between the two conditions is small. In this range of Re, the mean C_D is 1.31 with a standard deviation of 0.22. Following the structure of the empirical relationship in Mendez et al. (1999), a relation between C_D and Re was found as the best fit (R^2=0.89) for all the data obtained from pure wave and current-wave cases (see Figure 2.6d):

$$C_D = 1.04 + \left(\frac{730}{\text{Re}}\right)^{1.37} \qquad 300 < \text{Re} < 4700 \quad (2.18)$$

The tested Re in the pure wave case is in the range of 300-2800, while for current-waves tests it is 670-4700.

2.3.3 Velocity in canopies

2.3.3.1 Mean velocity profiles
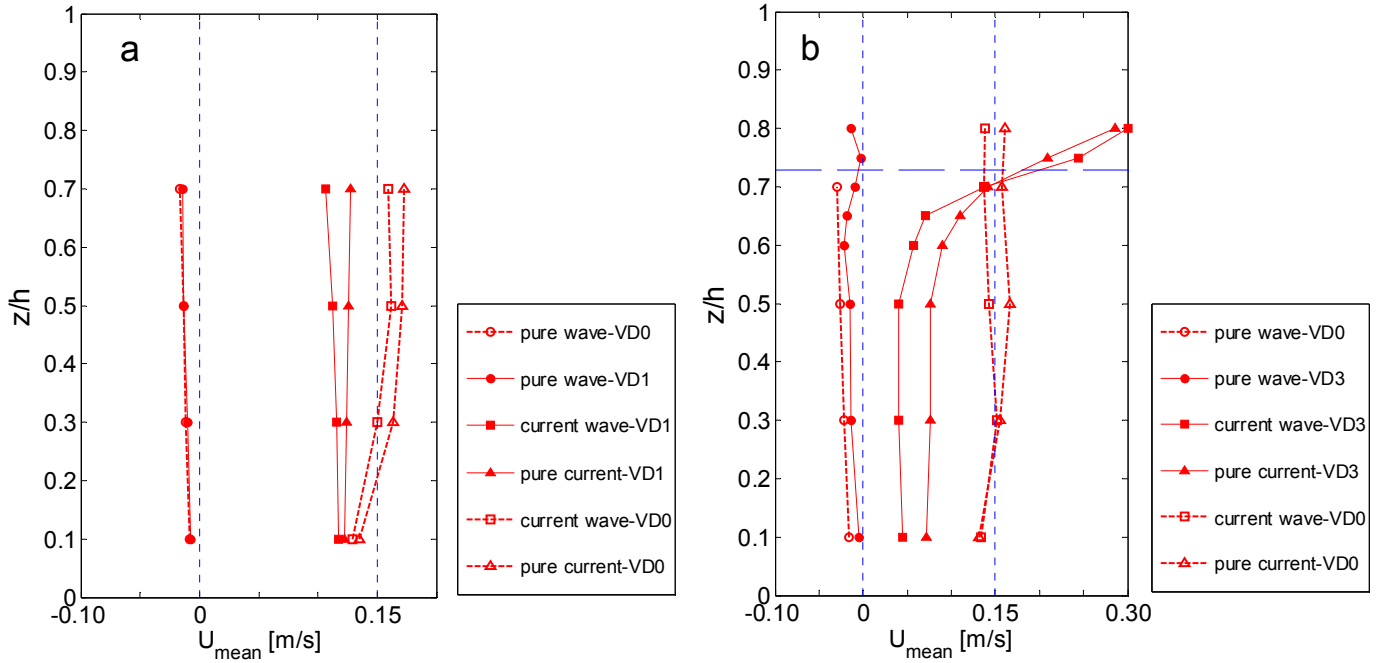
Figure 2.7 Vertical profile of time-mean velocity (U_{mean}). (a) emergent canopy; (b) submerged canopy, the horizontal dashed line indicates the relative height of the canopy. The dotted lines in each panel indicate the imposed U_C is 0 and 0.15 m/s, respectively.

Vertical profiles of mean velocity (U_{mean}) were measured in both emergent and submerged canopies. A U_{mean} that is representative for the entire mimic canopy is obtained by taking its average over the measuring locations at x=27.5 m, 29.5 m and 30.5 m. The emergent (Figure 2.7a) canopy was tested with case wave0612. The submerged canopy was tested with case wave1016 (Figure 2.7b). The measured velocity profiles cover a major part of the water column (z/h = 0.1-0.7 for emergent canopy cases and z/h = 0.1-0.8 for submerged canopy cases). The other parts could not be measured as the EMF probes cannot be used close to the bed or above the wave trough. Figure 2.7a shows that when the emergent canopy (VD1) is subjected to a pure wave flow, a negative U_{mean} exists throughout the measured depth. The variation along the vertical is small. The minimum U_{mean} is -0.014 m/s. A similar negative U_{mean} profile can be found in the control tests (VD0). In the pure current case, the U_{mean} profile in the control test (VD0) resembles a logarithmic profile. However, the presence of the mimic canopy (VD1) can significantly reduce the U_{mean} and result in a uniform profile. The comparison between current-wave and pure current cases suggests that the co-occurring waves suppress the

imposed current velocity (U_c). Evidently, a lower U_{mean} can be found in the wave-current flows compared to that in pure current cases, with the maximum deficit being 0.021 m/s.

The results of the submerged canopy cases (Figure 2.7b) are similar to the emergent canopy cases. The major difference is that a distinctive shear layer exists near the canopy top when following currents exist. In pure wave conditions, a negative U_{mean} still can be found in the submerged canopy. A lower U_{mean} magnitude was also found in the current-wave case compared to that of a pure current case.
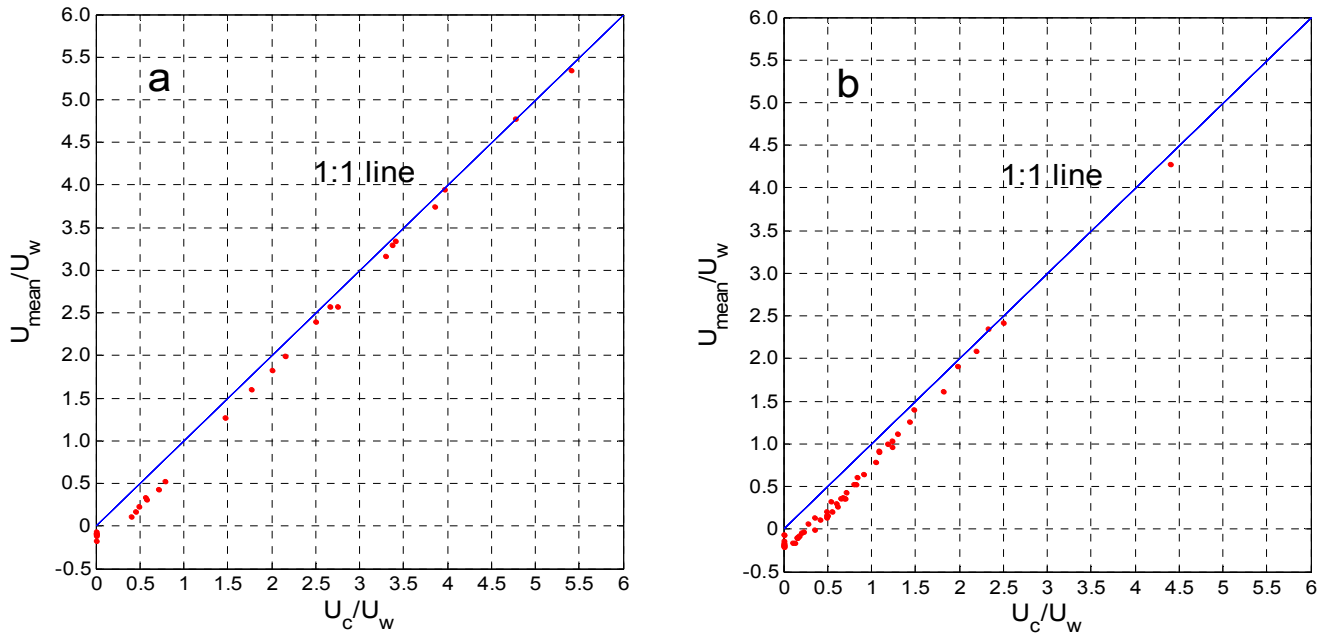
Figure 2.8 Variation of the mean velocity (U_{mean}) with the imposed steady current velocity (U_c): (a) emergent canopy; (b) submerged canopy

Figure 2.8 compares U_{mean} with U_c. Both of them are nondimensionalized by U_w. For most data shown in Figure 2.8, U_{mean}/U_w is smaller than U_c/U_w (i.e. α). It shows that wave motion has a tendency to form a negative velocity and suppress positive current velocities. In the submerged canopy case (Figure 2.8b), when the flow is purely wave driven (U_c/U_w =0), U_{mean} is in the negative directiong so that U_{mean}/U_w is negative. When 0< U_c/U_w <0.35, the negative U_{mean} is counteracted by the imposed positive currents and approaches zero. When 0.35< U_c/U_w <2.3, U_{mean}/U_w shifts towards the positive direction but it is still smaller compared to U_c/U_w. When 2.3 < U_c/U_w, the difference is negligible. The tests with the emergent canopy show a very similar pattern (Figure 2.8a). However, the data from the emergent canopy is more equally distributed, whereas the data from the submerged canopy is mostly in a lower range of U_c/U_w.

2.4 Discussion

Our experimental results show that the effect of following currents on WDV does not vary monotonically with α but shows a decrease followed by an increase. A simple analytical model has been proposed to understand this mechanism. However, modifications to this model appeared necessary to capture the overall WDV variation. The reasons for these modifications lie in the assumptions made regarding drag coefficients and period-averaged velocities. The characteristics of the drag coefficient variation and in-canopy velocities dynamics are the key to understand the WDV variation with following currents.

2.4.1 Drag coefficients obtained by direct measurement approach

A commonly used method to obtain C_D is by calibrating WDV models (e.g. Equation 2.8 and 2.9) against measured wave height decay. This method is prone to introducing modeling errors into the derived C_D. This study applies a direct force measurement approach to derive the C_D, which eliminates the influence of modeling miscalculations. It is noted that even though C_D is derived from a different method, it stems from the original Morison Equation and has the same definition as that derived from the calibration methods.

Since the measurement errors of the instruments are small (about 1%), the accuracy of this method mainly depends on the synchronization of the F and u data. Therefore, in our experiment, the force sensors and EMF were placed at same wave flume cross-sections. Still, a small time lag (ca. 0.05 s) exists in our measurements. This time lag may be induced by small misalignments between the EMF probes and force transducers and/or intrinsic delays of electronic instruments. As the time-dependent C_D is proportional to F_D/u^2, a small phase difference may lead to relatively large errors if u or F_D is close to zero (Figure 2.5). In the major part of a wave period, the influence of this small time lag (0.05 s) is negligible as it is small compare to the tested wave period T (1.0 s-2.5 s). It is important to note that the work done by F_D is proportional to u^3 (Equation 2.12 and 2.13). Thus, in a wave period, the work done by F_D when u equals zero is much less than that when u is near its peak. Therefore, in this study, the period-averaged C_D is obtained by integrating the work done by F_D in a wave period (Equation 2.7). This method automatically assigns less weight to the phase when u is near zero because of its small contribution to the WDV. This way, the obtained C_D is largely determined by the relatively high u and strong F_D in a wave period, which minimizes the influ-

ence of the time lag. Moreover, this method avoids the need for discriminating between F_D and F_M, which may also introduce errors in C_D.

The results show that C_D is negatively correlated to the Reynolds number, which agrees with previous studies (e.g. Augustin et al., 2009; Koftis et al., 2013). However, the Reynolds number Re is defined differently in the present study. In Mendez et al. (1999), the Reynolds number Re* was defined by using U_w in front of the canopy as the characteristic velocity (Equation 2.5)). However, it is apparent that wave height decreases along plant canopies and U_w decreases accordingly. The Re* only takes into account the U_w in front of the canopy, which is not representative of the hydrodynamic conditions inside a canopy, especially when the WDV is high. This may explain the large scatter when C_D is plotted against Re* (Figure 2.6a). In our study, Re is defined using the measured in-canopy velocity U_{max} as the characteristic velocity (Equation 2.4)). U_{max} directly interacts with plant mimics, which is more representative for the hydrodynamic conditions inside a canopy.

When comparing the two different methods of deriving C_D (calibration approach and direct force measurement, presented in Figure 2.6b and 2.6c, respectively), it can be seen that the scatter of C_D is larger between different mimic stems densities following the calibration method. The reason for this may be that the calibration approach assumes that u in a canopy follows the linear wave theory and is not attenuated by the plant stems. In reality, however, u is reduced due to the presence of plant stems and this reduction varies with the plant stem density (Pujol et al., 2013; Stratigaki et al., 2011). The calibration approach neglects such a variation and attributes it solely to C_D, which leads to scattered C_D between different densities. The direct measuring method, on the other hand, collects the in-canopy u data. The variation induced by vegetation density is inherently considered, which results in less spreading of C_D (Figure 2.6c). It is worth noticing that the tested Re in our experiments is 300-4700 and the frontal area per canopy volume is 0.62 m^{-1}, 1.39 m^{-1} and 5.56 m^{-1} for three different mimic stems densities. The dependence of C_D on the mimic stem density is found to be weak in such conditions. With a different range of Re or mimic stem densities, the dependence can be stronger as found in previous studies (Huang et al., 2011; Tanino and Nepf, 2008).

Notably, the direct force measuring technique enables us to obtain the C_D in current-wave flows, which is not possible with the calibration method. To our knowledge, the C_D of mimic vegetation canopies in current-wave flows has not been assessed previously. Our results show that C_D values in current-wave conditions follow the same decreasing pattern as in pure wave

conditions. In general, the presence of a current decreases the C_D since the Re is increased. This finding is consistent with the observation in tests with an isolated cylinder (Sumer and Fredsøe, 2006; Zhou and Graham, 2000). Zhou and Graham (2000) explained that the reduction of C_D was because the vortex formation, shedding and oscillatory motion in pure wave conditions was altered by the imposed steady currents. In pure wave conditions, the vortices act at both the downstream and upstream sides of a stem. When steady currents are present, the vortices are shifted to the downstream side. This results in less obstruction 'seen' by water particles, namely less drag of the flow. To include this phenomenon, we propose an overall empirical relation of C_D for both pure wave and current-wave conditions (Equation 2.18). Such a relation can be useful in understanding WDV and predicting it in numerical modeling studies. For example, if Re > 1000 in a test case, C_D = 1.31 can be a reasonable first estimate. In detailed spectral wave models or phase-resolving models, Re in a canopy can be easily accessed and the value of C_D can be estimated from this relation subsequently.

2.4.2 Wave dissipation in pure wave and current-wave flows

Test results obtained in pure wave conditions show that WDV is higher when the mimic canopies have a higher N and a lower submergence ratio (Figure 2.3a), which is consistent with previous studies (e.g. Stratigaki et al., 2011; Paul et al., 2012; Mendez and Losada, 2004). The main objective of this study, however, is to understand the effect of following currents on WDV, on which the previous two studies have drawn contradicting conclusions (Paul et al., 2012; Li and Yan, 2007). Our study shows that when α is small, following currents generally reduce the WDV. However, when α is sufficiently large, currents can also promote the WDV (Figure 2.4). Hence, it depends on   whether following currents suppress or intensify WDV. The two previous studies investigated WDV in different ranges of α, which caused the seeming inconsistency.

Li and Yan (2007) predicted WDV to increase linearly with the velocity of following currents and such a rise was attributed to wave-current interactions. However, our measured data shows that WDV is only enhanced when α is larger than the corresponding transition points, which are in the range 0.65-1.25 depending on the tested canopy (Figure 2.4). The α tested in the physical experiments of Li and Yan (2007) were all above 1.5. Therefore, WDV reduction by following currents (i.e. r_w<1) in low α was not observed by them. On the other hand, Paul et al. (2012) measured WDV with low α (<0.5) and concluded that WDV was reduced in cur-

rent-wave flow. In our experiment, WDV is only reduced when α is less than its value at the transition points (Figure 2.4).

The variation of U_{mean} with α is also important in understanding the tendencies of WDV. In pure wave conditions, a negative U_{mean} exists in pure wave conditions, which can be explained by the Stokes wave theory (Pujol et al., 2013). Above the wave trough level, the U_{mean} is in the positive direction. In a wave flume with closed boundaries, there must be zero net transport. Hence, below the wave trough level a net negative U_{mean} must exist to compensate for the positive flux above. In pure wave conditions, the non-zero U_{mean} leads to a higher WDV compared to that with idealized velocity symmetry because of the current-wave interaction (Equation 2.14). When a small positive U_c is imposed, it counteracts the negative U_{mean} and forces the overall velocity to be symmetric (Figure 2.5a). The magnitude of U_{mean} is then reduced to zero, which results in a lower WDV (Equation 2.14). As the imposed U_c increases, U_{mean} shifts into the positive direction and starts increasing its magnitude again, which promotes WDV and eventually leads to a higher WDV than that in the pure wave conditions.

The variation of C_D is also closely related to the tendencies of WDV with α. In Figure 2.8b, U_{mean} reaches zero when α is around 0.35. When $0.35<\alpha<0.5$, U_{mean} is in the positive direction and its magnitude is increasing with α. However, WDV (i.e. r_w in Figure 2.4f) does not reach its minimum when U_{mean} reaches zero (i.e. $\alpha=0.35$). It keeps decreasing until it reaches its minimum when $\alpha \approx 0.50$. The further reduction of WDV is induced by the continuous decline of C_D (Figure 2.6d). Hence, the tendencies of WDV are influenced by the combined effects of U_{mean} and C_D variation. By adapting the variation of U_{mean} and C_D with α, the modified model is capable of describing the non-monotonic dynamics of WDV (Figure 2.4f).

Paul et al. (2012) explained the reduction of WDV in current-wave flows by the bending of the non-rigid mimics, which reduces the drag-forming area of the canopy. However, our study used rigid wooden rods as plant mimics, which deform negligibly with the water motion. Nevertheless, the reduction in WDV can still be found when α is small. Hence, such a reduction is not necessarily induced by canopy deformation. The decrease of WDV can also be induced by the reduction of C_D and the magnitude of U_{mean} (Figure 2.6 and 2.8). It is possible that these two factors also played a role in the observed WDV decline in flexible canopies.

Natural salt marsh and mangrove wetlands are often bounded by sea dikes on their landward side. The dikes are closed boundaries similar to those in confined flumes. Thus, the above-

motioned interactions between the wave-induced velocities and tidal currents may also take place in real coastal wetlands. This study shows that the wave dissipation capacity of a certain plant canopy can be reduced as much as 50% when α is around 0.5. During storm events, U_w can be significantly larger than current velocities during a regular flood, which leads to very low α values. As a consequence, the WDV can be significantly reduced in such a scenario. It is important to take into account the possible negative effect of flooding currents on WDV when integrating natural wetlands into coastal protection schemes.

2.5   Conclusions

This chapter primarily evaluated the effect of following currents on WDV by flume experiments. An analytic model was built to understand such effect. It was observed that following currents can affect WDV in all the tested canopies with different mimic stems density and submergence ratio. The effect of following currents on WDV can be either suppressing or promoting, which depends on the ratio between current velocity and the amplitude of horizontal orbital velocity (α). When α is small, WDV is reduced owing to the reduction of C_D and U_{mean} magnitude. When α is sufficiently high, WDV can be strengthened due to current-wave interaction. These observations can explain the contradictive conclusions in the previous studies that investigated WDV in different ranges of α (Paul et al., 2012; Li and Yan, 2007). Our findings suggest that the flooding tide during storm events could be a critical scenario for coastal protection schemes that utilize coastal wetlands to attenuate wave energy. In order to understand WDV, a direct force measurement approach was applied to derive drag coefficient C_D. This method can be applied to obtain the C_D in current-wave flows, which has not been assessed previously. An empirical relation between drag coefficient and Re has been formulated based on the measured data. This relation can be useful for future studies on wave-current-vegetation interaction.

Chapter 3

Windows of Opportunity for saltmarsh vegetation establishment on bare tidal flats: the importance of temporal and spatial variability in hydrodynamic forcing

Zhan Hu, Jim van Belzen, Daphne van der Wal, Thorsten Balke, Zheng Bing Wang, Marcel Stive, Tjeerd J Bouma

Submitted

Abstract

Understanding the mechanisms limiting and facilitating saltmarsh vegetation initial establishment is of widespread importance due to the many valuable services saltmarsh ecosystems offer. However, knowledge on where and when saltmarshes can establish is largely empirical and insights of the governing processes are lacking. Recently, the 'Windows of opportunity' (WoO) concept has been proposed as a framework providing an explanation for the initial establishment of biogeomorphic ecosystems and the role of physical disturbance herein. A WoO is a sufficiently long disturbance-free period following seedling dispersal, which enables successful establishment. By quantifying the occurrence of WoO, vegetation establishment pattern can be predicted. For simplicity sake and as prove of concept, the original WoO framework considers tidal inundation as the only physical disturbance to marsh establishment, whereas the known disturbance from hydrodynamic forcing is ignored. In this study, we incorporate hydrodynamic forcing in the WoO framework. Its spatial and temporal variability is considered explicitly in a saltmarsh establishment model. We used this model to explain the observed episodic marsh recruitment in the Westerschelde Estuary, the Netherlands. Our results reveal that this model can significantly increase the spatial prediction accuracy of marsh establishment compared to a model excludes the hydrodynamic disturbance. Using the better performing model, we further illustrate how tidal flat morphology determines marsh establishing elevation and width via hydrodynamic force distribution. Our model thus offers a valuable tool to understand and predict bottlenecks of saltmarsh restoration and consequences of changing environmental conditions due to climate change.

Highlights

- Temporal and spatial variability in hydrodynamic forcing is key to marsh establishment
- Tidal flat morphology can influence marsh vegetation establishment patterns via hydrodynamic forcing distribution
- Applying 'Windows of Opportunity' concept can assist marsh restoration.

3.1 Introduction

Saltmarshes are important ecosystems providing numerous ecosystem services such as preventing coastal erosion and filtering nutrients from the water (Barbier et al., 2008; Borsje et al., 2011; Temmerman et al., 2013; Marton and Roberts, 2014). Despite their importance, saltmarshes are still degrading worldwide (Coverdale et al., 2013; Hughes and Paramor, 2004; Li et al., 2014). There is increasing need for conservation and restoration strategies to preserve these valuable ecosystems (Bakker, 2012; Lotze et al., 2006). Although the question if saltmarshes may keep pace with sea-level rise by sediment accretion have gained a lot of attention (Fagherazzi et al., 2012a; Kirwan and Megonigal, 2013), understanding of the mechanisms affecting lateral expansion or retreat of salt marshes, such as plants recruitment and cliff erosion is still scarce (Mariotti and Fagherazzi, 2013, 2010; van de Koppel et al., 2005). Especially, processes that enable or disable the initial establishment of saltmarsh vegetation on bare tidal flats are still poorly studied (Balke et al., 2014). Hence, mechanistic insight into these processes is essential for the effective management and restoration of saltmarshes worldwide (Spencer and Harvey, 2012; Viles et al., 2008).

Saltmarsh plant recruitment on bare tidal flats often occurs during episodic events as consequences of interactions between ecological, physical and biogeochemical processes (Wang and Temmerman, 2013; Balke et al., 2014). Typically the suitable elevation for salt marsh establishment is described as an empirically derived minimum elevation (e.g. Wang and Temmerman, 2013; Wolters et al., 2008) mainly arguing with physiological limits of salt marsh plants to inundation stress. Wang and Temmerman (2013) have described in a remote sensing study for the Westerschelde Estuary that a minium elevation of -0.5 m to -0.6 m above local MHWL (Mean High Water Level) is suitable for colonization. Yet, such emprical descriptions do not provide insights into the key mechanisms determining colonization of tidal flats (Balke et al., 2014; Spencer and Harvey, 2012). Therefore, using the empirically-derived elevation threshold to predict vegetation establishment without appreciation of the responsible processes may lead to over- or underestimation of the colonized areas (Wang and Temmerman, 2013).

Recently, Balke et al. (2014) suggested that disturbance free periods of a defined minimum duration, called 'Windows of Opportunity' (WoO), can be identified from time series analysis to hindcast and potentially predict colonization events in ecosystems where new establishment is disturbance-limited. Examples in dunes, floodplains, mangroves and salt marshes

suggested that wind and water movement is needed to disperse the diaspores to vacant bare areas for colonization. And yet, the same processes also can inhibit seedling establishment as they form strong physical disturbance in these bare areas (Balke et al., 2014). Therefore, the temporal variability of e.g. hydrodynamic forcing to saltmarshes is both essential for enabling the colonization of new areas while it may also form the bottleneck to seedling survival after the dispersal. Since the WoO concept provides mechanistic insight, it may become a widely applicable predictive tool for new establishment in coastal marshes and other disturbance-limited ecosystems, once the underlying mechanisms can be correctly reproduced in a modelling approach.

Using a simple tidal-level time series analysis for inundation-free period following a high tide that dispersed the seeds, it was possible to identify a salt-marsh recruitment event on a bare tidal flat (Balke et al., 2014). This analysis however did not account for hydrodynamic stresses that originates from waves and currents. Physical disturbance induced by hydrodynamics (i.e. waves and currents) and associated sediment dynamics (i.e. erosion and deposition at the bed) are known to potentially be main bottlenecks to seedling establishment on tidal flats fronting saltmarshes (Bouma et al., 2009a; Friess et al., 2012; Schwarz et al., 2011; Spencer and Harvey, 2012; Temmerman et al., 2007) and mangroves (Balke et al., 2013a, 2013b, 2011). In order to develop the WoO approach into a powerful predictive tool, it is hence necessary to expand the time series analysis from a solely disturbance-frequency driven analysis that only accounts for water level fluctuations, to a spatially explicit disturbance-frequency and disturbance-magnitude driven analysis that accounts for both water level fluctuations and gradients of hydrodynamic forcing.

A relevant proxy for the hydrodynamic forcing exerted on seedlings and sediment is bed shear stress (BSS) induced by waves and currents (Callaghan et al., 2010). Young seedlings will be exposed to BSS disturbance upon flooding, regardless of their anchorage conditions in the substrate. If the seedlings are still in an early stage with roots of only a few millimetre long, high BSS and associated sediment motion can easily dislodge the seedlings causing failure. However, the tolerance of seedlings to BSS increases with their age and hence root length (Balke et al., 2011; Infantes et al., 2011; Wiehe, 1935). Therefore, we hypothesize that successful seedling establishment on bare tidal flats requires a first WoO consisting of a sufficiently long inundation-free period for germination and initial root anchorage against flooding (i.e., WoO1), as proposed by Balke et al., (2014). This WoO1 needs to be followed by a sec-

ond WoO, in which time-dependent BSS need to remain below a critical value determined by seedling age and hence seedling root length (i.e., WoO2). Disturbance-frequency and disturbance-magnitude are thus considered in WoO1 and WoO2, respectively.

The spatial distribution of BSS over a tidal flat is typically influenced by its bathymetry (Le Hir et al., 2000; Mariotti and Fagherazzi, 2012). We therefore hypothesize that bathymetry is also affecting the disturbance magnitude experienced by establishing seedlings, even if the hydrodynamic boundary conditions are similar. Thus, the morphology of a tidal flat may play an key role in providing abiotic conditions for marshes plants establishment, and may be equally important than the elevation zone and inundation period itself. Tidal flats typically have a contrasting convex or concave shape and different profile slopes (Friedrichs, 2011; Bearman et al., 2010). For different tidal flat profiles, the abiotic conditions for plant establishment can be assessed by the lowest elevation for plant establishment (*LE*). A lower *LE* indicates a more favorable abiotic condition for seedling establishment, which ultimately leads to a larger overall saltmarsh area. Thus, the variation in tidal flat bathymetry may affect the outcomes of saltmarsh conservation and restoration efforts.

The objectives of our study are twofold. *Firstly*, we wanted to test the importance of including the disturbance-magnitude (hydrodynamic forcing) related WoO2 in our ability to predict seedling establishment. Hence, we build two vegetation establishment models with or without considering the WoO2, i.e. WoO1 model versus a WoO1&WoO2 model. These two models were quantitatively compared for their ability to explain observed vegetation establishment patterns on a tidal flat in the Westerschelde estuary, the Netherlands. The spatial-temporal dynamics of BSS at the study site was provided by hydrodynamic modelling, which has been validated against field measurements. *Secondly*, we aimed to gain insights in the effect of tidal-flat morphology on seedling establishment. Hence, we predicted vegetation establishment patterns on schematized tidal flat profiles using a calibrated WoO model. Convex and concave shaped tidal flats with different slopes were tested to find the lowest tidal elevation threshold for plants establishment (*LE*) and associated marsh width. The results of *LE* and marsh width on different profiles are discussed for their importance to restoration and management of salt marshes.

3.2 Method

3.2.1 Alternative models for vegetation establishment based on WoO

To understand initial seedling establishment patterns and test the importance of including hydrodynamic forcing, two analytical marsh establishment models were built. One model solely considers a long enough inundation-free period following a (seed-dispersing) high tide as a 'Windows of Opportunity' (WoO) for seedlings establishment, which will be referred to as the WoO1 model. The other model considers an additional subsequent period (WoO2) when the seedlings are exposed to BSS, i.e. the WoO1&WoO2 model (Figure 3.1). Both models consider seedling survival rather than seed availability as the bottleneck for marsh establishment (Balke et al., 2014; Temmerman et al., 2007; Z. Zhu et al., 2014).
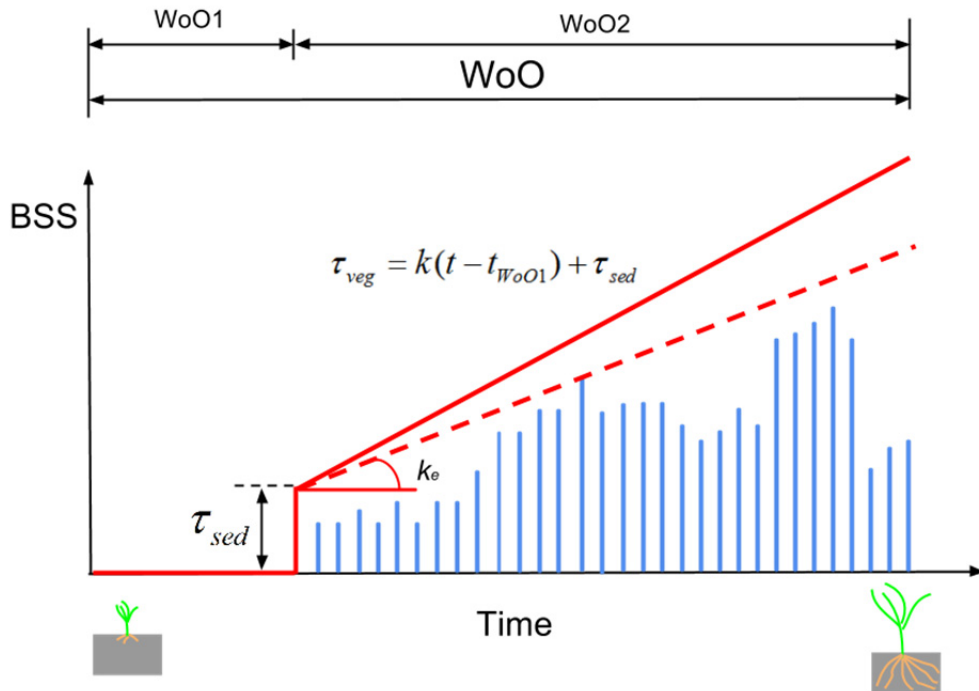
Figure 3.1 Schematization of the perdition based on WoO1&WoO2; WoO1 is an inundation-free period with a critical minimum duration (BSS is zero); WoO2 is a period following WoO1, when the seedlings are experiencing BSS disturbance (the blue line). If during WoO2 the external BSS stays lower than the τ_{veg} (red solid line), then WoO events occur for seedlings establishment. τ_{veg} increases with seedling age because of seedlings roots development, whose increase rate is k. The red dashed line indicates k_e as the maximum slope derived from the BSS time series, which incorporates both magnitude and timing of the external forcing (Equation 3.2). By comparing k_e and external k, we can determine if the disturbance magnitude exceeds the threshold for seedlings survivals in the WoO2.

For the WoO1 model, long inundation-free periods typically occur when the daily high tidal level is declining (i.e., from spring to neap tide). In this phase of the spring-neap tidal cycle, receding water can deliver diaspores to a sufficient high elevation, where inundation disturbance is absent in the following period. For a certain elevation, inundation-free periods can be identified by analyzing time series of the tidal water level. If such an inundation-free period is sufficiently long, then it is regarded as a WoO1 that may enable seedlings establishment. The required minimum inundation-free period is t_{WoO1}, which is the only calibration parameter in the WoO1 model.

The situation that seedling establishment requires both WoO1&WoO2 is schematized in Figure 3.1. As WoO1 is an inundation-free period, BSS is by definition absent (zero). WoO2 is the period following WoO1, when the seedlings are inundated and become exposed to BSS. Its duration is t_{WoO2}. The WoO2 is characterized by the critical BSS for seedlings survival (, τ_{veg}), which describes the plants tolerance to hydrodynamic forcing. If BSS stays below the corresponding τ_{veg} during the WoO2, then seedlings will become successfully established (e.g. Figure 3.1). If the BSS exceeds τ_{veg} at any moment in WoO2, then seedlings cannot be successfully established due to the prohibitive disturbance. At the seedlings initial growing stage, we assume τ_{veg} increases linearly with time following dispersal due to seedling root development (Balke et al., 2011). τ_{veg} is greater than the critical BSS for sediment motion initiation (τ_{sed}), as the forcing needs to be at least strong enough to mobilize bed sediment in order to dislodge rooted seedlings. Thus, the τ_{veg} function starts at the point (t_{WoO1}, τ_{sed}) and increase linearly over time:

$$\tau_{veg} = k\left(t - t_{WoO1}\right) + \tau_{sed} \qquad (3.1)$$

where t is the age of the seedlings after dispersal in hours; k is the growth rate of the τ_{veg} in Pa/hour. It is related to seedlings root growth, which may be influenced by plants species, temperature, salinity, substrate type and moisture (Mudd et al., 2009; Kirwan and Guntenspergen, 2012; Booth and Loheide, 2012). In this study, k is a calibration parameter, as for saltmarsh plants, the estimates of k have not yet been reported in the literature. Alternatively, based on a flume experiment using mangrove seedlings, a k value can be estimated to be 3.3×10^{-3} Pa/hour (Balke et al., 2011). Due to the uncertainty lays in the k value, a sensitivity

analysis was carried out by varying k in a wide range to assess model robustness and explore its effect on the modelled vegetation establishment pattern.

In order to describe the external BSS forcing conditions in relation to the seedlings development, a slope of BSS can be derived for each time step in WoO2 to incorporate both instantaneous BSS magnitude and its timing. The maximum slope in WoO2 is selected to be the characteristic value (k_e) representing the overall external forcing (Figure 3.1):

$$k_e = \left(\frac{BSS(t) - \tau_{sed}}{t - t_{WoO1}} \right) \qquad (3.2)$$

k_e can be regarded as the required growth rate of a seedling BSS tolerance to the external conditions. Therefore, the comparison between BSS and τ_{veg} can be assessed by comparing k_e and k. If $k_e > k$, the external BSS will then exceed the corresponding τ_{veg} at a certain time step in WoO2. Thus, the external forcing is too severe for seedlings survival. If $k_e \leq k$, the BSS stays below τ_{veg} during the whole WoO2, i.e. the external forcing is mild and suitable for seedling establishment (Figure 3.1). BSS time series are provided by hydrodynamic simulations including both wind waves and tidal currents, which is described in section 3.2.3.

For both vegetation establishment models, saltmarsh establishment pattern can be predicted by quantifying the WoO occurrence during the growing season (e.g. 1st April to 1st Oct, *Balke et al.*, 2014). For a tidal flat transect, prediction can be made for each 1 m segment. If a segment has one or more WoO occurrences, then it is predicted to become colonized (*Balke et al.*, 2014) and it is assigned a value of '1'. If a segment does not have any WoO, it is predicted to stay bare and is assigned a value of '0'. Similar 1/0 distribution treatment will be applied in the vegetation establishment observations to facilitate the model performance evaluation.

3.2.2 Observations of vegetation establishment

To test the two alternative vegetation establishment models, we used observations of vegetation dynamics on a tidal flat (Zuidgors, near Ellewoutsdijk) in the Westerschelde estuary, SW Netherlands (Figure 3.2). The Westerschelde is a meso to macrotidal estuary. At the study site, the mean tide range and mean high water level (MHWL) is 4.1 m and 2.3 m NAP (Normal Amsterdam Peil), respectively (Callaghan et al., 2010). The bare tidal flat in front of the mature saltmarsh is exposed to air at low tide and submerged at high tide with water depth

being 1 m to 3 m. On the mature saltmarsh, the water depth can vary from 0 to 0.6 m. As the tidal flat is on the northern bank of the Westerschelde, it is exposed to the prevailing south-westerly winds. It leads to higher incident waves compared to the tidal flats on the southern bank (Callaghan et al., 2010). At the study site, τ_{sed} is estimated to be 0.15 Pa based on the medium sediment grain diameter ($d_{50} = 85$ μm) (van Rijn, 2007).
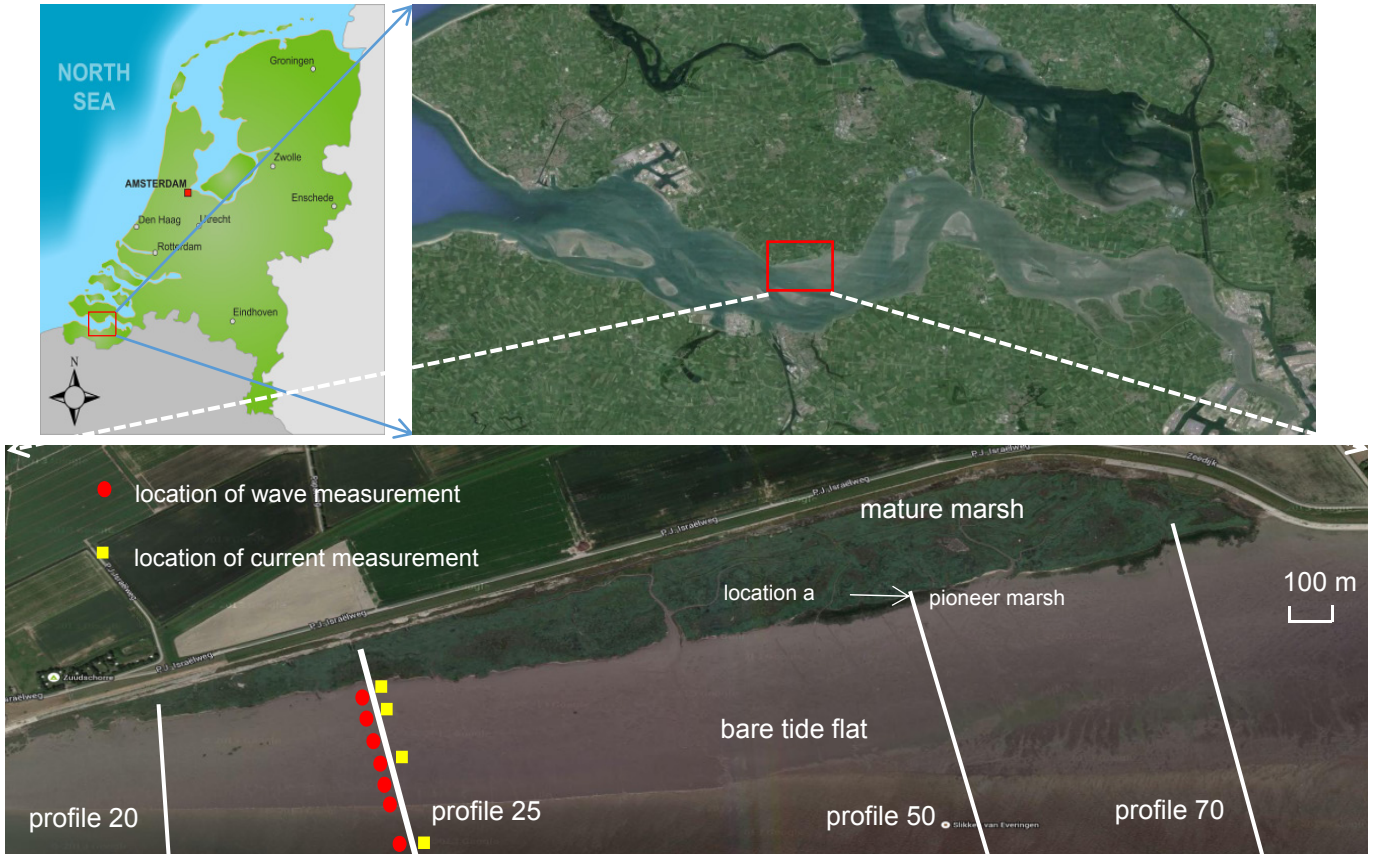
Figure 3.2 Study site near Ellewoutsdijk in the Westerschelde estuary, SW of the Netherlands. Profile 20, 25, 50 and 70 are monitored for vegetation establishment. Hydrodynamics measurements were carried out on the profile 25. Time series of BSS at location a (1.85 m NAP) is shown as examples in the following section 3.2.

The potential pioneer zone is in front of a distinctive saltmarsh cliff. The pioneer vegetation on this tidal flat is predominately *Spartina anglica* with some *Salicornia sp* and *Aster tripolium* in the more densely vegetated areas. The potential pioneer zone was defined as the area from the mature marsh edge (i.e. cliff at ca. 2.2 m NAP) until 1.7 m NAP. The lower boundary of the potential pioneer zone was the elevation threshold suggested by *Wang and Temmerman* (2013) (-0.6 m to MHWL), above which plants have a high chance of establishment. As the lower areas would have very limited chance for establishment, we confined

vegetation cover monitoring and WoO modelling in this potential pioneer zone to avoid inflating model prediction accuracy by including area that is too low to be colonized. The position of the marsh cliff can move landward over time due to lateral erosion. The position change was adapted in the analysis.

Vegetation establishment patterns were obtained along 4 cross-shore profiles from west to east (profile 20, 25, 50 and 70, Figure 3.2) based on aerial photographs. Each profile was divided into 1 m long segments. A segment was considered being successfully colonized by seedlings if it shifts from bare state to vegetated state in two subsequent aerial images. Similar to the WoO models, segments that were colonized are assigned a value of '1', whereas those stayed bare were assigned a value of '0'. Vegetation absence and presence between 2001 to 2013 were classified based on NDVI (Normalized Difference Vegetation Index) from false colour aerial images provided by the Dutch Department of Public Works and Water Management. The aerial images of this area, generally taken on a 1:5000 scale, were taken in 2001, 2004, 2007, 2010, 2011 and 2012. To narrow down the period in which recruitment took place we further used true color images obtained from Google Earth from 2005 and 2013 as supplements. These images were classified based on the Green Excess Index (Richardson et al., 2009).

Elevation (expressed in m NAP) of the intertidal zone from detailed ground levelling was available from the Dutch Department of Public Works and Water Management along profiles 20, 50, and 70 for 2004. In 2012, these elevation profiles were obtained from interpolation of data with 20 m resolution from a combination of airborne laser altimetry and shipborne singlebeam/multibeam bathymetric surveys. The intertidal topography of profile 25 was measured by laser levelling and dGPS equipment in 2004 and 2012, respectively. To facilitate hydrodynamic modelling, profiles were extended downwards till -1.62 m NAP if the original profiles did not reach this seaward boundary elevation, by extracting information from the 20 m resolution surveys in a Geographical Information System.

3.2.3 Hydrodynamic measurements and bed shear stress quantification

3.2.3.1 Wave and tidal current measurement on profile 25

The model including WoO2 requires the information of temporal and spatial BSS variations. This information was provided by means of hydrodynamic modeling. To obtain data for validating the hydrodynamic model, we measured tidal level, wind wave and current velocity

along profile 25 (Figure 3.2). Seven pressure sensors (Coastal Leasing, Inc.) were deployed in October and November 2012 to measure the water level and wave characteristics. They were placed 0.05 m above the seabed at elevations: -1.62 m NAP, -0.64 m NAP, 0.37 m NAP, 1.01 m NAP, 1.43 m NAP, 1.58 m NAP and 1.74 m NAP. Measuring frequency was 4 Hz and measuring interval was 15 minutes. A total of 4096 data points were obtained in each measuring interval. The water level is determined as the mean value measured in an interval. The recorded water level data was compared to the nearby tide gauge at Terneuzen in order to obtain water level data outside the validation period. The wave analysis was based on pressure fluctuations. The attenuation of the pressure signals with water depth was corrected to derive bulk wave parameters, e.g. significant wave height (H_s) and peak wave period (T_P) (Tucker and Pitt, 2001). The obtained H_s data at the edge of the tidal flat (-1.62 m NAP) was linked to wave data measured by a nearby wave pole at Hansweert (i.e., $H_{s\text{-}pole}$) in the estuary. An empirical relation between H_{s_pole} and H_s measured by the most seaward pressure sensor was derived:

$$H_s = 0.58 * H_{s\_pole} - 0.01 \quad (R^2 = 0.62) \quad (3.3)$$

This relation was used to provide wave characteristics outside the wave measuring period for BSS quantification.

Tidal current velocity was measured using 4 Acoustic Doppler Current Profilers (ADCP) from December 2013 until January 2014. They were placed in the seabed at elevations: -1.56 m NAP, 1.06 m NAP, 1.70 m NAP and 1.77 m NAP. The measuring interval was 10 minutes. We conducted harmonic analysis using measured depth-averaged current velocity at the most seaward ADCP and a package of MATLAB routines called T_TIDE (Pawlowicz et al., 2002). In total, 29 main tidal constituents were detected in the dominating long-shore tidal current, which facilitates future tidal velocity predictions.

3.2.3.2 Wave and tidal current modeling

To be able to obtain BSS along the elevation gradient of the whole tidal flat, a hydrodynamic model was constructed to quantify wave height and tidal current velocity. Wind wave propagation on the tidal flats was simulated by a 1D spectral model using Simulating WAves Nearshore (Booij et al., 1999). This model accounts explicitly for wave shoaling, breaking and bed friction processes in varying external conditions. Wave modeling domains were created for

each monitored tidal profile indicated in Figure 3.2. The elevation of the modeling domains was from -1.62 m NAP until the marsh cliff. The grid size of the computation domain is 1 meter, which is the same as the WoO models to enable WoO quantifications. The model was forced by incident waves with a JONSWAP spectrum (Hasselmann et al., 1973), while wind force was excluded. During the field measurement period, incident wave parameters (H_s and peak period T_p) were provided by the most seaward pressure sensor. Outside the field measurement period, H_s data was provided by the long-term wave pole measurements via the empirical relation (3). T_p was assumed to be a constant equal to the mean value in the field measurements (T_p =2.8 s, standard deviation= 0.81 s). Parameters that describe wave propagation processes were set as default values (see http://swanmodel.sourceforge.net/).

Tidal current velocity modeling shared the same computation domains and grid size as the wave model. Cross-shore and long-shore tidal current velocity was modeled separately. The cross-shore current (u_c) was derived by water volume conservation (Friedrichs and Aubrey, 1996). The longshore tidal current at the seaward boundary (u_{l_out} in m/s) was predicted by T_TIDE (Pawlowicz et al., 2002). Subsequently, the longshore tidal current velocity on the shallower tidal flat can be derived by considering balancing the bed friction and longshore water level gradient (Le Hir et al., 2000). Such a gradient is assumed to be uniform on a tidal flat transect since the tide propagation often has a much larger scale than a cross-section of a tidal flat. We further assume that bed friction is proportional to the square of the depth-averaged velocity (Le Hir et al., 2000). The u_l is then determined as:

$$u_l = u_{l\_out} \sqrt{\frac{h}{h_{out}}} \qquad (3.4)$$

where h_{out} is the water depth at the seaward boundary; h is the water depth at a certain location on the tidal flat. Consequently, the total tidal current velocity is:

$$u = \sqrt{u_c^2 + u_l^2} \qquad (3.5)$$

The angle between the tidal current velocity and shore normal direction is:

$$\theta = \tan^{-1}(\frac{u_l}{u_c}) \qquad (3.6)$$

The hydrodynamic model performance is evaluated using the scatter index (*SCI*) and relative bias scores (*Rel.bias*) to compare the model output against in situ measurements, which are defined as:

$$SCI = \frac{\sqrt{\frac{1}{n}\sum_{i=1}^{n}(\Psi_{model}^{i} - \Psi_{obs}^{i})^2}}{\frac{1}{n}\sum_{i=1}^{n}\Psi_{obs}^{i}} \qquad (3.7)$$

$$bias = \sum_{i=1}^{n}(\Psi_{model}^{i} - \Psi_{obs}^{i}) \qquad (3.8)$$

$$Rel.bias = \frac{\sum_{i=1}^{n}(\Psi_{model}^{i} - \Psi_{obs}^{i})}{\sum_{i=1}^{n}\Psi_{obs}^{i}} \qquad (3.9)$$

where Ψ_{obs}^{i} is the data from the observations; Ψ_{model}^{i} is the corresponding model output; n is the number of the total observations. *SCI* and *Rel.bias* give a comprehensive evaluation of the models. The closer *SCI* and *Rel.bias* value to zero indicates a batter model performance. The hydrodynamic model performance was assessed based on two main parameters: H_s and u (Figure 3.3). The *SCI* and *Rel.bias* values of both parameters are close to zero showing a good model performance. It is noticed that the tidal current model underestimates the high current velocities at the most seaward measurement position (at -1.62 m NAP). However, this is not a problem for the present study as it has no effect on the BSS quantification on the upper tidal flat, where colonization might occur. Since the other 3 monitoring profiles in Figure 3.2 are not far from profile 25 (ca. 200 m to 1400 m), it is assumed that the same hydrodynamic model and boundary conditions on profile 25 can also be applied on other profiles.
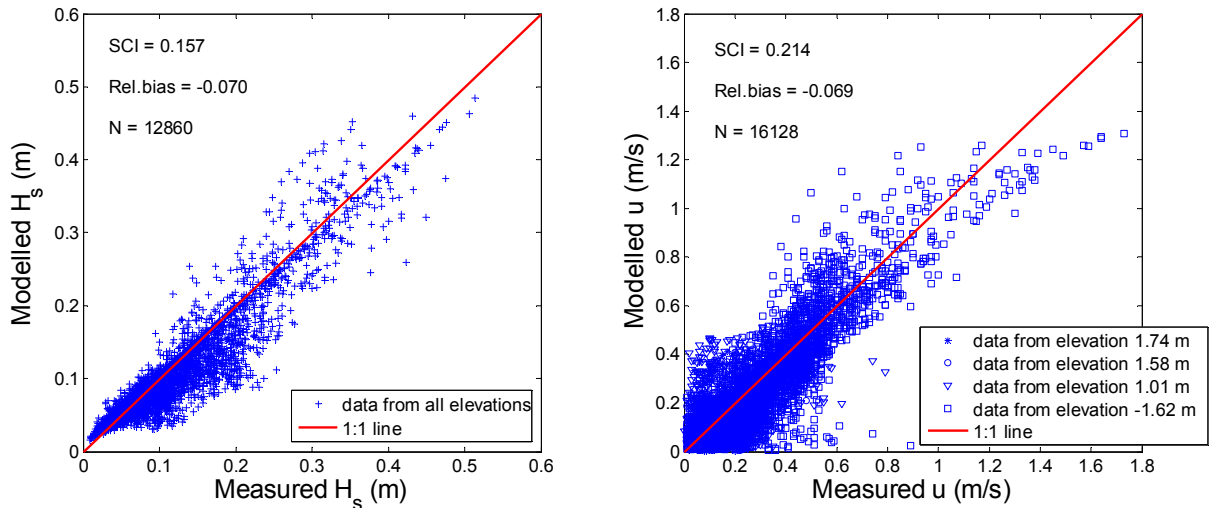
Figure 3.3 Comparison between hydrodynamic modelling results and measurements

3.2.3.3 BSS quantification

The validated hydrodynamic model was used to provide BSS data every half hour on the monitored 4 tidal flat profiles. The magnitude of current induced BSS is (Roberts et al., 2000):

$$\tau_{cur} = \rho f_c u_c^2 \qquad (3.10)$$

where ρ is water density, $f_c = g / C^2$, C is a Chézy coefficient determined as:

$$C = 18 \log_{10}(12h(x)/k_s) \qquad (3.11)$$

k_s is the Nikuradse roughness length $2.5*d_{50.}$ The magnitude of wave induced BSS is (*Soulsby*, 1997):

$$\tau_{wave} = 0.5 \rho f_w u_{wave}^2 \qquad (3.12)$$

where u_{wave} is the root-mean-square value of the maximum orbital motion near the bottom, which is outputted by the SWAN model. f_w is a friction factor estimated as:

$$f_w = 1.39 \left(\frac{\xi}{k_s / 30} \right)^{-0.52} \qquad (3.13)$$

in which ξ is particle excursion amplitude close to the bed, which was also a part of SWAN output. The mean BSS during a wave cycle under combined waves and currents is calculated as (*Soulsby*, 1997):

$$\tau_m = \tau_{cur} \left[1 + 1.2 \left(\frac{\tau_{wave}}{\tau_{cur} + \tau_{wave}} \right)^{3.2} \right] \qquad (3.14)$$

The maximum BSS during a wave cycle is calculated as (*Soulsby*, 1997):

$$\tau_{\max} = \left[(\tau_m + \tau_{wave} |\cos \theta|)^2 + (\tau_{wave} |\sin \theta|)^2 \right]^{0.5} \qquad (3.15)$$

As $\tau_{\max}$ is a measure of the peak hydrodynamic forcing, it is selected to be the representative BSS in the WoO1&WoO2 model, which directly influences seedlings survival prediction. To

avoid the potential errors related to very shallow water, τ_{max} is quantified only when the water depth is larger than 0.1 m.

3.2.3.4 Calibration of WoO models and model selection

In order to evaluate which WoO model is better supported by the observations, we first calibrated both models and then assess their performance by Akaike Information Criterion (AIC). The WoO1 model has only one calibration parameter: t_{WoO1}, while the WoO1&WoO2 model has 3 calibration parameters: t_{WoO1}, t_{WoO2} and k. The calibration is done by tuning the parameters to minimize the total prediction errors of vegetation establishment pattern. Both observations and modeling outputs are expressed as 1/0 distributions. The errors are measured by residual sum of squares (*RSS*):

$$RSS = \sum_{i=1}^{n} (\Psi_{model}^{i} - \Psi_{obs}^{i})^{2} \quad (3.16)$$

where *n* is the number of segments in the potential pioneer zone on the 4 tidal flat transects in Figure 3.2. The 3 parameters in the WoO1&WoO2 model were tuned independently. t_{WoO1} and t_{WoO2} were varied at a half-day step, which resembles the semidiurnal tidal cycles.

It is noted that the two different vegetation establishment models have different degrees of complexity with the WoO1&WoO2 model being more complex than the other one. AIC accounts for both the model performance and model complexity represented by the number of calibration parameters (Johnson and Omland, 2004). Greater model complexity is penalized to ensure a fair comparison between competing models. AIC quantification is carried out as:

$$AIC = n\ln(RSS / n) + 2p \quad (3.17)$$

where *p* is the number of calibration parameters representing the model complexity; A lower AIC score indicates a batter overall model performances. Based on the AIC scores, the probability that one model is the best model among the candidate models can be assessed by Akaike weights (W_i) (Johnson and Omland, 2004):

$$W_i = \frac{\exp(-0.5*(AIC_i - AIC_{min}))}{\sum_{j}^{R} \exp(-0.5*(AIC_j - AIC_{min}))} \quad (3.18)$$

where R is the number of models, i.e. 2; AIC_{min} is the minimum AIC score among a set models.

Like any statistical analysis, AIC assessment requires independent observations to avoid inflating statistical significance. However, observations of tidal flat segments are likely to be correlated with their neighboring segments resulting in spatial autocorrelation (Fortin and Dale, 2005). In order to correct for the autocorrelation and obtained independent datasets, we subsampled the original vegetation establishment dataset at an interval. This interval was determined as the minimum distance between two uncorrelated segments. The degree of correlation between two segments is measured using Moran's I (Fortin and Dale, 2005), which is a function of the distance (d) between the two segments. Moran's I (I) was calculated based on the minimum k_e of each segment as it directly relates to the WoO occurrence:

$$I(d) = \frac{\frac{1}{W} \sum_{h=1}^{n} \sum_{i=1}^{n} w_{hi}(k_{e\_h} - \overline{k_e})(k_{e\_i} - \overline{k_e})}{\frac{1}{n} \sum_{i=1}^{n} (k_{e\_i} - \overline{k_e})^2} \quad h \neq i \quad (3.19)$$

k_{e_h} and k_{e_i} are the minimum k_e from segment h and I; $\overline{k_e}$ is the spatial mean of the k_e of all segments; w_{hi} is a matrix of weighted values; $w_{hi} = 1$, when k_{e_h} and k_{e_i} are from segments of a given distance (d). $w_{hi} = 0$ for all other cases. W is the sum of the w_{hi}. When the $d \geq 5 \, \text{m}$, $I(d)$ drops below value $1/e$. It suggests that two segments are uncorrelated, if they are at least 5 m apart. Such distance is then defined as the interval to subsample the original dataset for independent data. The overall AIC scores were determined by averaging the subsampled data sets.

3.2.3.5   Quantification of BSS and WoO on schematized profiles

In order to explore the influence of tidal flat bathymetry on vegetation establishment, we quantified WoO occurrence on schematized tidal flat profiles. A set of schematized profiles with varying slopes and contrasting shapes was built. For each slope, a convex and a concave profile was tested, to resemble tide and wave dominated tidal flats (Friedrichs, 2011). These profiles were firstly described by a cosine function with amplitude being A (m):

$$f(x) = A \cos\left(\frac{x}{L}\pi\right) \quad -\frac{L}{2} \leq x \leq \frac{L}{2} \quad (3.20)$$

where L is the width of the tidal flat profile; For convex profiles, $A = 1$; For concave profiles, $A = -1$. Secondly, the profiles were rotated around the origin to ensure the upper and lower end of the tidal flat profiles was E_{max} and E_{min} (Figure 3.4). In Figure 3.4, E_{max} and E_{min} is 2.5 m and -2.5 m, respectively. Then, profile slope is $(E_{max} - E_{min})/L$. By varying L from 300 m to 1000 m, different profile slopes ($1/60 - 1/200$) can be achieved. In total, 16 tidal flat profiles with 8 different slopes and 2 different profile shapes (convex or concave) were built.
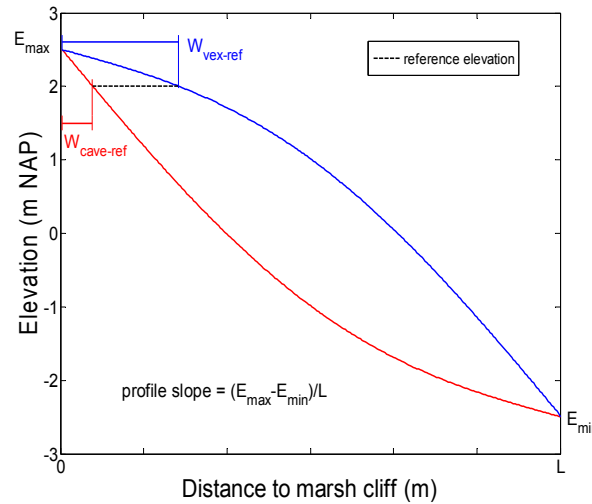
Figure 3.4 Schematized concave and convex tidal flat profiles; The demonstrated two profiles have a same slope as $(E_{max}-E_{min})/L$, where $E_{max} = 2.5$ m NAP and $E_{min} = -2.5$ m NAP respectively, i.e. the elevation of the upper and lower end of the tidal flats; A reference elevation is set to be 2 m NAP as an example; $W_{cave-ref}$ and $W_{vex-ref}$ are the reference marsh width for concave and convex profiles based on the reference elevation.

The vegetation colonization pattern on these profiles was investigated using both the calibrated WoO1 and WoO1&WoO2 to further demonstrate the effect of including the WoO2. For both models, the lowest elevation for plant establishment (LE) and associated marsh width were quantified. LE is determined as the lowest elevation that has WoO events. Accordingly, marsh width is defined as the horizontal distance from profile upper ends till LE. In the WoO1&WoO2 model, time series of water level and wave conditions were provided by the data obtained at the study site to enable BSS quantification on these schematized profiles. When considering hydrodynamic forcing in WoO2, LE can vary with different profile morphology due to the different forcing environment and marsh width will vary accordingly. Assuming LE is constant on different profiles, marsh width is still different on these profiles because of the difference in profile configurations (Figure 3.4). In order to separate the variations in marsh width induced by the different forcing condition from those induced by different profile geometry, we defined a reference marsh width for each profile based on a single

reference elevation (Figure 3.4). The difference between the reference marsh width and the marsh width derived from WoO1&WoO2 model is then the marsh width variation due to different forcing conditions. For concave profiles, the reference marsh width is $W_{cave-ref}$, whereas for convex profile, the reference marsh width is $W_{vex-ref}$. As the WoO1 model only considers the water level fluctuations, the *LE* on different profiles is expected to be constant regardless of the profile bathymetry. Therefore, the *LE* from the calibrated WoO1 model is selected to be the reference elevation (e.g. 2 m NAP in Figure 3.4).

3.3 Results

3.3.1 Vegetation cover monitoring
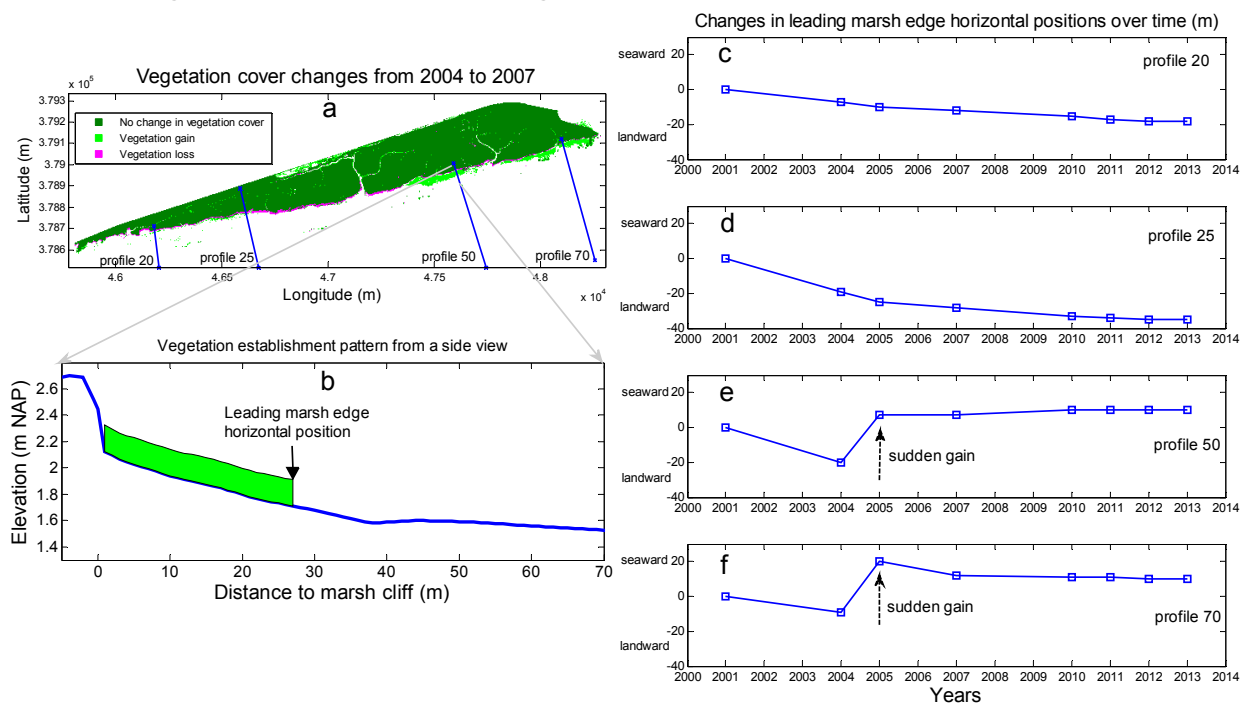
Figure 3.5 Vegetation cover changes monitoring. (a) vegetation cover change from 2004 to 2007; (b) side view of the vegetation area gain on profile 50. The solid black arrow indicates the leading edge position in 2007, which was on the marsh cliff in 2004; (c) the changes in leading marsh edge horizontal positions on 4 profiles relative to the position in 2001.

Semi-continuous vegetation cover monitoring using sequential aerial images shows that a sudden gain in vegetation area only occurred on profile 50 and profile 70 during the period 2004 - 2007 (Figure 3.5a and 3.5b). Using a Google Earth image further narrowed down the sudden vegetation recruitment in the period from 2004 to 2005. By tracing the leading marsh edge over time, information of marsh area dynamics on the 4 profiles can be obtained (Figure 3.5). On profiles 20 and 25, the leading marsh edge was moving shoreward with the retreating

cliffs over the whole monitoring period. On profiles 50 and 70, the leading marsh edge also moved shoreward from 2001 till 2004 (Figure 3.5e and 3.5f). In 2004, however, there was seaward propagation of leading marsh edges due to sudden gains in vegetation areas, which was picked up by the observation in 2005. Afterwards, the leading marsh edge on those two profiles became relatively stable.

3.3.2 Time series of BSS
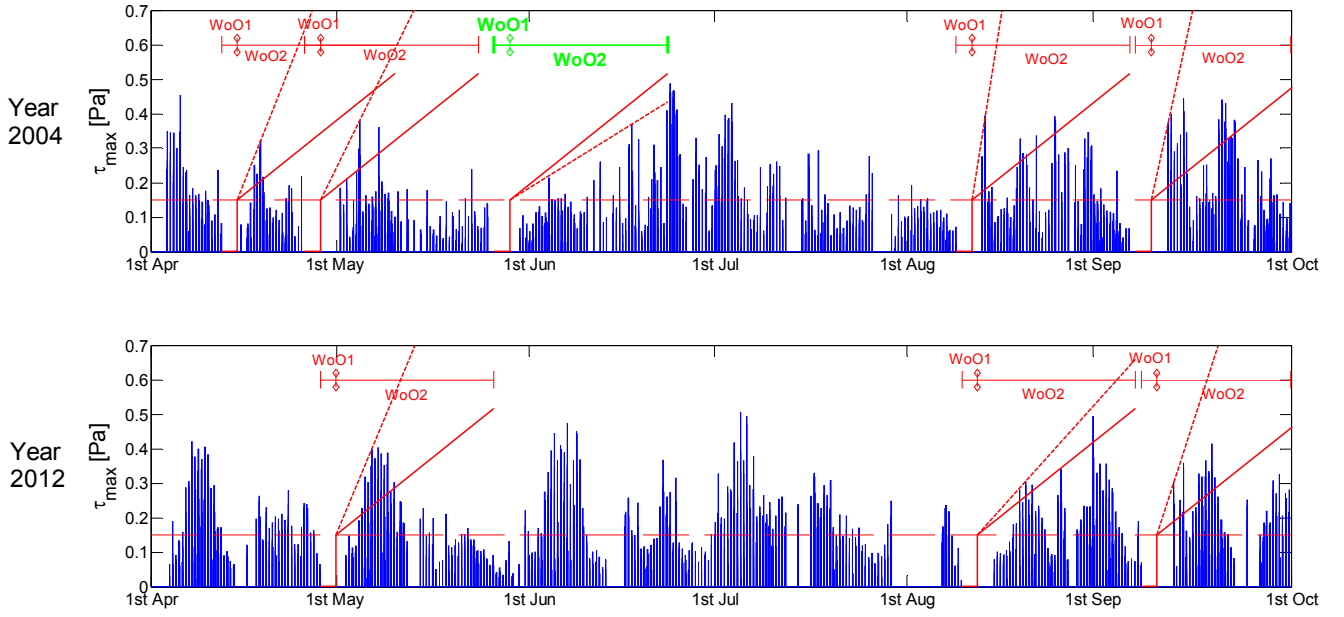
Figure 3.6 Example of $\tau_{\max}$ time series (blue bars) in the growing season (1st Apr to 1st Oct) of year 2004 and 2012 from elevation 1.85 m NAP on profile 50. $\tau_{\max}$ is the maximum wave-current BSS in a wave period. 'WoO1' indicates a inundation-free period t_{WoO1} = 2.5 days ($\tau_{\max} = 0$) and 'WoO2' indicates a period with t_{WoO2} =25.5 days. The red solid line is the calibrated τ_{veg} function with $k = 5.9 \times 10^{-4}$ Pa/hour. These three parameters: t_{WoO1}, t_{WoO2} and k were determined by model calibration in section 3.3. The thick red dashed line indicates k_e derived from $\tau_{\max}$ time series. Only during a period around 1st Jun 2004, $k_e < k$, i.e. $\tau_{\max}$ stays lower than τ_{veg} during the whole WoO2. Thus, this period ('WoO1' and 'WoO2') may lead to marsh recruitment, which is indicated in green. In other periods of both years when $k_e > k$, seedlings may not surpass the WoO2 with high disturbance magnitude. These periods are then indicated in red. The horizontal dashed line indicates τ_{sed}. $\tau_{\max}$ is quantified when water depth is larger than 0.1 m. Thus, in some periods BSS is absent, but tidal inundation disturbance may be present, e.g. the period around 1st Aug, 2012.

In order to understand the relation between hydrodynamic disturbance and vegetation establishment pattern, BSS time series of each segment on the 4 monitoring profiles were quantified during the growing season (Figure 3.6). The fluctuations in the τ_{max} is induced by the co-varying wave and tidal current conditions. Periods with zero BSS in the time series, are due to shallow water inundation (water depth < 0.1 m) during neap tide. For the demonstrated elevation (1.85 m NAP), there are multiple long inundation-free periods (t_{WoO1} = 2.5 days) in both growing season of 2004 and 2012. Subsequent to these periods, k_e can be derived to represent the BSS time series in a WoO2 and compared with a calibrated k (5.9×10^{-4} Pa/ hour), which represents seedling BSS tolerance. The three parameters: t_{WoO1}, t_{WoO2} and k were determined by calibration, which is described in the following section. In 2004, the k_e varies from 5.0×10^{-4} Pa/ hour to 4.7×10^{-3} Pa/ hour. It is noted k_e is lower than the calibrated k in the WoO2 period around 1st Jun, 2004 (indicated in green in Figure 3.6). In 2012, however, all three k_e in WoO2 exceed the calibrated k value. The difference in the BSS time series (represented by k_e) in these two years will lead to different vegetation establishment outcome at this elevation, which is further elaborated in the following section.

3.3.3 WoO models calibration and evaluation

The predictions of the WoO1 model and WoO1&WoO2 model were evaluated based on the overall vegetation cover dynamics in 2004 and 2012 (Figure 3.7). If t_{WoO1} is set to be 5 days, the WoO1 model can predict the observed establishment in 2004 reasonably well ('*pre-5days*' in middle panels of Figure 3.7). However, this setting leads to large overestimations of plant establishment in 2012 ('*pre-5days*' in lower panels of Figure 3.7). If t_{WoO1} is set to be 6 days, the WoO1 model has the best fit of the overall observations ('*pre-6days*' in Figure 3.7). In general, *pre6days* underestimates the plant establishment areas in 2004 and overestimates the areas in 2012. Because t_{WoO1} is increased by one day from *pre5days* to *pre6days*, the predicted colonization areas were reduced. *pre-best* is the prediction from the best-fitted WoO1&WoO2 model (Figure 3.7). It can capture the establishment events in 2004 reasonably well despite an overestimation on the profile 70. In addition, it also predicts the absence of plants establishment at the potential pioneer zone on all the 4 profiles in 2012, which is in a good agreement with the observations. Moreover, there was no establishment in both years on profile 20 and 25. This can be explained by the WoO1&WoO2 model as: in 2004, when the external condition was favorable for establishment, but the elevation on those two profiles was too low to

facilitate establishments; in 2012, however, when the profiles had reached adequate elevation, the external conditions became unfavorable.
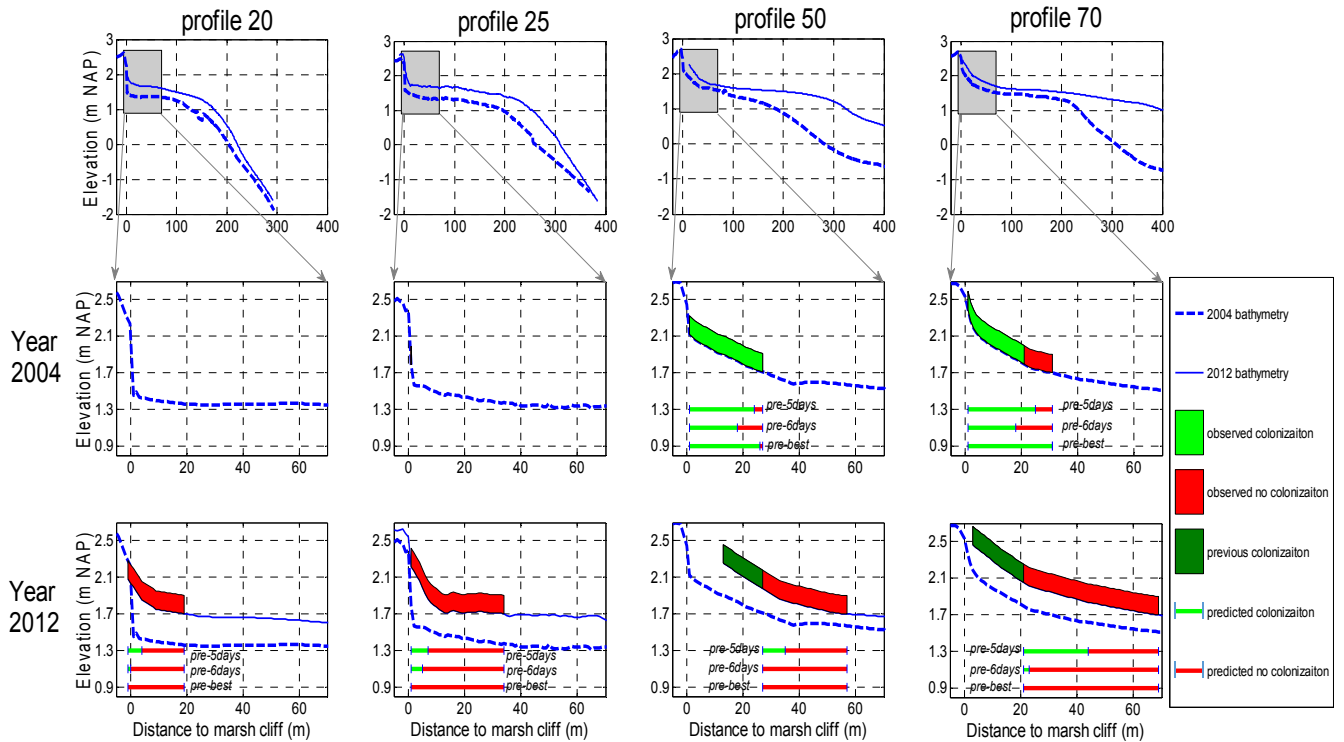
Figure 3.7: Observations and predictions on vegetation establishment pattern on the 4 monitored tidal flat profiles in 2004 and 2012; the upper four panels are the bathymetry of the 4 profiles. The shaded areas in these panels are enlarged in the middle and low panels. The vegetation cover monitoring and predictions also showing in the middle (2004) and lower panels (2012). For all the profiles, 1.7 m NAP is the suggested threshold elevation suggested by Wang and Temmerman (2013), above which the shift from a bare state to vegetated state is likely to occur. The areas above this threshold till marsh cliffs are regarded as potential pioneer zones. Vegetation establishment observations and predictions were confined in these areas. Three prediction are included: *pre-5days* is the prediction of the WoO1 model with t_{WoO1} = 5 days; *pre-6days* is the prediction of the WoO1 model with t_{WoO1} = 6 days; *pre-best* is the best-fit results based on WoO1&WoO1 model; Details of the parameter settings and model evaluation is shown in Table 3.1; Colonization from previous period (in 2004) is not included in the vegetation establishment modeling in 2012.

Based on the vegetation cover changes in 2004 and 2012 on the 4 profiles, model selection procedure using AIC indicates that the WoO1&WoO2 model is better supported compared to the WoO1 model (Table 3.1). The total number of observation points (n) is 193, i.e. number

of segments in the potential pioneer zone in those two years. *pre-best* derived from the best-fitted WoO1&WoO2 model results in minimum errors (RSS=19) among the three predictions. After penalizing for the greater model complexity, the best-fitted WoO1&WoO2 model still has the lowest AIC score and its Akaike weights is as high as 1, indicating this model is un-ambiguously supported by the data despite its higher degree of model complexity. It is noted that the total length of a t_{WoO1} and t_{WoO2} is 28 days, which is the duration of two spring-neap tidal cycles.

Table 3.1 Parameter settings in vegetation establishment predictions and Akaike information criterion (AIC) analysis based on the overall vegetation cover change data from 2004 and 2012 on 4 monitoring profiles.

Prediction	Model	Number of parameters	WoO1 duration (days)	WoO2 duration (days)	k (Pa/ hour)	RSS/n	AIC	Akaike weight
pre-5days	Only WoO1	1	5	-	-	56/193	-44.42	0
pre-6days	Only WoO1 (best fit)	1	6	-	-	30/193	-68.14	0
pre-best	WoO1&WoO2 (best fit)	3	2.5	25.5	5.9×10^{-4}	19/193	-81.50	1.00

3.3.4 Sensitivity analysis of *k*

The parameter k is the increase rate of τ_{veg} for saltmarsh plants (i.e. the resistance against BSS disturbance), which has not yet been reported in the literature due to the still recent discovery of the WoO concept. Considering the uncertainty of k, a sensitivity analysis was carried out to test if the WoO1&WoO2 model prediction varies greatly with different k. The sensitivity analysis is done by quantifying the ratio of the predicted colonization area over the potential pioneer zone area using the WoO1&WoO2 model (Figure 3.8). The ratio can be visualized as the ratio of a horizontal green bar length of *pre-best* in Figure 3.7 over the whole bar length. The increase of k means vegetation can increase τ_{veg} faster and the ratio of colonization area increases accordingly.
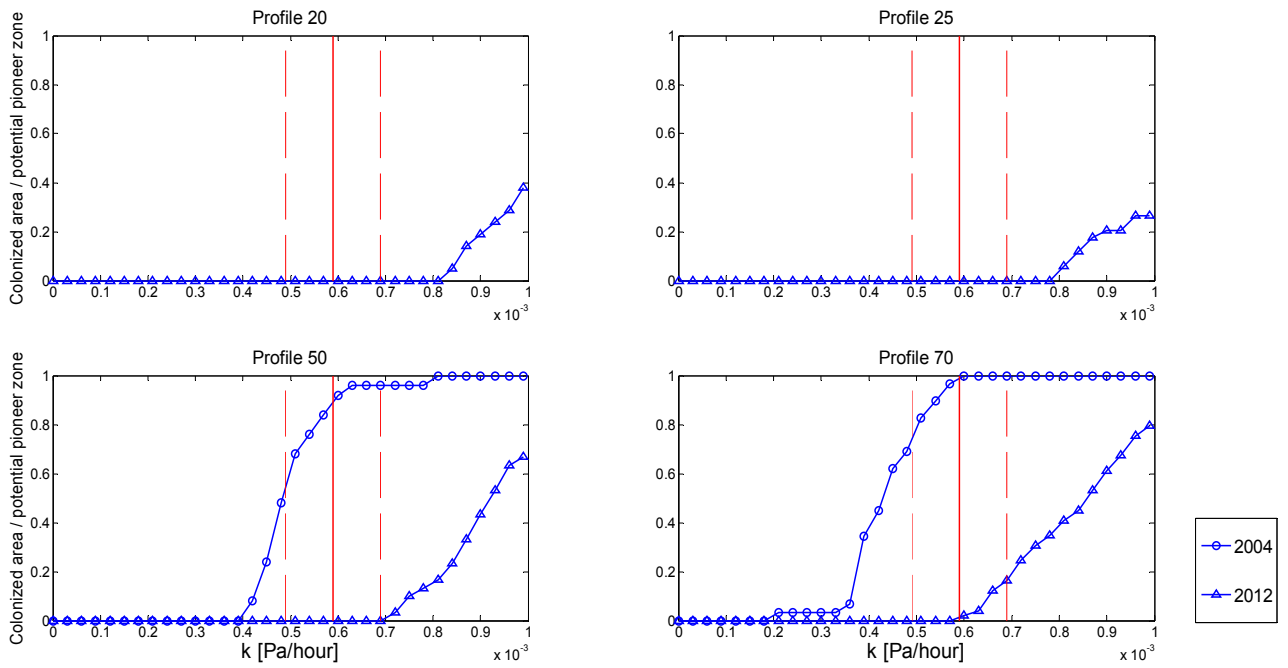
Figure 3.8 Ratio between vegetation colonized area over the potential pioneer zone with varying k, obtained by the WoO1&WoO2 model. The ratio can be visualized as the ratio of a horizontal green bar length of *pre-best* in Figure. 7 over the whole bar length. The best-fitted k value is 5.9×10^{-4} Pa/hour, which is indicated as the red solid line. The two red dashed lines indicate $k = 4.9\times10^{-4}$ Pa/hour and $k = 6.9\times10^{-4}$ Pa/hour, which is about 15% lower and higher than the best-fitted k respectively. There was no potential pioneer zone on profile 20 and 25 in 2004, which is excluded in the sensitive analysis.

The sensitivity analysis shows that the overall model prediction (4 profiles in two years) does not vary significantly if k deviates ca. 15% from the best-fitted value (4.9×10^{-4} Pa/hour - 6.9×10^{-4} Pa/hour) and that the prediction is generally in agreement with the observations (Figure 3.7 and 3.8). In 2004, there was no potential pioneer zone on profile 20 and 25. Those two profiles in 2004 are then excluded in the sensitive analysis. On profile 50 and 70 in 2004, it is predicted that a large portion of the potential pioneer zone was colonized as long as k is in the range of 4.9×10^{-4} Pa/hour - 6.9×10^{-4} Pa/hour, which generally agrees with the observations (Figure 3.8). In 2012, within the same range of k, it is predicted that there is no colonization on all profiles except profile 70, which is also similar with the observations.

3.3.5 BSS distribution and vegetation establishment pattern on schematized profiles

Based on the simple 1D hydrodynamic model, we show that the distribution of τ_{wave} on different profiles is affected by their bathymetry, whereas the distribution of τ_{cur} is not influenced by profile bathymetry, but only determined by the elevation (Figure 3.9a). The τ_{cur} decreases linearly with the increasing elevation and results in similar magnitude of BSS on both profiles. However, τ_{wave} on a gentle convex profile is lower than that on a steep concave profile, even with the same incident wave conditions. The difference is greater in the potential pioneer zone (i.e., zone where elevation > 1.7 m NAP), which may lead to different seedling establishment patterns. The peak of τ_{wave} is where the waves are breaking. From seaward boundary to the wave breaking point, τ_{wave} becomes stronger with the increasing elevation (decreasing water depth) and the difference of τ_{wave} on two profiles also becomes more apparent. The location and the magnitude of the τ_{wave} peak is related to wave propagation processes on the tidal flat foreshore (Green and Coco, 2014).

The difference in τ_{wave} distribution leads to different τ_{max} in the potential pioneer zone (i.e., zone where elevation > 1.7 m NAP) on the schematized profiles (Figure 3.9a and b). In such area, τ_{wave} on gentle convex profiles is generally lower than that on steep concave profiles. The τ_{max} on the gentlest convex profile and that on steepest concave profile become the two extremes with the lowest and highest forcing. The different magnitude of τ_{max} in the potential pioneer zones can influence the predicted vegetation establishment patterns in the WoO1&WoO2 model.

The lowest elevation for plants establishment (*LE*) was predicted to be 1.90 m NAP on all the profiles by the best-fitted WoO1 model (Figure 3.10a). However, the WoO1&WoO2 model predicts that *LE* varies with profile slope and shape (Figure 3.10a). *LE* becomes lower as the profile slope becomes gentler. For concave and convex profiles, the *LE* is reduced by 0.32 m and 0.14 m respectively, when the profile slope drops from 1/60 to 1/200. Furthermore, with the same profile slope, a convex profile has lower *LE* than the corresponding concave profile. The difference in *LE* becomes smaller as the profiles become gentler. Overall, the *LE* is lower on the profiles with lower τ_{max} (Figure 3.9 and 3.10b).
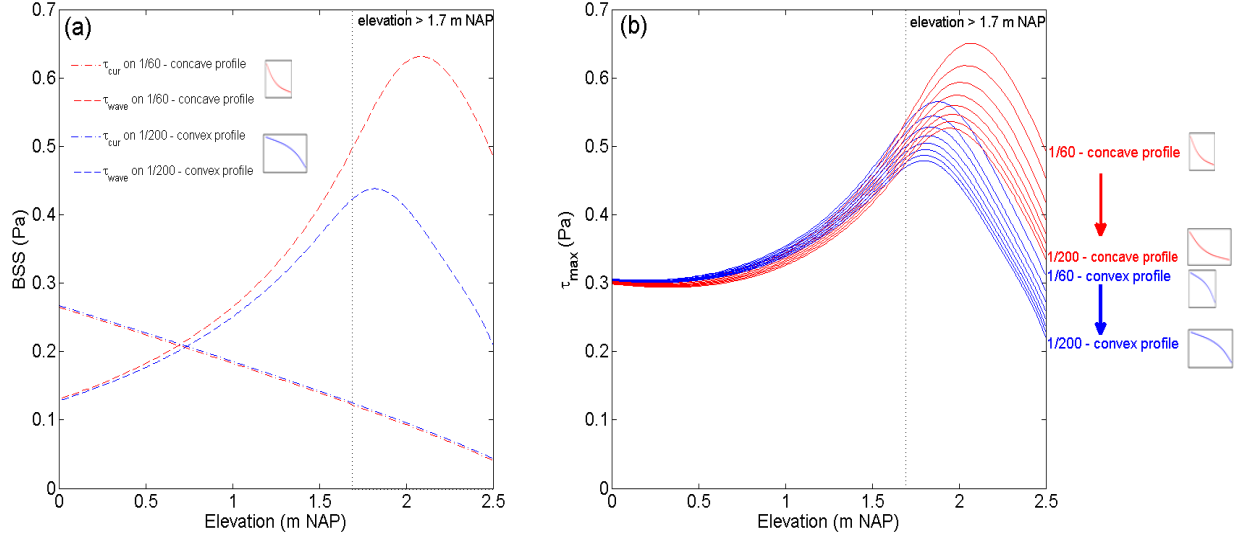
Figure 3.9 Example of BSS distribution on schematized tidal flat profiles. (a) distributions of τ_{cur} and τ_{wave} on two contrasting tidal flat profiles: steepest concave profile (slope=1/60) and gentlest convex profile (slope=1/200) (b) distribution of τ_{max} on all the schematized profiles with varying slope (1/60, 1/80, 1/100, 1/120, 1/140, 1/160, 1/180 and 1/200) and contrasting shapes. The BSS on convex profiles is indicated by blue lines, whereas the BSS on concave profiles is indicated by red lines. The potential pioneer zones (elevation > 1.7 m NAP) are indicated by the dotted line. The insert figures indicate the schematized profiles. The BSS was obtained when tidal level = 2.78 m NAP, H_s = 0.53 m and T_p = 2.8 s.

Corresponding to the *LE* variations*,* the marsh width differs on the schematized profiles (Figure 3.10b). In order to exam the marsh width variation induced by *LE* variations (forcing conditions)*,* the derived marsh width from WoO1& WoO2 modeling is compared to the reference pioneer zone widths ($W_{cave-ref}$ or $W_{vex-ref}$) based on a reference elevation at 1.9 m NAP. The reference elevation is derived from the best-fitted WoO1 model. It is noted that both derived marsh width and reference pioneer zone widths increase with the decreasing profile slope. The increase of the reference pioneer zone widths is due to the profile difference itself, which is also inherent in the increase of the derived marsh width (Figure 3.10b). However, the difference between the derived marsh width and the reference pioneer zone widths is due to the different forcing environments provided by different tidal profiles, which is related to *LE*. As the profile slope decreases, *LE* becomes lower and the difference between the predicted marsh width and reference marsh width becomes larger. Such difference is larger on the convex profiles than that on the concave profiles. This is because the upper part of the convex profile is

very flat (small local slope) and a small variation in elevation may lead to large variation in horizontal distance. Distinctively, marsh width on the convex profile with the minimum slope is 337 m, which exceeds the corresponding $W_{vex-ref}$ by 66 m, i.e. an extra gain in the marsh pioneer zone as large as 24% of the $W_{vex-ref}$.
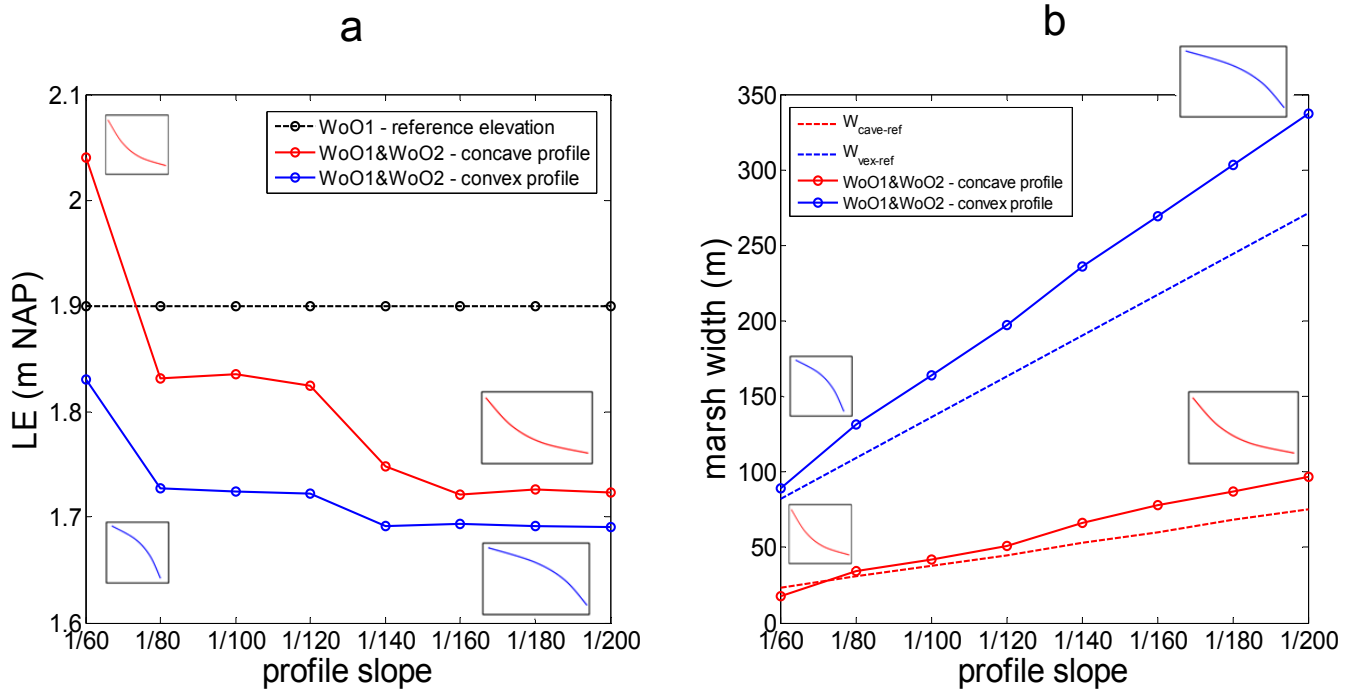
Figure 3.10 The variation of (a) lowest elevation for marsh establishment (*LE*) and (b) marsh width with schematized profile slope and shape. The solid blue and red lines are *LE* and marsh width results on different profiles using WoO1&WoO2 model. $W_{cave-ref}$ and $W_{vex-ref}$ are reference pioneer zone width of concave and convex profiles using a constant *LE* equals to 1.9 m NAP as suggested by the WoO1 model. The insert figures indicate the schematized profile bathymetry.

3.4 Discussion

Monitoring vegetation cover over time shows that vegetation colonization at the study site is episodic rather than gradual, as have been reported in previous studies (Balke et al., 2014; Chen Wang and Temmerman, 2013). This episodic expansion highlights the need of pinpointing the key mechanism that enable or inhibit vegetation survival and establishment. The 'Windows of Opportunity' (WoO) concept provides a framework to understand the occurrence and absence of such colonization events with the external forcing (*Balke et al.*, 2014). Within this study, we show *i)* this WoO concept can be improved by incorporating more than

one process-based WoO, and *ii)* how the derived establishment model can be used to mechanistically explain the relation between marsh establishment extent and tidal flat bathymetry.

3.4.1 The importance of hydrodynamic forcing on marsh establishment

To illustrate the principle of the WoO concept among various ecosystems *Balke et al.* (2014) focused only on the disturbance frequency (i.e., inundation period). For simplicity sake and as a first step, they ignored the influence of the inherent disturbance magnitude (e.g. hydrodynamic forcing). Our study revealed that including additional disturbance magnitude s needed to understand the causes of spatial and temporal variability in colonization events (Figure 3.5 and 3.7). The model incorporates both disturbance frequency and disturbance magnitude in two consecutive WoOs and explained the vegetation recruitment significantly better. This suggests that seedlings not only need to time their initial establishment, set by Wo1, but also need to 'outgrow' the hydrodynamic disturbance, set by WoO2, in order to become successfully established. This finding highlights the regulation effect of hydrodynamics on the seedling survivals, which is in line with the previous field and laboratory studies (Bouma et al., 2009a; Schwarz et al., 2011; Balke et al, 2011). Tidal flat morphodynamic models have shown the biogeomorphic feedbacks between morphological development and vegetation dynamics is important for the long-term tidal ecosystem evolution (Fagherazzi et al., 2012a; Mariotti and Fagherazzi, 2010; Temmerman et al., 2007; van de Koppel et al., 2005). The sediment transport process in these studies is often treated in detail by morphodynamic models (e.g. Delft3D in Temmerman et al., (2007)), but the processes related to vegetation establishment and loss are generally described in an aggregated way. Our marsh establishment model, however, explicitly considers the mechanisms that enable and disable marsh establishment. This will help understanding the consequences of biogeomorphic feedbacks and predicting long-term trajectory in tidal flat morphodynamic models.

3.4.2 Potential consequences of tidal-flat shape for marsh management and restoration

The WoO1&WoO2 model predicts that marsh establishment elevation (*LE*) varies with the profile morphology whereas the WoO1 model and the empirical description in Wang and Temmerman (2013) predict that marsh establishment elevation is constant on different profiles as long as the tide fluctuation is the same. It is shown that tidal flat morphology determines the *LE* for vegetation establishment by affecting hydrodynamic forcing and thereby

affects the overall marsh extent (Figure 3.9 and 3.10). Specifically, the difference in attenuating wave forcing on different tidal flat morphologies will lead to different vegetation establishment patterns. These insights give handles to develop effective conservation and restoration practices for saltmarsh ecosystems.

Saltmarsh restoration and conservation projects normally aim for creating or preserving marsh zone with a sufficient width over a range of elevations to optimize the associated ecosystem services, e.g. habitat provision and wave attenuation (Barbier et al., 2008; Borsje et al., 2011; Hu et al., 2014). The vegetation-establishment modeling on schematized profiles provides three valuable general applicable rules for restoration projects. *Firstly*, it is apparent that convex and gentler profiles are more favorable in hosting large areas of marsh compared to concave and steeper profiles (Figure 3.10b). Hence, when selecting potential saltmarsh restoration sites, not only the elevation zone in an intertidal frame but also tidal flat morphology and associated wave attenuation should be considered, which is also noted in Winterwerp et al., (2013) and Anthony and Gratiot, (2012) for mangrove establishment. *Secondly*, wave forcing is more efficiently dissipated on convex (tide-dominated) profiles than concave (wave-dominated) profiles because the higher foreshore elevation leads to higher dissipation and longer distance from wave breaking points towards the potential pioneer zone (Figure 3.9). This leads to lower elevation of the marsh edge and gain in marsh area (Figure 3.9 and 3.10). Therefore, it is beneficial to create more dissipative foreshores of suitable sites, for example by disposing dredging materials (Temmerman et al., 2013). At locations with benign hydrodynamic forcing, putting dredged sediment can further increase the sediment supply to promote marsh accretion and new marsh establishment (Day Jr. et al., 2007; Temmerman et al., 2013). *Thirdly*, dredging activities near tidal flats should be very cautious, as unexpected loss in potential marsh pioneer area may occur if the bathymetry is altered to be less efficient in dissipating wave energy. Hence, comprehensive assessment of the dredging and dumping activities near marshes are necessary.

3.4.3 Potential consequences of changing boundary conditions

The hydrodynamic forcing experienced within the pioneer zone is of course strongly influenced by the seaward boundary condition (incident wave height, current velocity, etc.). It would be interesting to explore how seedling establishment patterns adjust to long-term boundary condition variations, e.g. the long-term increase of storminess due to climate change (Day et al., 2008; Donat et al., 2011). However, such long-term trend analyses may not pro-

vide input with a sufficient high temporal resolution (e.g. every 30 minutes) as needed for applying the WoO1&WoO2 model. Nevertheless, our results imply that there may be "snow-ball" effects in the relation between saltmarsh establishment opportunity and hydrodynamic boundary variations (Winterwerp et al., 2013; Anthony and Gratiot, 2012). For example, an increase in storminess due to climate change may directly lead to more hostile forcing environment for seedling survival (Balke et al., 2013a; Day et al., 2008; Donat et al., 2011). Additionally, increased wave forcing can lead to more concave tidal flats (Friedrichs, 2011). Therefore, the hostile forcing environment is amplified by the fact that the profile is becoming less dissipative, making the switch back to a favourable condition for establishment even more difficult.

3.4.4 The importance of plant-growth and environmental characteristics for establishment

Within our WoO-model, we used a linear increase rate k to describe how growing seedlings increase their tolerance to τ_{max}, due to the seedling root growth (Balke et al., 2011; Infantes et al., 2011). Similarly, such increase rate has been estimated for mangrove seedlings by Balke et al. (2011). However, their estimation for mangrove-seedlings (3.3×10^{-3} Pa/ hour) is much higher than the calibrated rate k we obtained for saltmarsh plants (5.9×10^{-4} Pa/ hour). This difference may be induced by the fact that mangroves are the tropical species with diapsores and therefore have an inherently much higher (root) growth rate than temperate saltmarsh plants (Saintilan et al., 2014). In reality, the actual occurring seedling root growth is influenced by various abiotic factors such as temperature, salinity and substrate substance (Mudd et al., 2009; Kirwan and Guntenspergen, 2012; Booth and Loheide, 2012). Thus, k may be a spatial-temporal variable depending on the above-mentioned factors. Further field and laboratory studies are needed to provide better estimates of k for various species and various growth conditions. Nevertheless, our sensitivity analysis suggests that the occurrence of vegetation establishment events is not significantly altered if abiotic factors vary within a reasonable range, indicating the uncertainty in k does not greatly affect model robustness in describing the observed vegetation establishment patterns.

3.4.5 Data needed to enable applying the WoO concept to other sites

To apply the WoO concept (WoO1&WoO2 model) to other sites, accurate hydrodynamic modeling and in situ hydrodynamic boundary conditions are needed. In this study, BSS quantification was ensured by the validated hydrodynamic model that takes the combined effect of current and waves into account (Figure 3.3). Hydrodynamic boundary conditions for modeling were provided by the long-term high-frequency tide and wave measurements in the nearby station, which is often not available. In addition, detailed tidal flat bathymetry data or adequate tidal flat profile prediction is required. Frequent vegetation cover monitoring is desirable to record the exact timing of the colonization events in a growing season in order to identify effective WoO events. Finally, in order to further test the WoO concept, it can be valuable to conduct case studies with similar vegetation species and growing conditions but with contrasting hydrodynamic forcing environments; or case studies with similar external forcing conditions but with different growing circumstances.

3.5 Conclusions

In this study, we revealed that including hydrodynamic forcing (as disturbance-magnitude) in the WoO concept is important for understanding and predicting vegetation establishment process. The WoO1&WoO2 model, which considers both the disturbance frequency (WoO1) and the disturbance magnitude (WoO2), can explain the observed vegetation establishment patterns on a tidal flat. This model offers a tool to understand vegetation establishment mechanisms and may predict saltmarsh restoration success under contrasting conditions. Applying this model on contrasting tidal flat profiles shows that marsh plant establishment patterns is influenced by the foreshore bathymetry and related wave force distribution. Gentle convex profiles are more effective in dissipating wave forcing than steep concave profiles, which leads to wider elevation range and larger area for seedling establishment. Therefore, saltmarsh restoration and management projects should not only seek for suitable accommodating elevations, but also favorable foreshore morphology to maximize the vegetation establishment opportunities. Thus, affecting the tidal flat morphology can open up windows of opportunity to restore and manage these valuable coastal ecosystems.

Chapter 4

Continuous monitoring of short-term bed-level dynamics on an intertidal flat: introducing a novel stand-alone high-resolution SED-sensor

Zhan Hu, Walther Lenting, Daphne van der Wal, Tjeerd J. Bouma

Abstract

Tidal flat morphology is continuously shaped by hydrodynamic force, resulting in a highly dynamic bed surface. The knowledge of short-term bed-level changes is important both for assessing sediment transport processes as well as for understanding critical ecological processes such as e.g. vegetation recruitment on tidal flats. High frequency bed-level measurements with a high vertical resolution are generally needed for hypothesis testing and numerical model validation. However, conventional manual bed-elevation measurements tend to have a coarse temporal resolution (weeks to months) due to the labor involved. Existing automated methods for continuous monitoring of bed-level changes either lack a high vertical resolution or are very expensive and therefore limited in spatial application. In light of this, we developed a novel instrument called SED (Surface Elevation Dynamics) sensor for continuous monitoring with a high vertical resolution (2 mm). This sensor makes use of light sensitive cells (i.e. phototransistors) and operates stand-alone. The unit cost and the labor in deployments are reduced, facilitating spatial application with a number of units. In this study, a group of SED-sensors is tested on a tidal flat in the Westerschelde Estuary, the Netherlands. The obtained bed-level changes are compared with the data obtained with precise manual measurements using traditional Sedimentation Erosion Bars (SEB). An excellent agreement between the two methods was obtained, confirming the accuracy and precision of the SED-sensors. Furthermore, to demonstrate how the SED-sensors can be used for measuring short-term bed-level dynamics, two SED-sensors were deployed at two sites with contrasting wave exposure. Daily bed-level changes were obtained including a severe storm event. The difference in observed bed-level dynamics at both sites was statistically explained by their different hydrodynamic conditions. Thus, the stand-alone SED-sensor can be applied to monitor sediment surface dynamics with high vertical and temporal resolution, which provides opportunities to pinpoint morphological responses to various forces in a number of geomorphological environments (e.g. tidal flats, beaches, rivers and dunes).

Highlights

- The novel SED-sensor provides accurate automated monitoring of sediment surface
- This sensor can be applied in various geomorphological environments
- Stand-alone design of the sensor reduces unit cost and deployment labor
- The observed daily bed-level dynamics was related to the prevailing hydrodynamic conditions.

4.1 Introduction

Tidal flats are commonly found in sediment-rich environments with gentle bed slopes (Friedrichs, 2011). Due to the absence of stabilizing vegetation cover, tidal flat topography is continuously shaped by hydrodynamic force from tidal currents and wind waves. As such force has great temporal and spatial variability on short time scales (i.e., hours to days), it may impose short-term surface-elevation dynamics (Green and Coco, 2014; Le Hir et al., 2000). The information of the short-term bed-level changes is important to pinpoint the effect of prevailing hydrodynamic forcing and understand fundamental processes in sediment transport (Friedrichs, 2011; Green and Coco, 2014). Moreover, the short-term dynamics of the tidal flat sediment surface is important for the recruitment of vegetation, microphytobenthos and benthic invertebrates (Balke et al., 2014, 2011; Fagherazzi et al., 2014; Bouma et al., 2001; Nambu et al., 2012), thereby influencing the ecosystem services delivered by tidal flats (Temmerman et al., 2013; Borsje et al., 2011; Foster et al., 2013; Bouma et al., 2014; Fagherazzi and Wiberg, 2009). High frequency bed-level measurements with a high vertical resolution are generally needed for hypothesis testing and numerical model validation in various biogeomorphological studies.

Conventional discontinuous surface-elevation monitoring typically has a coarse temporal resolution (weeks to months), determined by resurvey frequency (Nolte et al., 2013; Lawler, 2008). In tidal flat environments, the discontinuous methods include using erosion pins (Gabet, 1998; Stokes et al., 2010), Surface Elevation Table (SET, (Cahoon et al., 2002), Sedimentation Erosion Bar (SEB, (Van Wijnen and Bakker, 2001) and leveling (e.g. total station theodolite and differential GPS, (Silva et al., 2013). Each method has its own advantages and disadvantages in terms of vertical resolution, ease and cost of covering multiple spots (Table. 1). Nevertheless, none of these methods is suitable in continuously quantifying short-term (e.g. daily) surface elevation changes because of a prohibitively high cost of labor and travelling involved. Elevation can also be assessed with great spatial coverage, using for example airborne laser altimetry (LIDAR) techniques, photogrammetric and Structure from Motion (SfM) techniques (Millard et al., 2013; Fonstad et al., 2013; Mancini et al., 2013). Restricted overpass frequency and limited vertical resolution, however, make such methods less suitable for monitoring individual erosion and deposition events (Table 4.1).

To continuously measure sediment surface dynamics, a range of automated instruments have been developed over the years: the Photo-Electronic Erosion Pin (PEEP) sensor (Lawler,

1991), resistive rods (Ridd, 1992; Arnaud et al., 2009), and acoustic bed-level sensors (Andersen et al., 2006; Ganthy et al., 2013). Of these methods, the acoustic sensors, including ALTUS (Jestin et al., 1998; Ganthy et al., 2013), ADV (Acoustic Doppler Velocimeter, (Andersen et al., 2006)) and PCADP (Pulse-Coherent Acoustic Doppler Profiler, (Q. Zhu et al., 2014)), generally have the highest vertical resolution (within 2 mm), but their application is typically relatively expensive (Table. 1). Furthermore, most of these methods require alongside external power and data logging systems, which leads to high unit cost and labor-intensive deployment. Monitoring at multiple disconnected locations to obtain spatial information is therefore restricted.

We designed a novel stand-alone instrument called SED (Surface Elevation Dynamics) sensor, in order to obtain a high vertical resolution at a reasonable cost. The SED-sensor detects sediment surface position by a dense array of light sensitive cells (i.e. phototransistors) placed as close as 2 mm apart, ensuring a high vertical resolution. Moreover, we supplied this SED-sensor with an internal data-logger and power supply, to enable stand-alone deployment. In this study, we aim to (1) test the performance of this newly developed SED-sensor on an unvegetated, wave exposed intertidal flat and (2) demonstrate how the sensor can be used to measure surface-elevation dynamics with a high temporal (daily) and vertical resolution (2 mm) over a prolonged period of time and (3) test if the observed bed-level dynamics can be related to physical forcing. To achieve these objectives, firstly, we deployed a set of 4 SED-sensors at a single location on a tidal flat, in the SW of Netherlands. The measured surface-elevation dynamics were compared with that obtained with a precise manual measurement: Sediment Erosion Bars (SEB). Secondly, we use these SED-sensors to measure the daily surface-elevation dynamics on two contrasting sites during 1 month. The obtained bed level changes were interpreted in relation to the local tidal and wave conditions measured by alongside wave gauges.

Table 4.1 List of discontinuous and continuous methods used to measure bed-level changes

	Method	Reference (examples)	Estimated vertical resolution (mm)	Typical time resolution	Price range [a] (Euros)	Spatial coverage	Labor	Typical environments
Discontinuous method	SEB/SET	Cahoon et al. 2002; Van Wijnen and Bakker, 2001	0.5-1.5	Weeks - decades	< 100	Spot	High	salt marshes, mangroves, tidal flats, subtidal areas
	Erosion pin	Gabet, 1998; Stokes et al., 2010	~10	Weeks - months	< 5	Spot	High	salt marshes, mangroves, tidal flats, dunes, beaches
	Levelling	Silva et al. 2013	5-25	Weeks - decades	< 25,000	~ 1 km	High	salt marshes, mangroves, tidal flats, dunes, beaches
	Ground-based LIDAR	Nagihara et al. 2004	~ 6	Weeks - decades	< 100,000	~ 0.3 km^2	Medium	salt marshes, mangroves, tidal flats, dunes, beaches
	Airborne LIDAR	Millard et al., 2013; (Glenn et al., 2011)	100-150	Months - decades	< 15,000	> 1 km^2	Medium	salt marshes, mangroves, tidal flats, dunes, beaches
	Photogrammetry/ SfM	(Fonstad et al., 2013; Mancini et al., 2013)	100-200	Weeks - decades	< 5,000	0.1-1 km^2	Medium	tidal flats, dunes, beaches
Continuous method	SED sensor	This thesis	2	Days - months	< 1,000	Spot	Low	salt marshes, mangroves, tidal flats, dunes, beaches
	PEEP	Lawler, 1991; 2008	~ 2.3 [b]	Days - months	< 1,750	Spot	Medium	river banks, gullies, canals, tidal mudbanks
	Electro-resistivity sensor	Ridd, 1992; Arnaud et al., 2009	10-30	Intra tide - months	< 6,000	Spot	Medium	beaches
	Acoustic sensors	Jestin et al., 1998; Ganthy et al., 2013;	1-2	Intra tide - months	< 8,000	Spot	Medium	salt marshes, tidal flats, dunes, beaches, subtidal areas

[a] Prices are for a set of measuring and data logging instruments, based on quotes from corresponding manufactures. For methods that consist of different set of devices (e.g. acoustic sensors includes ALTUS, ADV and PCADP), the listed price was from the method with lowest price. For airborne LIDAR, the price is based on one-time fly passage.

[b] This resolution was obtained in good natural light; it may be different in different light conditions because the calibration and interpolation procedures.

4.2 Materials and methods

4.2.1 SED-sensor

A SED-sensor has a semi-continuous array of 200 light sensitive cells (Figure 4.1). The distance between two adjacent cells is 2 mm, composing a measuring section of ca. 400 mm. The array cells is packed in a transparent tube. The tube as a whole is enclosed in a half-open stainless sheath to increase its durability. The upper and lower part of the SED-sensor is the data logging and battery supply system respectively, which excludes the need for external data logger or power source.
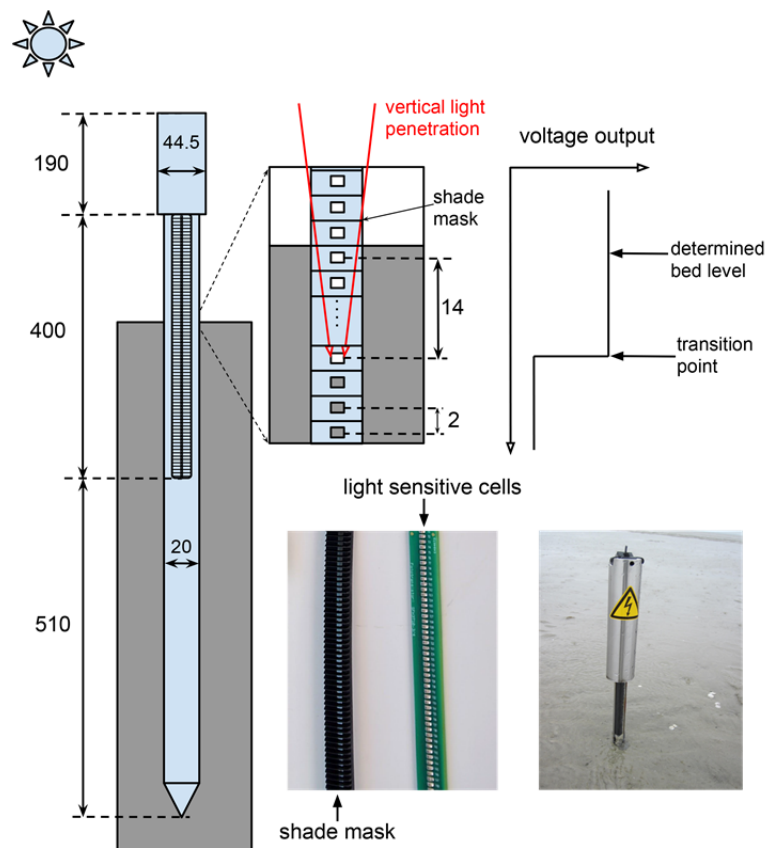
Figure 4.1 Schematized of the SED-sensor in operation. The individual light sensitive cell outputs voltages proportional to their light availability. The aboveground cells and belowground cells should give high and low output accordingly, resulting in a transition point at the bed level. However, light can penetrate vertically into the measuring section just below the bed level, which delays the transition point. A shade-mask is placed to regulate such light penetration. Laboratory and field tests showed with the shade-mask the distance between a transition point and the corresponding bed level was fixed to be 14 mm (i.e. 7 cells). The lower two photos show the array of light sensitive cells, shade mask and SED-sensor deployed in field.

When in use, a SED-sensor is inserted vertically into the seabed, leaving ca. half of the measuring section above the seabed (Figure 4.1). Each light sensitive cell gives a voltage output proportional to its light availability. In this way, aboveground and belowground cells will give higher and lower output accordingly. Near the monitoring bed level, a transition point between low values to high values can be identified in the voltage output (Figure 4.1 and 2). It is noted that lights can penetrate vertically into the transparent tube and reach a few cells just below the bed level. Due to this light penetration, the transition from high to low voltage output does not occur exactly at the bed level. In order to minimize and regulate such vertical light penetration, we placed a customized shade-mask on the cells (Figure 4.1).
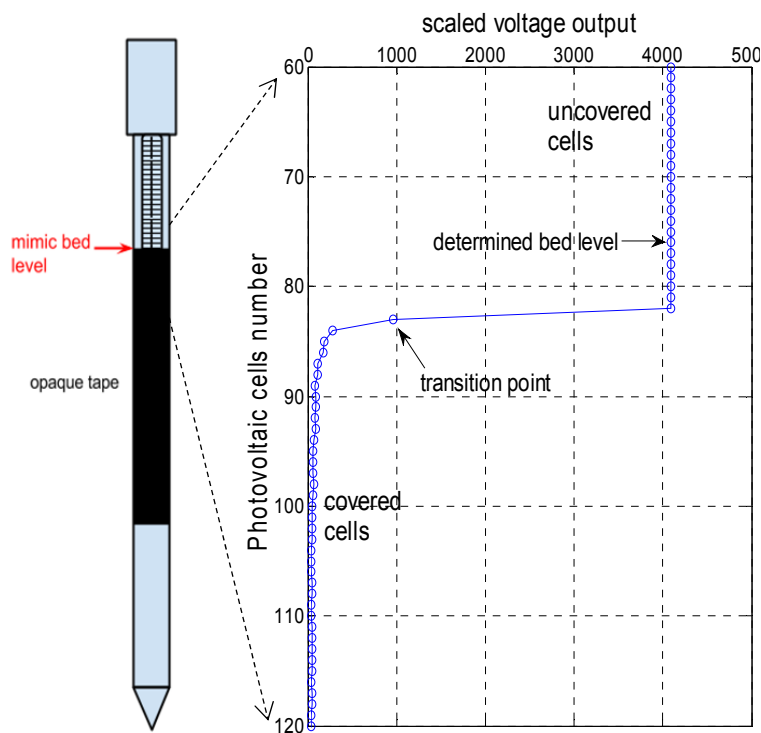
Figure 4.2 Demonstration of how the bed-level can be determined by the SED-sensor, using the 'high sensitive' voltage output mode. The data shown was derived from a test carried out with a low light intensity (15 μmol m^{-2} s^{-1}). Part of the sensor was covered by opaque tape to mimic a fixed bed-level. The output of the uncovered cells is 4095, which is the maximum value that can be restored in 12 bits. The covered cells generally give a much lower voltage output. At the location of the transition point (i.e., going from the covered to uncovered cells), the voltage output difference between two adjacent cells is larger than 500. The mimicked bed level is 14 mm (i.e., 7 cells of 2 mm each) above the transition point. This distance of 14 mm was constant, regardless if ambient light levels were higher (data not shown). The shown data is from a part of the whole 200 photovoltaic cells array.

The voltage output is obtained by measuring currents generated by the light sensitive cells over different resistors. By using resistors with high resistance ($10^6\,\Omega$), medium resistance ($10^4\,\Omega$) and low resistance ($10^2\,\Omega$), three different voltage outputs categorized as 'high sensitive', 'medium sensitive' and 'low sensitive' are obtained in each measurement. For all the categories, the voltage measurement range is from 0 to 3.3 volts and the outputs are scaled proportionally as integers between 0 - 4095 (unsigned 12-bit integers). In the 'high sensitive' output, transition points can be detected even when the measurement is taken with a very low light intensity (e.g. 15 μmol m^{-2} s^{-1} in natural light, see Figure 4.2). In this study, we use the 'high sensitive' output to determine bed levels. The transition point (i.e. going from below-ground to aboveground cells) is determined as where the output difference between two adjacent cells is larger than a threshold value of 500 (corresponding to 0.40 volts) (Figure 4.2). With the shade-mask, the transition point is always, regardless of the light level, 14 mm (i.e. 7 cells) beneath the bed level (i.e., actual transition air to sediment). Such distance and threshold value for the transition point were determined by calibrating the sensor outputs against known bed-level positions (Figure 4.2). For the calibration, we put opaque tape around the sensor to cover a part of its measuring section. The tape edge was then the mimicked bed-level, which is fixed over time. The calibration was done in varying light conditions both in laboratory and on a tidal flat (described in section 2.2) over 3 days. In the field test, we assured the tape edge is well above the actual bed level, so that the mimicked bed level (i.e. tape edge) is constant in time and would not be affected by natural bed level fluctuations.

The measuring interval of the SED-sensor can be set from one second to a few hours, depending on the application. Because of an energy-saving design, even with a measuring interval as short as one minute, SED-sensors with 9 AAA batteries can continuously operate longer than 24 months. The voltage outputs from each interval are stored chronologically as a binary file in a microSD card. One-month deployment of the SED-sensor using one-minute interval only requires 70 MB storage room. Thus, a common microSD card with a memory capacity of 8 GB can provide sufficient storage for deployments last for months to years.

The SED-sensors rely on daylight, and hence do not work during night. When submerged by turbid water, a high sediment concentration layer may be present near the monitoring bed, which hinders determining the bed-level positions. Therefore, data acquired while the SED-sensor is submerged are excluded from analyses. In intertidal environments, the measuring window for the SED-sensors is then at low tide during daytime. The length of a measuring

window depends on the local tidal condition and measuring elevation. The obtained bed-level dynamics is generally the overall change over one or two tidal cycles.

4.2.2 Comparing SED-sensor measurement with the SEB
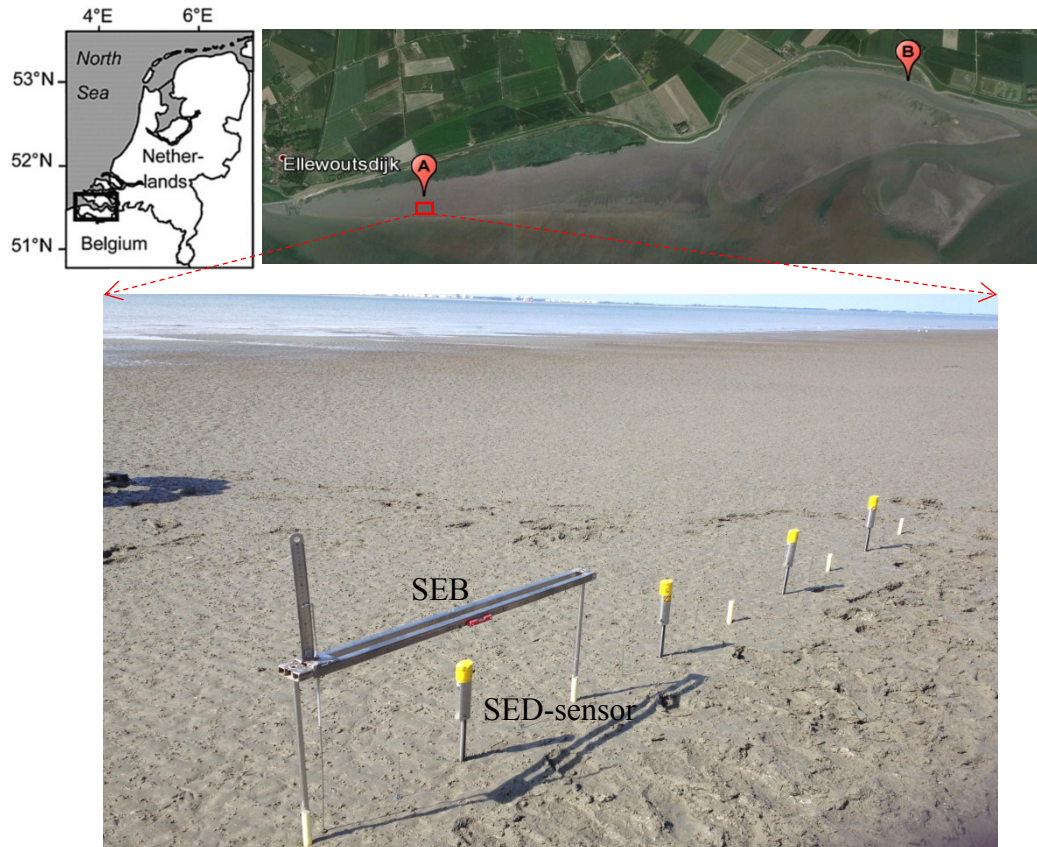
Figure 4.3 Study site and sensors deployments. Top left panel, location of the Westerschelde in SW Netherlands; top right panel, the study site at a tidal flat near Ellewoutsdijk, image from Google Maps; the location of the SED-sensor test is indicated as a red square; 'A' and 'B' are the exposed and sheltered site where bed-level dynamics, tidal level and wave conditions were measured; bottom panel, deployments of SED-sensor and SEB comparison test.

In order to test the performance of the SED-sensor, we compared the SED-sensor measurements with Sediment Erosion Bar (SEB) measurements, a manual approach with an vertical resolution of 0.5 mm (Nolte et al., 2013) (Figure 4.3). Four SED-sensors were placed at a same elevation (- 0.61 m NAP- Normal Amsterdams Peil) on a tidal flat in the, in SW Netherlands. The Westerschelde is a meso to macrotidal estuary. The mean tide range is 4.1 m NAP at the study site and it is exposed to the wave actions induced by prevailing south-westerly winds (Callaghan et al., 2010). The distance between two adjacent SED-sensors was 1 m. Between two sensors, there was a PVC pole mounted for the SEB measurement (Figure 4.3).

To avoid possible disturbance of the seabed near the SED-sensors, the SEB measurements were carried out 50 mm left and right of the SED-sensor. The bed level was then determined by averaging the two readings.

The testing period was from 13 June 2014 till 17 July 2014. SED-sensor measures the bed level dynamics continuously (every minute) during this period, whereas the measurement frequency of the manual SEB approach is limited by the frequency of field campaigns. In the testing period, six field SEB surveys were carried out on: 13 June 2014, 19 June 2014, 27 June 2014, 02 July 2014, 11 July 2014 and 17 July 2014. The SEB observations were done manually when the test location was emerged at low tide. The automatically recorded SED-sensor data in the same windows was used to compare with the SEB observations. In each window (2 hours), there were 120 readings from each SED-sensor. Due the absence of hydro-dynamic disturbance in these windows, the bed-level readings were expected to be constant. However, small reading variations may occur, depending on the water drainage condition on the bed surface. A small amount of water on the bed surface remains to be drained shortly after the receding tide, which can lead to different readings compared to the condition without any stagnant water. As the readings should be constant when the surface water is completely drained, we used the reading that had highest occurrence in a window as an effective SED-sensor measurement point. For both SED-sensor and SEB measurements, bed level changes were determined as the bed level difference between two consecutive surveys. Periods with net erosion were assigned negative values whereas period with net sedimentation were assigned positive values.

4.2.3 Measuring surface-elevation dynamics and hydrodynamics at contrasting sites

To show how the SED-sensor can be used to obtain time series of short-term bed-level dynamics, two SED-sensors were placed at two sites, with similar elevations but contrasting wave exposure conditions (Figure 4.3). The elevation of site A and B is 0.45 m NAP and 0.30 m NAP, respectively. The elevation difference (0.15 m) is considered small compared to the local tide range (4.1 m). Site A, on the western side of the tidal flat, is fully exposed to the wave force, whereas site B, on the eastern side of the tidal flat, is sheltered from waves because of the blockage of a seaward shoal (Callaghan et al., 2010). The measuring interval was also set to as short as 1 minute to be able to capture short measuring windows. An effective bed-level monitoring point was determined as the readings with the highest occurrence in a

window. The measurement period was 1 month, from 12 Oct 2013 till 11 Nov 2013. The obtained bed level time series is compared with the bed level measured at the initial deployment (as t_0). Based on the obtained bed-level time series, the overall dynamics of both sites can be assessed by the standard deviation of these data sets.

At each site, local tidal level and wave condition were measured by a pressure sensor (OSSI-010-003C; Ocean Sensor Systems, Inc.) deployed closed to the SED-sensor. The pressure sensor were placed 0.05 m above the seabed and the measuring frequency was 5 *Hz*. The measuring interval and the measuring period were 15 minutes and 7 minutes, respectively. Thus, 2100 data points were generated in each interval. The mean water level in an interval is determined by averaging all these data points. The wave analysis was based on pressure fluctuations. The attenuation of the pressure signals with water depth was corrected to derive bulk wave parameters, e.g. significant wave height (H_s) and peak wave period (T_P) (Tucker and Pitt, 2001).

To evaluate the relative importance of wave and tidal current forcing at different sites as driver of bed level dynamics, correlation coefficients between bed-level dynamics and corresponding hydrodynamic forcing were quantified. Specifically, the wave and tidal current forcing is represented by the maximum significant wave height (H_s) and peak tidal level in a tidal cycle. Peak tidal level provides a good proxy of maximum tidal current velocity (Bouma et al., 2005). In those cases that two consecutive bed-level observations integrate over two tidal cycles, the maximum H_s and the maximum tidal level in these cycles selected for analysis.

4.3 Results

4.3.1 SED-sensor and SEB measurement comparison

Six field SEB surveys with four replicated measuring locations resulted in (6-1)*4 = 20 data points of surface elevation changes (Figure 4.4). The same amount of SED-sensor data points was obtained using the readings with highest occurrence in corresponding measuring windows. On average, these readings have an occurrence of 57% in each window.

The obtained SED-sensor vs. SEB data points are very close to the 1:1 reference line, which shows a good agreement between SED-sensor and the precise manual SEB measurements. Using the data from the two methods, a fitted regression line can be obtained (R^2=0.89). The slope of the fitted line (1.03) is close to 1 and all the data points fall in the 95% prediction

bands, which further confirms the consistency between the two measurements. This also implies that scouring around the SED-sensor is limited due to the small sensor diameter (20 mm), not a problem for measuring the bed-level dynamics. The small difference between the two measurements is likely caused by the fact that these two instruments did not measure the exact same spots and small-scale sand ripples appeared on the bed surface (see Figure 4.3). Notably, there was some biofilm developing on the SED-sensors during the testing period, but this fouling did not influence the observations with the 'high sensitive' outputs.
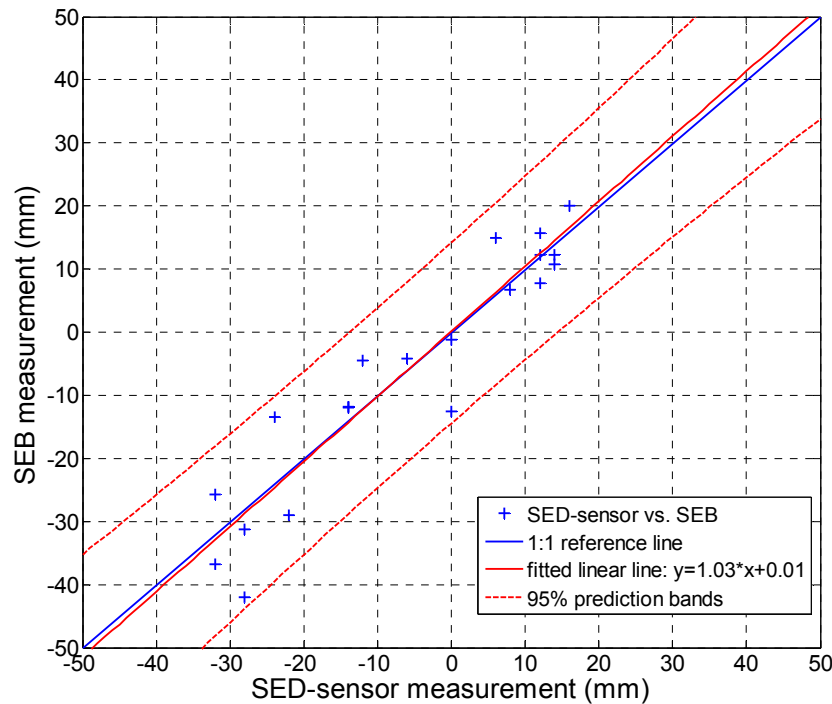
Figure 4.4 Comparison of SED-sensor and SEB measurements; Positive and negative values represent sedimentation and erosion respec-

4.3.2 Surface-elevation dynamics measured by the SED-sensors

In total, there were 41 effective bed-level monitoring points at site A over 59 tide cycles (Figure 4.5). In the same period, there were 31 effective bed-level monitoring points at site B. For most cases (98 %), there was at least one low-tide bed-level monitoring point per day. Thus, the bed-level monitoring at both sites generally provided the bed-level dynamics over one or two tide cycles. There were more monitoring points (measuring windows) at site A than site B due to its slightly higher elevation.

The obtained daily bed-level dynamics at two contrasting sites were interpreted in relation to the wave and tidal current forcing. At the two sites, the tidal fluctuations are similar because of their similar elevations and the short distance between two locations. However, the wave

conditions were significantly different (Figure 4.5). The exposed site A had much higher H_s than the sheltered site B, which leaded to more erosion (bottom panels in Figure 4.5). Remarkably, during St. Jude storm on 27 and 28 Oct 2013, severe erosion was observed at site A. Bed level was lowered as much as 102 mm in two tidal cycles. However, no significant erosion is observed at the site B post the storm, as the seaward shoal greatly attenuated the incident wave height (middle panels in Figure 4.5).
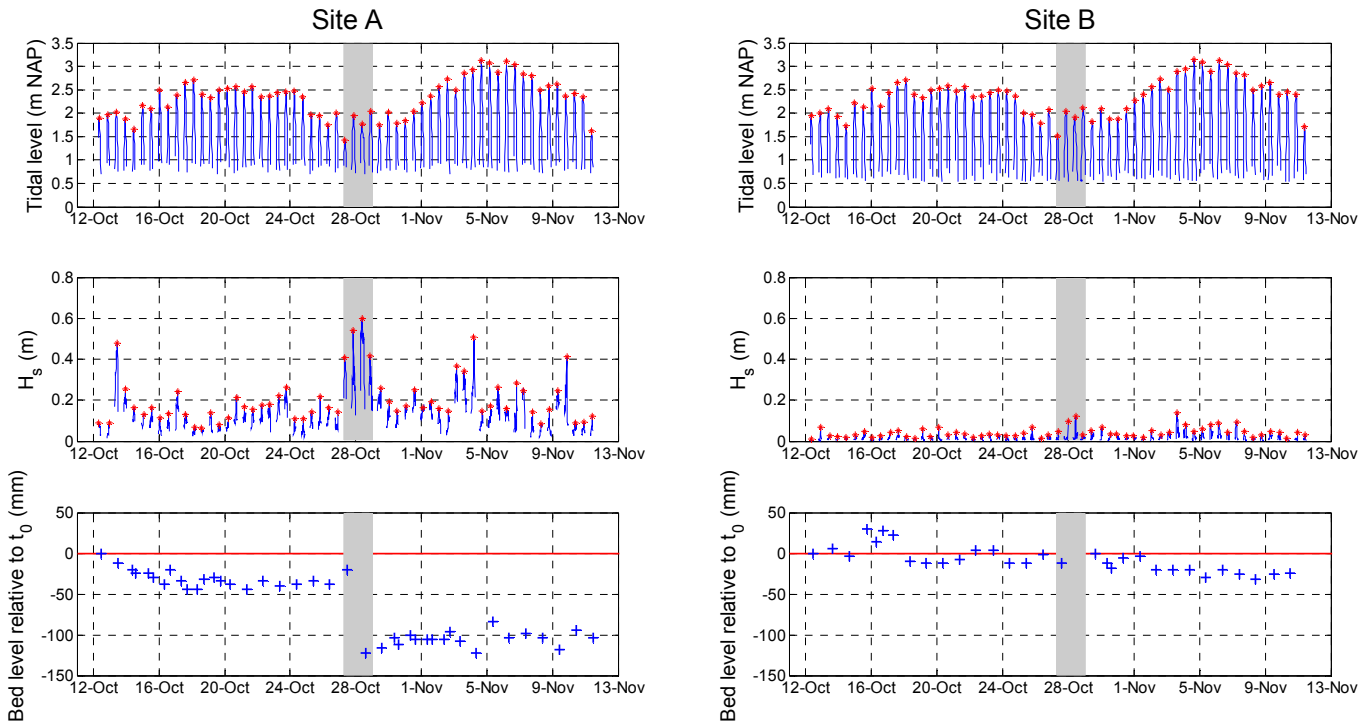
Figure 4.5 Time-series of bed-level dynamics at site A (exposed) and B (sheltered) in relation with the tidal level fluctuations and wave conditions. The red star in the upper and the middle panels are the peak tidal elevation or peak signification wave height (H_s), respectively. The lower panels show the bed level relative to t_0 on 12 Oct 2013. Positive values indicate sedimentation, whereas negative values show erosion. The shaded area indicates a large storm event occurred on 27 and 28 Oct 2013 (St. Jude storm).

In order to evaluate the relative importance of tidal and wave forcing, correlation coefficients between the bed-level changes and the corresponding hydrodynamic forcing was quantified (Table 4.2.). They indicate that the bed level dynamics at the exposed site A is significantly correlated with its wave forcing ($p < 0.05$), whereas the sheltered site B is significantly correlated with the tidal forcing ($p < 0.05$). Therefore, bed-level dynamics at site A and B is primarily related to wave forcing and tidal current forcing, respectively. The correlation coefficients are negative, suggesting that stronger corresponding hydrodynamic force leads to high-

er erosion in the observed bed levels. Furthermore, the overall bed-level dynamics at these two sites can be assessed by the standard deviations. For site A and B, the standard deviation is 39 mm and 17 mm, respectively. Thus, the exposed site A has higher bed-level variations than site B.

Table 4.2 The correlation coefficient between bed-level changes and tidal current or wave forcing; '*p*' is the p-value for testing the hypothesis of no correlation, which is compared with a threshold equals to 0.05. The total number of data points from site A and site B is 41 and 31, respectively.

	Site A	Site B
Tidal current forcing	-0.26 ($p = 0.10 > 0.05$)	-0.45 ($p = 0.01 < 0.05$)
Wave forcing	-0.34 ($p = 0.03 < 0.05$)	-0.26 ($p = 0.15 > 0.05$)

4.4 Discussion

The good agreement between the SED-sensor and SEB measurements shows that the SED-sensor is a reliable method to provide high-resolution bed-level change data. As bed levels can be detected with low light intensity using the 'high sensitive' output of the SED-sensor, the measurement accuracy is not influenced by the varying light condition during daytime or some fouling on the SED-sensors. However, for long deployments covering several months, the SED-sensors may require regular cleaning to prevent excessive fouling.

The frequent monitoring of bed level elevation with the SED-sensor, enables pinpointing the effect of specific hydrodynamic forcing on the tidal flat morphology (Figure 4.5). In rare occasions, the same temporal resolution was obtained using SEB, which reveals highly interesting bed-level dynamics (Yang et al., 2008). Nevertheless, the automated SED-sensor can general offer much higher temporal resolution than that typically cannot obtained from conventional discontinuous measuring methods such as SEB and erosion pins (Van Wijnen and Bakker, 2001; Lawler, 2008). As SED-sensors do not measure in nocturnal or submerged conditions, the effective monitoring frequency in intertidal environments will always be related to the emersion duration, as well as the selected frequency of measurement. But like in our study, this will generally provide sufficient measuring windows to observe the short-term bed-level dynamics and relate it to the prevailing hydrodynamic forcing condition.

Besides bare tidal flats, SED-sensors may also be used to measure the bed level changes in a number of other intertidal and subaerial environments. For example, these sensors are expected to be applicable in saltmarshes and mangroves since the light-reduction by shading from vegetation is likely to be too little to affect the monitoring, whereas other methods (e.g. SfM) may have difficulties in determining bed-level in vegetated areas (Fonstad et al., 2013). Furthermore, since the SED-sensors can be deployed over a prolonged period, they can also be inserted horizontally into the marsh cliff to monitor its rate of retreat. Lastly, the measuring interval of SED-sensors can be set as short as 1 second, which offers an opportunity to monitor aeolian transport on beaches and dunes.

4.5 Conclusions

Results of this study show that the newly developed SED-sensors can accurately monitor short-term bed-level changes originated from sediment erosion and deposition events. The SED-sensor measurement showed an excellent agreement with the most precise manual measurements such as Sediment Erosion Bars (SEB). The time series of bed-level dynamics obtained by using SED-sensors revealed contrasting characteristics at different sites, which could be explained by the contrasting hydrodynamic forcing. While further monitoring is needed to fully reveal the spatial and temporal variability of tidal flat sediment dynamics, our results suggest that the novel stand-alone high-resolution SED-sensor provide a reliable method to monitor bed-level dynamics in a number of environments. The major advantages of the SED-sensors are (1) high vertical resolution monitoring ensured by a dense array of light sensitive cells; (2) suitable for automated continuous long-term monitoring in the intertidal and other environments; (3) stand-alone design with internal power and data-logging systems that reduce the unit cost and deployment labor in large-scale monitoring.

Chapter 5

Predicting long-term and short-term tidal flat morphodynamics using a dynamic equilibrium theory

Zhan Hu, Zheng Bing Wang, Tjerk Zitman, Marcel Stive, Tjeerd Bouma

Abstract

Dynamic equilibrium theory is a fruitful concept, which we use to systematically explain the tidal flat morphodynamic response to tidal currents, wind waves, sediment supply and other sedimentological drivers. This theory stems from a simple analytical model that assumes a uniform bed shear stress distribution on tidal flats leads to morphological equilibrium. A number of field and modeling studies have shown that the tidal flat morphology tends to agree with this analytical model, even though a uniform bed shear stress rarely exists on actual or modeled tidal flats. In the present study, we develop a model based on the dynamic equilibrium theory and its core assumption. Different from the original analytical model, our model explicitly accounts for the spatiotemporal variations of the bed shear stress in order to 1) directly test the dynamic equilibrium theory in general conditions; 2) apply the dynamic equilibrium theory for morphological prediction. To test our model and the embedded theory, we apply the model for both long-term and short-term morphological predictions. The long-term modeling is evaluated qualitatively against previous modeling studies. The short-term modeling is evaluated quantitatively against high-resolution bed-level fluctuation data obtained from a tidal flat in the Netherlands. The model results show good agreement with the qualitative trends and observations, indicating the validity of the dynamic equilibrium theory. Moreover, this model provides a valuable tool to enhance our understanding of the tidal flat morphodynamics and to apply the dynamic equilibrium theory for realistic morphological predictions with spatially and temporally varying bed shear stress.

Highlights

- The dynamic equilibrium theory is tested directly by evaluating the DET-ESTMORF model

- The uniform bed shear stress associated with tidal flats equilibrium can be defined as the shear stress that can keep a constant background sediment concentration in suspension.

- The DET-ESTMORF model is a useful tool for both long-term and short-term morphological modeling

5.1 Introduction

Knowledge of tidal flat morphological evolution is of great importance as it is essential to the long-term sustainability of the intertidal ecosystem and related coastal defense values (Bouma et al., 2014; Kirwan and Megonigal, 2013; Temmerman et al., 2013). Furthermore, the short-term sediment dynamic patterns can influence the opportunity for salt marsh or mangroves plants to (re)establish on the bare tidal flat (Balke et al., 2014, 2011), which is important for coastal wetlands conservation and restoration.

The complex sedimentary mechanisms in the intertidal environments have been studied by numerical modeling (Hunt et al., 2015; Mariotti and Fagherazzi, 2010; Pritchard et al., 2002; Roberts et al., 2000), analytical solutions (Friedrichs, 2011; Friedrichs and Aubrey, 1996) and observations (Fan et al., 2006; Green, 2011; Zhu et al., 2014). Especially, the analytical model of the morphological equilibrium a tidal flat attains under current or wave forcing is a key discovery illustrating the relationship between prevailing hydrodynamic conditions and tidal flat bathymetry (Friedrichs and Aubrey, 1996). In this model, it is assumed that when a tidal flat is in equilibrium, the maximum bed shear stress in a tidal cycle is uniform in space, which leads to zero net sediment transport (Friedrichs and Aubrey, 1996). Based on this idealization, they found that in tide-dominated conditions the equilibrium tidal flat is convex-up, whereas in wave dominated conditions the equilibrium tidal flat is concave-up.

Building on the analytical solution, Friedrichs (2011) further formulated a dynamic equilibrium concept. It elucidates that observed tidal flat morphology approximates a dynamic equilibrium over annual and longer timescales, which is somewhere in between purely tide-dominated (convex) and purely wave-dominated (concave) extremes. On a shorter timescale, however, tidal flat morphology may deviate from that dynamic equilibrium and approach one or the other extreme depending on the prevailing forcing condition. Additionally, tidal flat equilibrium also responds to other sedimentological drivers acting on various time scales, e.g. external sediment supply changes, bioturbation/ bioaggregation, human interference et cetera. (Friedrichs, 2011; Green and Coco, 2014).

A number of observations and modeling studies have shown that large-scale long-term tidal flat morphology generally agrees with the analytical model and the dynamic equilibrium theory (Kirby, 2000; Bearman et al., 2010; van der Wegen and Jaffe, 2014). However, these assessments based on profile morphology are largely empirical and indirect as the analytical

profiles are derived assuming a uniform distribution of maximum bed shear stress. Such an idealized condition rarely occurs on actual or modelled profiles and a stationary equilibrium is in fact exceptional (Pritchard et al., 2002; Tambroni and Seminara, 2012). For instance, tidal flat equilibrium in tide-dominated conditions is often defined as the state when a constant (convex-up) cross-shore profile has been reached (Le Hir et al., 2000; Liu et al., 2011; Pritchard et al., 2002; Pritchard and Hogg, 2003). On such a profile, however, the maximum bed shear stress is in fact only uniform in the subtidal area and it decreases to zero in the intertidal area as the inundation depth reduces (Le Hir et al., 2000; Liu et al., 2011; Pritchard et al., 2002; Pritchard and Hogg, 2003). Such equilibrium is actually not static. The complete tidal flat profile continuously migrates seaward (Liu et al., 2011; Pritchard et al., 2002; Waeles et al., 2004), which cannot be explained by the analytical model. Additionally, due to the schematic nature of the analytical model, the dynamic equilibrium theory cannot be applied for tidal flat morphodynamic prediction with spatially varying bed shear stress.

In this study, we develop a model called Dynamic Equilibrium Theory-ESTMORF (DET-ESTMORF), which is a modification of the ESTMORF model (Wang et al., 2007; Wang and Townend, 2012). The most important feature of the DET-ESTMORF model is that it implements the dynamic equilibrium theory and explicitly accounts for the spatiotemporal bed shear stress variations to predict tidal flat morphodynamics. Following the dynamic equilibrium theory, this model defines idealized tidal flat morphological equilibrium as the state with a uniform bed shear stress distribution. The deviation between the uniform bed shear stress (associated with tidal flat equilibrium) and the actual bed shear stress is then the driver of morphological changes. This feature enables the DET-ESTMORF model to apply the dynamic equilibrium theory and derive tidal flat morphodynamics under the conditions with spatio-temporally varying bed shear stress, which may be not possible for the original analytical model (Friedrichs and Aubrey, 1996).

The aim of this study is: 1) to directly test the dynamic equilibrium theory under spatially and temporally varying forcing conditions by evaluating the DET-ESTMORF model, which is built based on the same theory and its core assumption; 2) to show how this theory can be applied to predict tidal flat morphodynamics. To evaluate the model, we firstly compare the long-term tidal flat morphological modeling with the previous field and modeling studies summarized in (Friedrichs, 2011). Most previous models are process-based (Liu et al., 2011; Pritchard et al., 2002; Roberts et al., 2000). They were developed without explicitly including

the dynamic equilibrium theory. Thus, the comparison between the DET-ESTMORF and process-based models can be an independent test of the theory. Secondly, we tested the model quantitatively by calibrating and validating it against high-frequency bed-level monitoring data obtained on a tidal flat in Westerschelde Estuary, the Netherlands. In the same process of the model testing, we demonstrate how the dynamic equilibrium concept can be applied for long-term and short-term bed-level change predictions.

5.2 Method

5.2.1 DET-ESTMORF model description

Both the original ESTMORF model and the DET-ESTMORF model are hybrid type morphological models. They combine physical process (hydrodynamics and sediment transport) simulations with morphological equilibrium relations to obtain an optimal description of morphological evolutions (Figure 5.1). This differs from fully process-based models (e.g. Delft3D) (Lesser et al., 2004) that predict sediment dynamics purely from elaborating physical processes (e.g. mass and momentum conservation) without explicitly using equilibrium relations.
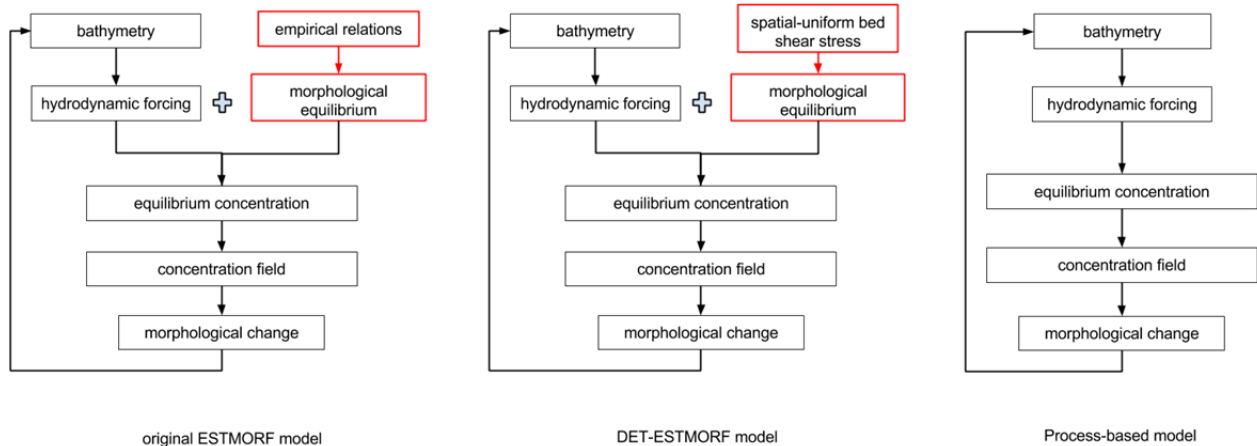
Figure 5.1 Computational procedure of the original ESTMORF model, DET-ESTMORF model and process-based model. The ESTMORF-type models make use of morphological equilibrium relation to derive morphological changes, whereas the process based models derive morphological changes directly without using equilibrium relations. Different from the original ESTMORF model, the DET-ESTMORF model does not rely on empirical relations to derive the morphological equilibrium but follows the dynamic equilibrium theory and defines the equilibrium as the state with spatially-uniform bed shear stress (Friedrichs and Aubrey, 1996).

The philosophy of the hybrid type morphological models is as follows: if all elements in a morphological system are in equilibrium, there is no sedimentation or erosion anywhere in the system. The sediment is assumed mainly transported in suspension. An overall equilibrium concentration c_E can be defined for the whole system. For each element in the system a local equilibrium concentration c_e is defined such that it equals c_E if the element is in morphological equilibrium. If it is larger than c_E, a tendency of erosion exists (i.e. requires more sediment than the average level to reach equilibrium), and if it is smaller than c_E, a tendency for sedimentation exists (i.e. requires less sediment than the average level to reach equilibrium). However, the erosion or sedimentation may not necessarily occur in an element with the corresponding tendency as the morphological changes also depend on the actual sediment transport process. Similar to the process-based models for suspended sediment transport, morphological changes occur when the actual suspended sediment concentration (c) of an element deviates from its local equilibrium value (c_e). Erosion occurs when c is smaller than c_e and sedimentation occurs if c is larger than c_e. The main difference between these two types of model is in the way of determining c_e (Figure 5.1). The ESTMORF type models make use of a morphological equilibrium relation to derive c_e of each element whereas process-based models derive it directly.

The original ESTMORF model has been successfully applied to predict long-term (decades) morphological evolution of estuaries and tidal lagoons (Wang et al., 2007; Wang and Townend, 2012). The morphological equilibrium states were given by empirical relations, e.g. a relation between tidal channel cross-section area with tidal prism volume (Equation (8) in Wang and Townend, 2012). To test the dynamic equilibrium theory, we define the tidal flat morphological equilibrium in the DET-ESTMORF model as the state with a spatial-uniform bed shear stress (τ_E). The τ_E is defined as the bed shear stress that can maintain the constant overall sediment concentration (c_E) in the water column to prevent exchange of sediment with the seabed. Hence, the vertical sediment erosion flux balances the vertical deposition flux, which is similar to the process-based model descriptions (Winterwerp and Van Kesteren, 2004; Amoudry and Souza, 2011):

$$m_e\left(\frac{\tau_E}{\tau_{cr}}-1\right)=c_E w_s \quad (5.1)$$
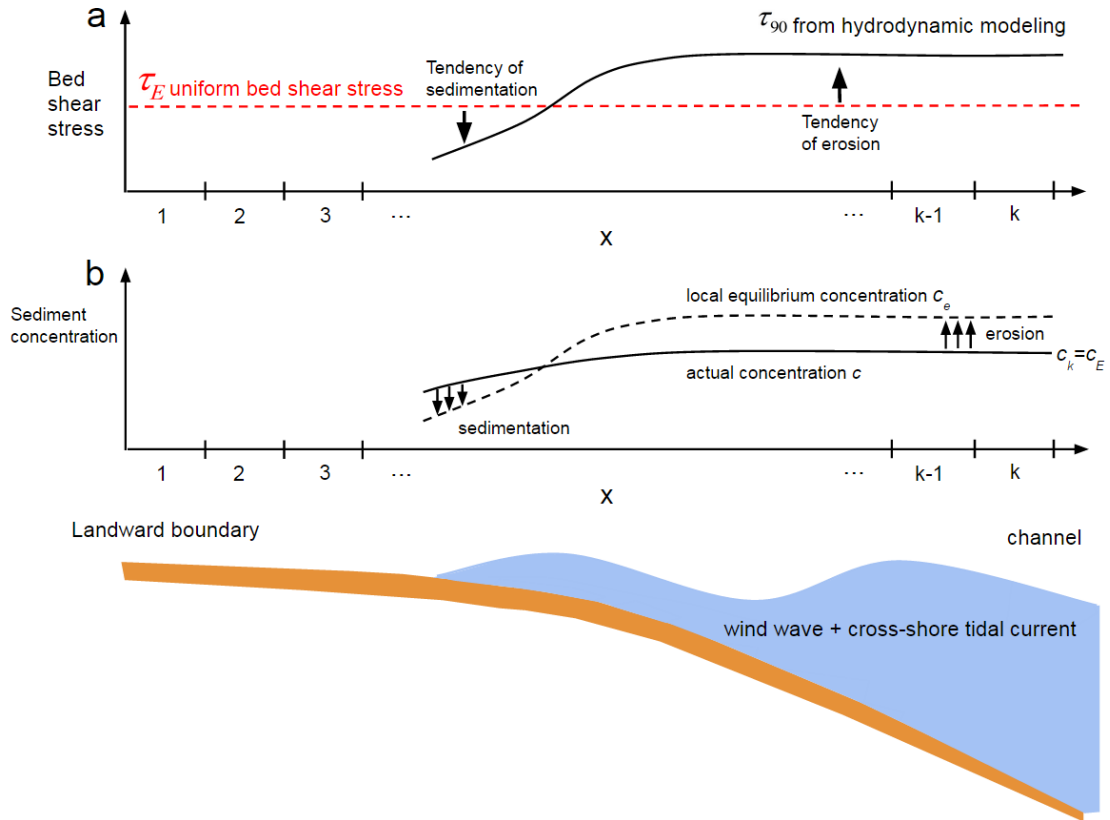
Figure 5.2 The schematization of the DET-ESTMORF model. The total number of elements in the model is 'k'. The top panel shows spatial bed shear stress distribution determines the corresponding morphological evolution tendency. Following the dynamic equilibrium theory, a uniform bed shear stress is defined as τ_E. The representative hydrodynamic forcing is choosing as the 90th percentile bed shear stress in a tidal cycle (τ_{90}). Variations between τ_E and τ_{90} lead to the morphodynamic tendencies, which determines the distribution of local equilibrium concentration (c_e) in the middle panel. The actual sediment concentration field (c) is determined by a sediment transport function, with the concentration at the seaward boundary (c_k) being the overall equilibrium concentration (c_E). The deviation between c and c_e determines the actual morphological changes.

The definition and value of m_e, c_E and τ_{cr} are listed in Table 5.1. Following the philosophy of ESTMORF models, when a stable equilibrium is reached, the actual bed shear stress is equal to τ_E and the actual c equals c_E in the entire domain. If the actual bed shear stress is higher than τ_E, this element has a tendency to erode, i.e. c_e is larger than c_E; if the actual bed shear stress is less than τ_E, the element has a tendency to accrete, i.e. c_e is smaller than c_E, which is summarized in Figure 5.2a and can be expressed as:

$$c_e = c_E \left(\frac{\tau_{90}}{\tau_E} \right)^n \qquad (5.2)$$

where τ_{90} is the 90th percentile bed shear stress in a tidal cycle, which accounts for both the characteristic magnitude of energetic forcing as well as the fraction of time that the forcing are strong (Friedrichs, 2011; Friedrichs and Wright, 2004). n is defined in Table 5.1.

Table 5.1 Parameters definition and values for morphological modeling

Parameter	Description	Value	Reference
n	power in equation (2) for the local equilibrium sediment concentration (-)	2	Wang et al., (2007)
D_{diff}	inter-tidal diffusion coefficient (m^2/s), representing the horizontal mixing process by water motion in a tidal cycle	600	Wang et al., (2007)
w_s	settling velocity for suspended sediment (m/s)	0.0005	Roberts et al., (2000); Liu et al., (2011)
m_e	erosion coefficient (kg/(m^{2}s))	0.00005	Roberts et al., (2000)
ρ_s	sediment density (kg/m^3)	2650	van Rijn, (2007)
ρ	water density (kg/m^3)	1000	
d_{50}	medium sediment grain diameter (μm)	85	Observation [a]
τ_{cr}	critical shear stress for erosion (Pa)	0.15	van Rijn, (2007)
f_c	constant friction factor for currents (-)	0.002	Roberts et al., (2000)

[a] this is the yearly-averaged medium sediment grain diameter (d_{50}) at the study site (Figure 5.3).

The actual sediment concentration field is provided by a mass-balance relation:

$$\frac{\partial(hc)}{\partial t} = w_s(c_e - c) + \frac{\partial}{\partial x}\left(D_{diff}h\frac{\partial c}{\partial x}\right) \quad (5.3)$$

where h is water depth (m); t is time (s); x is the cross-flat coordinate (m), which starts at the landward boundary (Figure 5.2); c is sediment concentration by volume (m^3/m^3), which can be converted to sediment mass concentration (kg/m^3) by multiplication with the sediment mass density ρ_s; Other parameters are defined in Table 5.1. After each tidal cycle, morphological change can be determined by the difference between c and c_e (Figure 5.2b):

$$\frac{\partial z}{\partial t} = \frac{1}{1-p}w_s(c - c_e) \quad (5.4)$$

where z is the bed level, $\partial z/\partial t$ is positive during sedimentation and negative during erosion. p is bed porosity (0.4). The hydrodynamic part of the DET-ESTMORF model provides τ_{90} as an input for morphodynamic modeling. The magnitude of the cross-shore current (u_c) was derived from water volume conservation under a varying surface level elevation (Friedrichs and Aubrey, 1996; Le Hir et al., 2000). As the tide rises, the water line moves landward. This is attended by an onshore flow. The volume of water (ΔV) that must pass through a vertical plane (at location x) parallel to the shore equals the total water volume increase of the area landward of location x. This increase of volume can been determined from the rise of the surface level assuming that it remains horizontal in every tidal phase. Then, the cross-shore current (u_c) that infills this volume in a time interval Δt is:

$$u_c(x,t) = \frac{\Delta V(x,t)}{\Delta t h(x,t)B} \quad (5.5)$$

where B is the unit along-shore width of the flat. The wave propagation processes on tidal flats were quantified using SWAN (Simulating WAves Nearshore), a spectral wave model (Booij et al., 1999). The wave model was forced at the seaward boundary by an incident wave field characterized by a JONSWAP spectrum (Hasselmann et al., 1973). Wind induced wave growth within the model domain was excluded. For model parameters related to wave propagation processes, default values have been used (see http://swanmodel.sourceforge.net/).

The bed shear stress induced by tidal currents is:

$$\tau_{cur} = \rho f_c u_c^2 \qquad (5.6)$$

where ρ and f_c are listed in the Table 5.1. The bed shear stress induced by waves is quantified as (Soulsby, 1995):

$$\tau_{wave} = 0.5 \rho f_w u_{wave}^2 \quad (5.7)$$

where u_{wave} is the root-mean-square value of the maximum orbital motion near the bed (this is part of SWAN output). f_w is a friction factor estimated as:

$$f_w = 1.39 \left(\frac{\xi}{k_s / 30} \right)^{-0.52} (5.8)$$

where k_s is the Nikuradse roughness length $2.5 * d_{50}$ and ξ is particle excursion amplitude close to the bed, which can be derived from SWAN model output. The mean bed shear stress under combined waves and currents during a wave cycle is calculated as (Soulsby, 1995):

$$\tau_m = \tau_{cur} \left[1 + 1.2 \left(\frac{\tau_{wave}}{\tau_{cur} + \tau_{wave}} \right)^{3.2} \right] \quad (5.9)$$

Thus, the maximum bed shear stress during a wave cycle is calculated as (Soulsby, 1995):

$$\tau_{max} = \left[(\tau_m + \tau_{wave} |\cos\theta|)^2 + (\tau_{wave} |\sin\theta|)^2 \right]^{0.5} \qquad (5.10)$$

where θ is the angle between current direction and direction of wave propagation. In our study, $\theta = 0$ as both currents and wave propagation are in cross-shore direction. To avoid potential errors related to overestimated bed shear stress in very shallow water, τ_{max} is quantified only when the water depth is larger than 0.1 m.

5.2.2 Field measurements of hydrodynamics and short-term bed-level changes
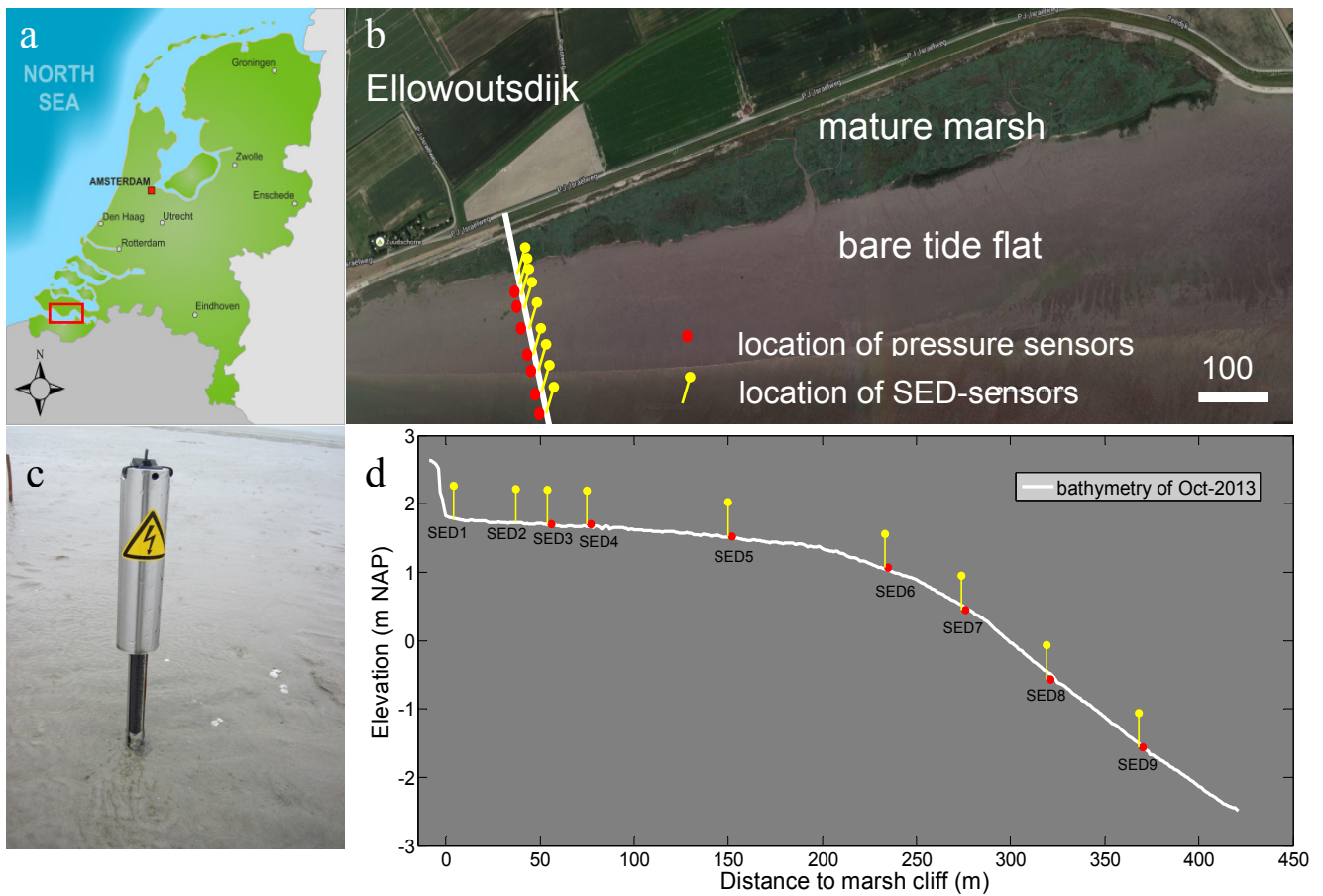
Figure 5.3 Location of the study site where short-term sediment dynamics and the corresponding hydrodynamics are measured. (a) is the location of our study site on a tidal flat in Westerschelde estuary, the Netherlands; (b) is the deployment of the SED-sensors for bed-level change measurements and the pressure sensors for wave measurements on a bare tide flat near Ellewoutsdijk; (c) is a photo of SED-sensor in field; (d) tidal flat cross-section and the instruments deployment, in which x= 0 is the location of a cliff between the mature marsh and the bare tidal flat.

To obtain field data for testing the DET-ESTMORF model performance in predicting short-term morphodynamics, we measured water levels, wave heights and short-term bed level changes along a tidal flat transect near Ellewoutsdijk in the Westerschelde Estuary, the Netherlands (Figure 5.3). The Westerschelde is a meso to macro-tidal estuary. At the monitored tidal flat, the mean tide range is 4.1 m and it is relatively exposed to wave action induced by prevailing south-westerly winds (Callaghan et al., 2010). As the tidal flat is about 25 km upstream of the open coast, the waves are mostly locally generated by prevailing southwesterly

winds. The yearly-averaged medium sediment grain diameter (d_{50}) at the study site is 85 μm. For this d_{50}, τ_{cr} is estimated to be 0.15 Pa, assuming that the proportion of clay is limited in the bed sediment (van Rijn, 2007). The field measurements were carried out almost continuously from 11 Oct, 2013 till 16 Jul, 2014. In this period, there were 6 field campaigns and each lasted about one month. Between two campaigns, there were gaps of a few days in between, when data was being retrieved from the field.

5.2.2.1 Water level and wave measurements

The water level and wave characteristics were measured by seven pressure sensors (OSSI-010-003C; Ocean Sensor Systems, Inc.). They are placed 0.05 m above the seabed. The measuring frequency is 5 Hz and the measuring interval is 15 minutes. The measuring period in an interval is 7 minutes, yielding 2100 data points. The mean water depth that occurs during an interval is determined as the averaged water depth recorded in these data points. Wave conditions were reconstructed from measured pressure fluctuations and the attenuation of the pressure signals with water depth was corrected following (Tucker and Pitt, 2001). Bulk wave parameters, e.g. significant wave height (H_s) and peak wave period (T_p), were derived from the reconstruction.

5.2.2.2 Bed-level change measurement

To provide data of short-term bed-level changes, we deployed automatic SED-sensors (Surface-Elevation Dynamic sensor) along the studied tidal flat transect (Figure 5.3c and 5.3d). The SED-sensor is a novel instrument developed at Royal Netherlands Institute for Sea Research (NIOZ), the Netherlands (see Chapter 4). When in use, it is inserted vertically into sediment bed. The electrical output of an array of 200 photovoltaic cells is used to determine the level up to which the array is covered by sediment. The distance between two cells is 2 mm, which is equal to the resolution at which bed levels and changes therein can be monitored. The length that the sensor is covered by sediment is noted as L_i, where the subscript 'i' indicates the number of tide with effective measurement. The accumulative bed-level change is then the difference between L_i and the initial belowground length (L_0). The day-to-day bed level change is then the difference between L_i and the previous effective measurement L_{i-1}. Erosion is assigned as negative values and sedimentation is assigned as positive values.

The SED-sensor does not work during nighttime or in turbid water due to the low light intensity. So the measuring window for the sensor is the emerged period during daytime. The lag

between two consecutive measurements can be more than one tidal cycle. For most cases, there was at least one measurement per day from each sensor (ca. daily resolution see Chapter 4). Additionally, the transect bathymetry has been measured using a manual DGPS leveling procedure at the beginning of the survey. This measurement has been used to facilitate model domain construction.

5.2.3 Model parameter setting and evaluations

Qualitative and quantitative tests of the DET-ESTMORF model were carried out with long-term and short-term morphodynamic modeling, respectively. The long-term modeling was compared with the previous process-based modeling results, whereas the short-term modeling was tested with the SED-sensor measurements.

5.2.3.1 Long-term morphological modeling

For the long-term morphological modeling, the initial tidal flat is linear for simplicity sake. The model domain extends 10 km in cross-shore direction and the grid size is 200 m. Water level fluctuations are schematized as:

$$\zeta(t) = \frac{R}{2}\cos(\frac{2\pi}{T}t) \quad (5.11)$$

where R and T are the tidal range and period, respectively. T was set as 12 hours and R was varied from 2 m to 8 m to explore its effect on tidal flat morphology. The incident significant wave height at the seaward boundary (H_{s_sea}) was varied from (0.2 m to 0.8 m) to test the effect of wave forcing on tidal flat morphology. In each tidal cycle, the τ_{90} is quantified every one hour.

The parameter settings for the long-term modeling are listed in Table 5.1. In particular, the inter-tidal diffusion coefficient D_{diff} should be proportional to $u^2 h / w_s$, in which u and h are the scales of flow velocity and water depth, respectively (Wang et al., 2007). In an ESTMORF modeling case study of the Westerschelde estuary, D_{diff} is 1250 m^2/s, with u = ~ 1 m/s, h = ~ 10 m and $w_s = 0.001$ m/s. In our long-term modeling, u = ~ 0.7 m/s, h = ~ 5 m and $w_s = 0.0005$ m/s. Hence, D_{diff} is estimated as 600 m^2/s for the long-term modeling.

For the long-term modeling, c_E was varied from 0.05 kg/m^3 to 0.3 kg/m^3 to test its influences on the tidal flat morphology. Correspondingly, τ_E varied in the range between 0.225 Pa and 0.6 Pa. At the seaward boundary of the model domain, the sediment concentration (c_k) is set to be c_E (Figure 5.2). At the landward boundary, the sediment transport flux is set to be zero, i.e. $c_1 = c_2$.

5.2.3.2 Short-term morphological modeling

For the short-term morphodynamic modeling, a modeling domain was built based on the bathymetry measured at the field measurement site, which was 371 m long in the cross-shore direction with 1 m resolution (Figure 5.3d). The modeling elevation range is from ca. -1.70 m NAP till ca. 1.8 m NAP, at the toe of the marsh cliff. The water level and the incident wave boundary condition used for morphological modeling were provided by most seaward pressure sensor near SED9. Combined force from wave and cross-shore tidal currents is taken in to account and it was quantified with a 15 minutes interval, which is the same interval for the wave measurement.

The short-term morphological modeling shared the same parameter settings as the long-term modeling listed in Table 1 with a few adaptions to the in-situ condition. One adaption is that the setting velocity of the suspended sediment (w_s) is determined based on the following equation [*van Rijn*, 1993]:

$$w_s = \frac{(s-1)gd_s^2}{18v} \quad (5.12)$$

where s is the ratio between sediment density to water density, equals to 2.65; v is the kinematic viscosity coefficient (Table 5.1); d_s is the suspended sediment grain size, which can be estimated based on bed sediment size measurement (d_{50} and d_{10}) as [*van Rijn*, 2007b]:

$$d_s = [1 + 0.0006(\frac{d_{50}}{d_{10}} - 1)(\psi - 550)]d_{50} \quad (5.13)$$

where the mobility parameter: $\psi = (u_{cw}^2)/[(s-1)gd_{50}]$ with $u_{cw}^2 = u_c^2 + u_w^2$. It is noted that equation (5.12) is only applicable when $\psi < 550$ and $d_{50} > 62$ μm (*van Rijn*, 2007b). Based on the hydrodynamic modeling of the study period, ψ is estimated to be 25 as the spatial-temporal mean 90th u_c and u_w is 0.06 m/s and 0.16 m/s, respectively. The mean d_{50} at the study site is

72 µm. As a result, d_s is estimated to be 20 µm and the setting velocity w_s is estimated to be 0.00036 m/s.

Another adaption is that D_{diff} should be adjusted to the reduced flow velocity (u_{cw}) and water depth. In the short-term modeling, a representative water depth can be given by the mean high water (i.e. the mean water depth for the location at 0 m NAP during the high water levels) at 2.2 m. A representative velocity scale can be provided by the sum of the spatial-temporal mean 90th u_c and u_w, which is 0.22 m/s. Hence, D_{diff} is estimated as 35 m^2/s based on the previous Westerschelde model (*Wang et al.,* 2007). However, the actual setting of D_{diff} is subjected to calibration.

For short-term modeling, the sediment concentration at the seaward boundary (c_k) is determined based on suspended sediment concentration measurement at a nearby regular monitoring location (Terneuzen), which is located at the other side of the estuary, opposing to our study site Ellowoutsdijk. At Terneuzen, water samples were taken on a monthly basis by a ship operated by Dutch Department of Public Works and Water Management (Rijkswaterstaat). This survey stops during storms and the corresponding sediment concentration is not known (*van Kessel et al.*, 2011). The mean sediment concentration (c_{mean}) is 0.058 kg/m^3 from Jan-2010 to Mar-2014, and this measurement after Mar-2014. As c_{mean} is a representative mean value that overlaps a part of the modeling period (Oct-2013 to July-2014), we assume that the overall equilibrium concentration (c_E) and the sediment concentration at the seaward boundary (c_k) equal to c_{mean} for the modeling period. Correspondingly, the uniform bed shear stress (τ_E) related to the conceptual equilibrium of the modeling tidal flat is estimated to be 0.14 [Pa] based on $c_E = c_{mean}$ and equation (5.1). The τ_E is kept constant for the entire modeling period (423 tidal cycles).

The landward boundary of the short-term model is located at the cliff between the saltmarsh and the bare tidal flat (near SED1 in Figure 5.3). Unlike the long-term model, the sediment transport flux cannot be set as zero at this boundary, as sediment can be transported from the bare tidal flat onto the saltmarsh (out of the model domain) during high tide. Because of the reduced hydrodynamic forcing, the sediment concentration at this boundary (c_l) is expected to be reduced compared to that at the seaward boundary. Hence, we assumed that at this

boundary $c_l = \alpha c_k$, where α is another calibration parameter to account for the reduced sediment concentration at the landward direction ($\alpha < 1$).

The high-frequency bed-level measurements in the periods: 11-Oct-2013 to 11-Nov-2013, 17-Jan-2014 to 04-Mar-2014 and 03-Apr-2014 to 06-May-2014 have been used for model calibration, whereas the measurements in the period: 20-Nov-2013 to 15-Jan-2014, 06-Mar-2014 to 31-Mar-2014 and 08-May-2014 to 12-Jun-2014 have been used for model validation. Prior to the morphological model evaluation, we first validated the wave modeling by comparing the modeled and measured significant wave heights (H_s) on the tidal flat transect.

All the modeling outputs (including hydrodynamic model validation, morphodynamic model calibration and validation) are evaluated by the root-mean-square deviation (*RMSD*), normalized root-mean-square deviation (*NRMSD*) and relative bias scores (*Rel.bias*).

$$RMSD = \sqrt{\frac{\sum(\Psi_{model} - \Psi_{obs})^2}{N}} \quad (5.14)$$

$$NRMSD = \frac{RMSD}{\left|\Psi_{obs\_max} - \Psi_{obs\_min}\right|} \times 100\% \quad (5.15)$$

$$\mathrm{Re}l.bias = \frac{\sum(\Psi_{model} - \Psi_{obs})}{\left|\sum(\Psi_{obs})\right|} \quad (5.16)$$

where Ψ_{obs} is the data from the observations and Ψ_{model} is the corresponding modeling quantify; Ψ_{obs_max} and Ψ_{obs_min} are the highest and lowest observations found in all the measuring stations; N is the total number of data points. *RMSD* and *NRMSD* give indications of the model correctness in an absolute and relative sense, respectively. The *Rel.bias* shows if there is any systematic defect in the model settings. For morphological model calibration, we tuned D_{diff} and α to obtain a minimum *RMSE* in accumulative bed-level changes compared to the observations. To test if the variation in D_{diff} has a significant impact on the model performance, a sensitivity analysis based on the evaluating *RMSD* and *Rel.bias* is conducted. D_{diff} is varied from 0.1 to 100 m^2/s in the sensitivity analysis.

5.3   Results

5.3.1 Long-term tidal flat morphological evolution modeling

To test the dynamic equilibrium concept embedded in the DET-ESTMORF model, long-term tidal flat morphodynamics modeling was carried out with various hydrodynamic and sediment supply conditions, which is compared qualitatively with previous process-based modeling studies.

5.3.1.1   Tidal flat evolution under contrasting forcing

The initial linear tidal flat profile was forced by tide only or combined tide-wave forcing in the long-term modeling (Figure 5.4). With the contrasting forcing conditions, the morphological response of the tidal flat is very different (Figure 5.4c and 5.4f). When the tidal flat is forced only by tide, the initial profile will firstly adjust its shape quickly to a steeper slope (from ca. $t_0 - t_2$) and then the profile can maintain such a slope and propagate seaward.

In contrast, when wave forcing is added, the tidal flat cannot continuously propagate seaward (Figure 5.4f). After an initial quick adjustment of the profile slope (from t_0–t_1), the profile seems to reach a quasi-static equilibrium around t_{10}. At this stage, the difference between two consecutive profiles is almost negligible. Notably, at t_{10}, the distribution of τ_{90} in combined wave and tide condition is almost uniform and equals to τ_E over the entire tidal flat (Figure 5.4d), which is different for the condition with only tide force and will be discussed in the following section.

Below the plateau, the tidal flat under pure tidal forcing generally has a convex shape. The tidal flats under combined tide and wave forcing has a distinctive concave shape. A "plateau" develops at the high water mark (elevation = 2 m) as the model only deals with the domain below the high water level.

Additionally, it is noted that the initial profile slope has no effect on the general evolution process or the stable profile bathymetry, but only influences the time span to reach a stable slope (data not shown).
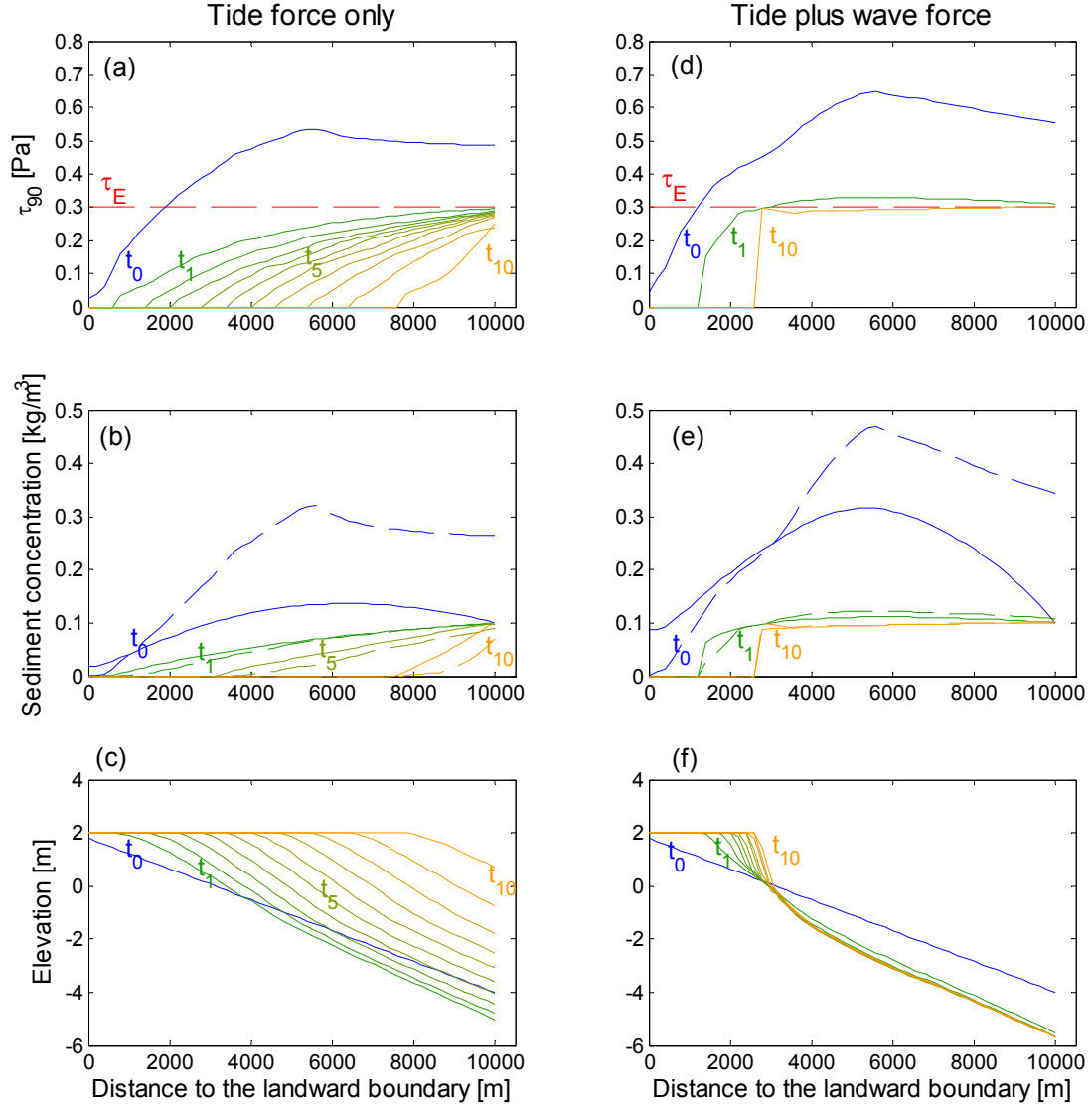
Figure 5.4 Long-term tidal flat evaluation under different hydrodynamic forcing; The model inputs are the overall equilibrium concentration (c_E) is 0.1 kg/m³, tidal range (R) is 4 m, incident signification wave height (H_{s_sea}) is 0.4 m. In each panel, t_0, t_1, … ,t_{10} indicate the time sequence of the evaluation, with t_0 being the initial conditions. Between two time steps, e.g. between t_0 and t_1 the time span is about 3,000 tidal cycles. The top two panels are the distribution of 90th percentile bed shear stress (τ_{90}) on tidal flats. The red dashed line indicates the uniform bed shear stress for equilibrium (τ_E) is 0.3 Pa, corresponding to the imposed c_E. The middle two panels are the distribution of the local equilibrium concentration (c_e, dashed line) and the actual concentration (c, solid line). The difference between these two determines the local bed-level changes. The tidal flat morphological evolution is shown in the two bottom panels. At the high water level mark (2 m), plateaus develop overtime as tidal flats propagate seaward.

The predicted contrasting profile evolution trajectories can be explained by the embedded dynamic equilibrium theory in the model. For the initial condition with pure tide forcing (t_0 in Figure 5.4a), τ_{90} is uniform and higher than the τ_E (0.3 Pa) on the lower part of the profile. On the upper tidal flat, it decreases gradually towards landward direction as the (tide-driven) passing water volume is reduced (ΔV in Equation (5.5)). A similar distribution of τ_{90} has been shown in previous studies (Le Hir et al., 2000; Pritchard et al., 2002). According to Equation (5.2), the spatial distribution of τ_{90} results in a similar distribution pattern of the local equilibrium concentration c_e (t_0 in Figure 5.4b). It shows that the lower tidal flat has the tendency of erosion (i.e. high c_e) and the upper tidal flat has the tendency of sedimentation (i.e. low c_e). The actual sediment concentration has a unimodal shape (c at t_0 in Figure 5.4b), which is derived by the sediment transport function (Equation (5.3)). The lower c at the upper and lower flat is induced by the subscribed boundary conditions. A high c at the middle flat is likely caused by sediment erosion over the lower part of the flat bed. Finally, the difference between c and c_e determines the bed level changes (Equation (5.4)): the deficits of c compare to c_e on the lower tidal flat leads to erosion whereas the surplus of c on the upper tidal flat leads to sedimentation (see t_0 in Figure 5.4b and 5.4c). Thus, the whole flat at t_1 becomes steeper than the original profile at t_0.

After the initial stage (since t_1 onwards), a positive feedback mechanism seems to govern the tidal flat development under pure tidal forcing. At t_1, τ_{90} drops below τ_E over the entire tidal flat because the tidal current velocity is reduced on the steeper tidal flat (i.e. increasing h in Equation (5.5)). Hence, the entire tidal flat has the tendency of sedimentation, which is also indicated by the low c_e over the tidal flat (see t_1 in Figure 5.4b). The derived actual sediment concentration field at t_1 is higher than the c_e in the area ca. x < 4000 m, which leads to sedimentation on the upper part of the tidal flat. The infilling of the upper profile further reduced the overall cross-shore current velocity because of the reduction of ΔV in Equation (5.5). It means the τ_{90} over the whole tidal flat will be further reduced (Figure 5.4a). Thus, the sedimentation on the profile continues and the positive loop is formed, which results in the seaward progressing profile ($t_1 - t_{10}$ in Figure 5.4c).

For the case with co-occurring wave forcing, the positive feedback does not occur and the tidal flat eventually approaches to a quasi-static equilibrium (Figure 5.4f). At t_0, τ_{90} is higher than that in a pure tide condition due to the addition wave force (Figure 5.4d), but the overall distribution pattern of τ_{90}, c_e and c is similar. As the profile moves seaward (t_1 - t_{10} in Figure 5.4f), the wave forcing becomes more competent in the shallow (upper) tidal flat to compensate the attenuated tidal current force (Figure 5.4d). At t_{10}, the τ_{90} becomes almost uniform and equals to the τ_E on the tidal flat. Correspondingly, the driver for morphological changes vanishes, i.e. the difference between c and c_e approaches to zero (t_{10} in Figure 5.4e). In such a condition, the tidal flat reaches a relatively stable equilibrium state (t_{10} in Figure 5.4f).

5.3.1.2   Tidal flat profile in various conditions

In order to test the long-term modeling performance comprehensively, we use the DET-ESTMORF model to predict tidal profile shape under various forcing and sediment supply conditions (Figure 5.5). In the previous section, it has been shown that a tidal flat under pure tidal forcing can continuously progress seaward with a constant slope (Figure 5.4c). A static equilibrium state is not possible in such a condition. Considering this, we compared profile shapes in different conditions when all of them have achieved stable slopes (e.g. t_5 in Figure 5.4c). The modeling outcomes can be compared qualitatively with previous studies.

It is clear that a tidal flat profile becomes steeper with an increase of tidal range (Figure 5.5a). The increase in steepness can be explained by the insights gained from Figure 5.4a and 5.4c. The larger tidal range will lead to larger passing volume (ΔV) in Equation (5.5), which means a higher current velocity and a higher τ on the lower tidal flat. Then, stronger erosion can occur on the lower flat to make the whole profile steeper compared to the cases with smaller tidal ranges. For the cases with larger tidal range, the same initial profile takes longer to reach a stable slope, as there is more sediment to be eroded at the beginning of the simulation.

The width of the tidal flat, i.e. the distance from high water to low water, increases as the tidal flats propagate seawards. As the profiles with larger tidal ranges takes more time to reach stable slopes, they have smaller width within the same time span. However, the width difference may be not important as all the profile width increases over time in this condition and the actual width may depend on the considered time-scale.
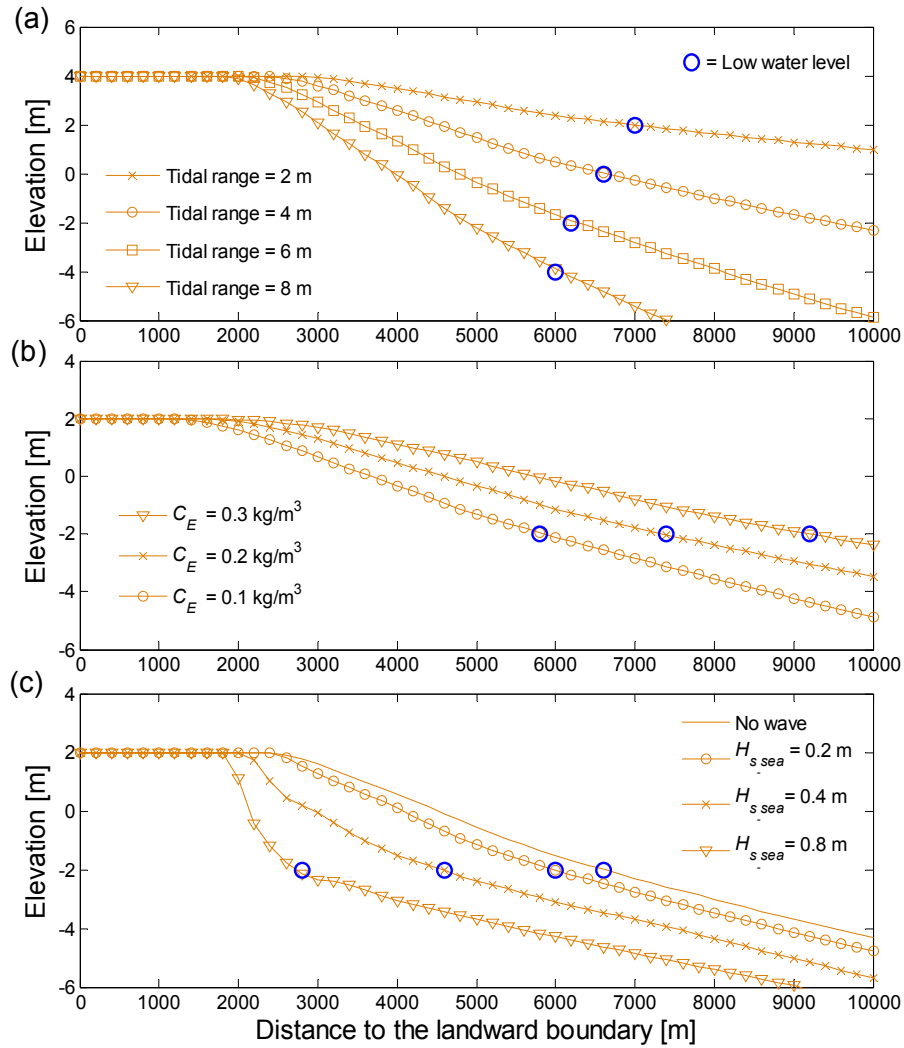
Figure 5.5 Predicted tidal flat profiles with different conditions. (a) tide only condition, the overall equilibrium concentration (c_E) is 0.1 kg/m³, correspondingly the uniform bed shear stress for equilibrium (τ_E) is 0.3 Pa. The tidal range (R) varies from 2 to 8 m. The 4 profiles are moved vertically to make the high water level coincident. The shown profiles are from 10000 tidal cycles, when relative constant profile slopes have been reached; (b) tide only condition, R is 4 m. C_E is 0.1, 0.2 and 0.3 kg/m³, accordingly τ_E is 0.3, 0.45 and 0.6 Pa. The shown profiles are from 5000 tidal cycles, when relative constant profile slopes have been reached; (c) tide plus wave, R is 4 m, C_E is 0.1 kg/m³, τ_E is 0.3 Pa, wave height from the seaward boundary (H_{s_sea}) is 0, 0.2, 0.4, 0.8 m. The shown profiles are from 10000 tidal cycles, when the profile with 0.8 m incident wave has reached a quasi-stable equilibrium and other profiles are still migrating seaward.

The modeling results also show that if the sediment supply is increased in the system, tidal flat width increases and profile steepness reduces accordingly (Figure 5.5b). Furthermore, a rise in H_{s_sea} leads to more concave profiles with smaller profiles width (Figure 5.5c). It is worth noticing that under combined tide and wave forcing, the lateral position of the relative stable equilibrium profile may depend on the relative strength of wave forcing compared to the tidal forcing. If wave forcing is stronger than tidal forcing (high H_{s_sea} conditions), tidal flats can reach a relative stable equilibrium profile in a shorter time-span and can stay closer to the landward boundary. For the case with weaker wave forcing (low H_{s_sea} conditions), the profile will keep migrating seaward until the wave forcing becomes significant in the shallow areas to enable a uniform distribution of τ_{90}. For instance, the profile with 0.8 m H_{s_sea} approaches to a stable equilibrium after about 10,000 tidal cycles (Figure 5.5c), whereas other profiles with 0.4 m H_{s_sea} will keep propagating seaward after the same time span and will reach a stable equilibrium after about 30,000 tidal cycles (see t_{10} in Figure 5.4f).

5.3.2 Short-term bed-level dynamics modeling

To test the DET-ESTMORF model in a quantitative way, we compared the modeling results with the hydrodynamic and morphodynamic measurement at the study site in the Westerschelde Estuary. This modeling exercise also demonstrates how this dynamic equilibrium theory can be applied for realistic morphological predictions.
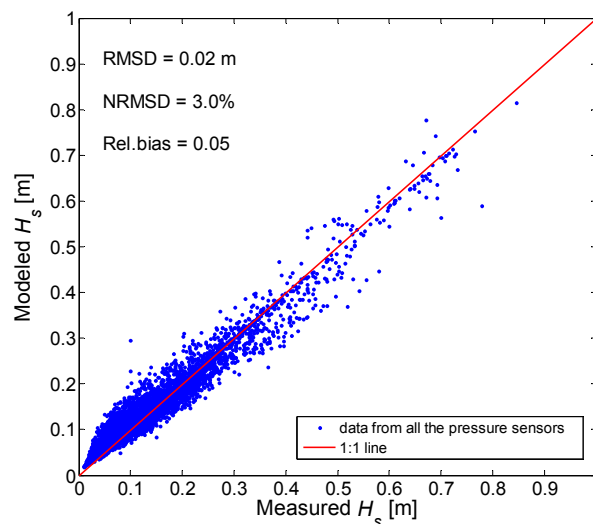
Figure 5.6 Comparison of modeled and measured significant wave height (H_s) on the studied tidal flat. The wave measurements are obtained by an array of press sensors shown in Figure 5.3. The shown data is from the measuring period: 11-Oct-2013 to 11-Nov-2013 and the measuring interval is 15 minutes. The total number of data points is 6418 in this period, which includes a severe storm event with maximum significant wave height being 0.8 m on this shallow tidal flat.

5.3.2.1 Hydrodynamic modeling at the study site

The wave modeling part was evaluated firstly. The modeled significant wave height was compared against the measured significant wave height along the monitoring transect (Figure 5.3). The comparison shows that the predicted H_s agrees well with the wave measurement (Figure 5.6), which indicates it is reliable to use SWAN model for wave simulations at the study site.
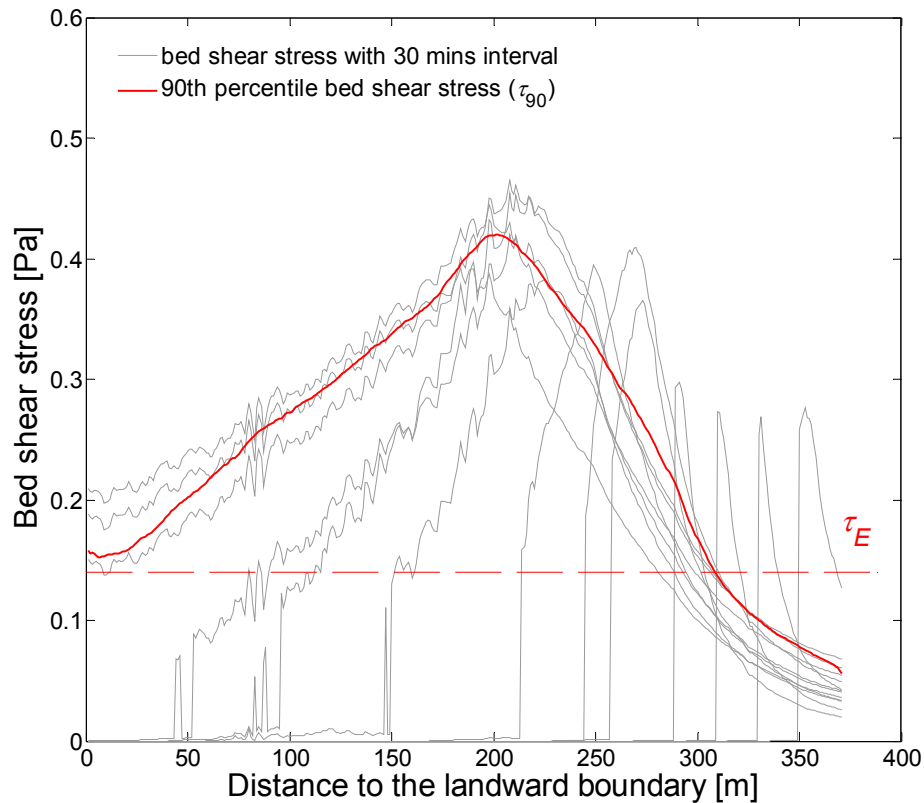
Figure 5.7 A demonstration of bed shear stress in a tidal cycle and the corresponding 90th percentile bed shear stress (τ_{90}) for morphodynamic modeling at the study site; the estimated uniform bed shear stress for equilibrium (τ_E) is 0.14 Pa, which is plotted as the horizontal dashed line. In this tidal cycle, the incident significant wave height (H_{s_sea}) varies from 0.08 m to 0.43 m, with the tide-averaged H_{s_sea} being 0.26 m bed shear stress is quantified every 15 minutes in the model and plotted here every 30 minutes for demonstration.

For the short-term morphology modeling, bed shear stress is quantified every 15 minutes to count for the changing hydrodynamic forcing conditions. Within a tidal cycle, the bed shear stress distribution varies in time with the incident wave conditions and the tidal phase (Figure

5.7). For each time step shown in the Figure 5.7, the bed shear stress distribution generally has a unimodal shape, which is likely induced by wave breaking process that occurs in this tidal cycle with relatively large incoming wave height. The location of the peak bed shear stress moves laterally on the tidal flat with the varying tidal phase. Based on the bed shear stress time series at each location, the τ_{90} is derived as an input for the morphological prediction following (Friedrichs, 2011) (Figure 5.7).

5.3.2.2 Short-term bed-level changes modeling and measurements

Quantitative evaluation of the morphological model is carried out by calibrating and validating the DET-ESTMORF model with the SED-sensors measurements. D_{diff} and α are calibrated to be 30 (m^2/s) and 0.1 (-) respectively, as this setting leads to the minimum *RMSD* (2.19 cm) in the calibration. Subsequently, these settings were applied to both calibration and validation of the morphodynamic modeling.
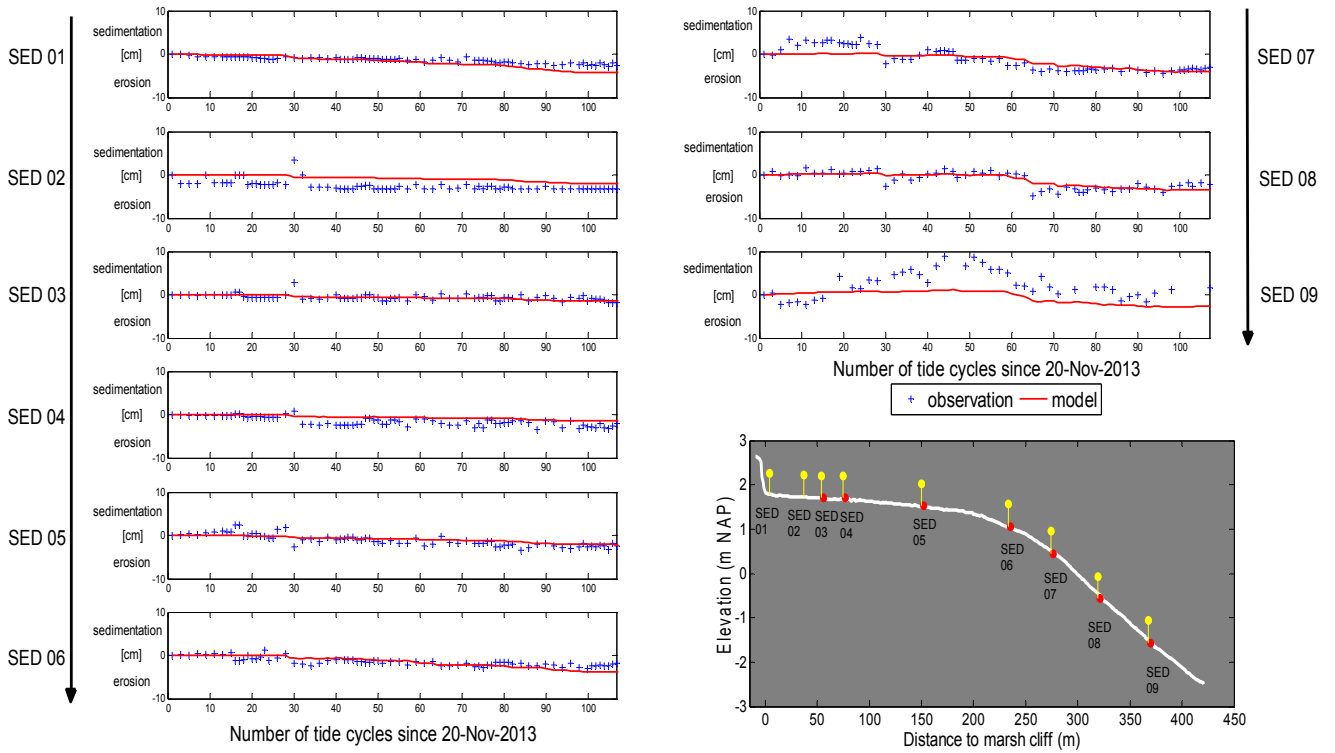
Figure 5.8 Modeled and measured accumulative short-term bed-level changes, which is the bed-level changes of each period compare to the initial bed-level. Positive values mean sedimentation and negative values mean erosion. The demonstrated data is from the period 20-Nov-2013 to 15-Jan-2014. The total number of observation points during this period is 627.

An example of the modeled accumulative bed-level changes and the corresponding SED-sensor data is shown in Figure 5.8. The accumulative bed-level changes give an overview of the short-term morphological evaluation in a model validation period: 20-Nov-2013 to 14-Jan-2014. Overall, the predicted bed-level changes fit reasonably well with the observed erosion trends at each station (Figure 5.8). On the upper tidal flat (i.e. station SED1, SED3 to SED6), the model prediction agrees well with the measurements. At station SED2, however, the model does not capture the bed-level change occurred between the first and second measurements and such an error retains during the rest of the modeling period. At lower stations SED7 and SED8, the agreement between model prediction and measurement is still reasonably good. Specially, the prediction captured a storm event during tidal cycle 64 (tidal-averaged $H_{s\_sea} > 0.55$ m) at these two stations. Although the erosion during this storm seems underestimated, the morphodynamic trend is reproduced well by the model. The model cannot reproduce the high degree of morphodynamics at the most seaward station (SED9). It is likely that long-shore currents may play an important role in this relatively deep area but it is not accounted for in our 1D model.

An overview of the model calibration and validation using all the SED-sensor measurements shows that the model performance is good (Table 5.2). The evaluation is conducted based on both accumulative and daily bed-level changes. For the evaluation based on accumulative bed-level changes, the mean *RMSE* value of the three calibration period is 2.25 (cm), whereas the mean *RMSE* value of the validation periods is 1.58 (cm). The smaller mean *RMSE* value in the validation periods indicates a reasonable predictive capability of the model. The mean *NRMSD* of the accumulative bed-level changes in calibration and validation periods is 28% and 20%, which implies that the modelling errors is relatively small compare to the observed overall morphodynamic activities.

For the evaluation based on daily bed-level change, the *RMSD* and the *NRMSD* are generally smaller than those based on the accumulative bed level change. It is because this assessment is based on the changes over two consecutive measurements, and the possible influence of the errors modeled in previous periods is excluded (e.g. the second data point at SED2 in Figure 5.8). In this assessment, *Rel.bias* values are closer to zero compared to those with accumulative bed-level changes, which indicates a weaker bias favoring sedimentation (Table 5.2).

Table 5.2 Model calibration and validation against the SED-sensor measurements [a]

Bed-level measurement periods	Data usage	Total number of observations	RMSE (cm)	NRMSE (%)	Rel.bias (-)
11-Oct-2013 to 11-Nov-2013	calibration	292	3.00 (1.02)	36% (19%)	0.70 (0.13)
20-Nov-2013 to 15-Jan-2014	validation	627	1.49 (0.90)	10% (15%)	-0.04 (-0.04)
17-Jan-2014 to 04-Mar-2014	calibration	508	1.61 (0.91)	20% (19%)	-0.49 (-0.01)
06-Mar-2014 to 31-Mar-2014	validation	291	1.56 (1.03)	31% (22%)	084 (0.08)
03-Apr-2014 to 06-May-2014	calibration	280	2.13 (1.22)	27% (20%)	0.57 (-0.01)
08-May-2014 to 12-Jun-2014	validation	235	1.70 (0.91)	20% (20%)	0.08 (-0.02)

[a] The data without brackets is based on the accumulative bed-level changes, which is the difference between the current bed-level and the initial bed-level; the data in brackets is based on the daily bed-level changes, which is the difference between the current bed-level and the bed-level of the previous day(s). All the data is averaged in space based on the SED-sensor stations (see Figure 5.3).

Sensitivity analysis is conducted by evaluating the model performances with varying D_{diff} (Figure 5.9.). The measured accumulative bed-level changes are used in the model evaluation. In the modeling performance test with calibration data, $RMSD$ reaches to its minimum (2.19 cm) when D_{diff} is 30 m^2/s. In this test, as D_{diff} varies from 0.1 to 100 m^2/s, the corresponding $RMSD$ only increased 14% to about 0% compared to the minimum value. In the test with both calibration and validation data, the $RMSD$ values are smaller compare to that with calibration data. The minimum $RMSD$ (1.87 cm) in this test is reached when D_{diff} is 10 m^2/s. As D_{diff} varies from 0.1 to 100 m^2/s, the $RMSD$ only increased 17% to 1% compared to the minimum value. When D_{diff} is higher than 1 m^2/s, the $RMSD$ is fairly constant around 1.90 cm. Therefore, in the test with only calibration data and the test with all the data, the model performance is not significantly influenced by D_{diff} in terms of $RMSD$.
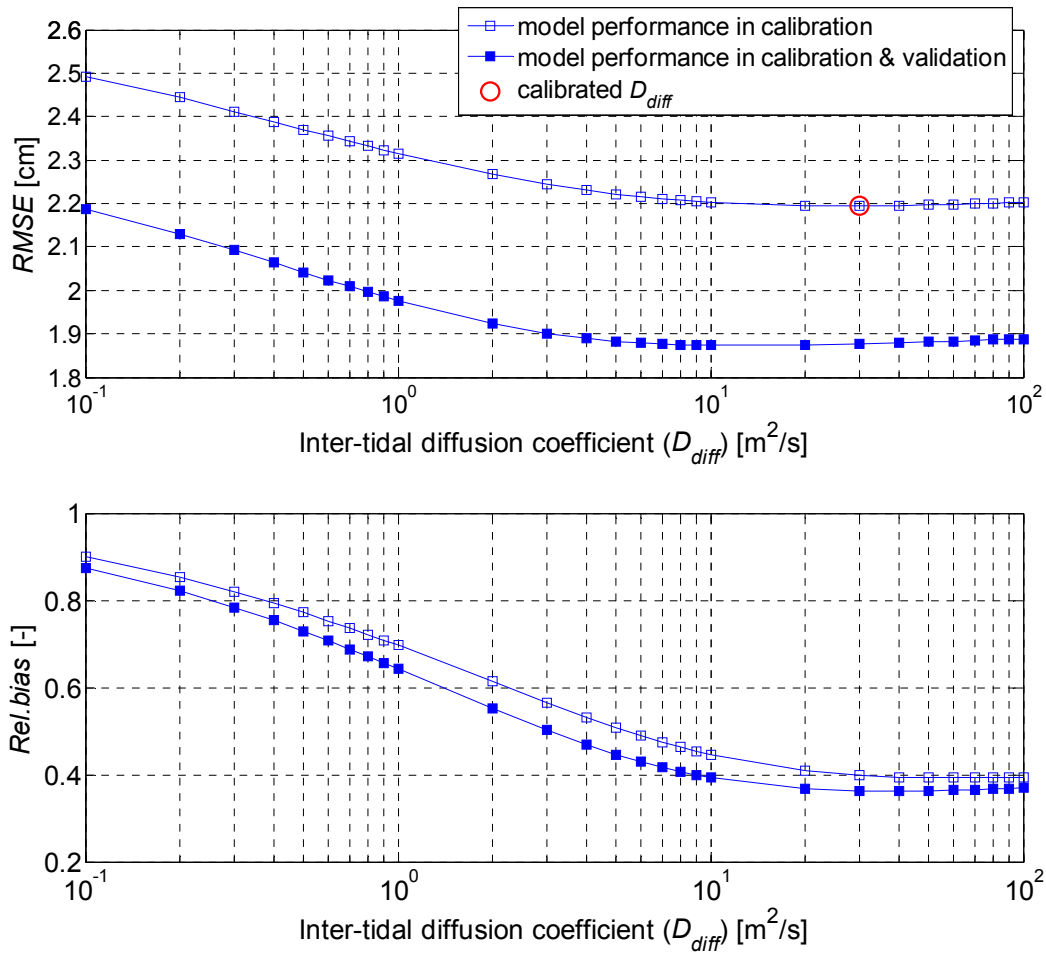
Figure 5.9 Sensitivity analysis of the modeling performance related to inter-tidal diffusion co-efficient (D_{diff}). The performance is evalued by root-mean-square deviation (*RMSD*) and relative bias scores (*Rel.bias*), which are based on accumulative short-term bed-level changes. The 'model performance in calibration' is based on comparing the modeled and measured data that used for calibration (see Table 2.), and the 'model performance in calibration & validation' is based on the entire data set. D_{diff} is calibrated as 30 m^2/s, as it leads to the least RMSD during the calibration.

It is also noted that in the test with calibration data, the *Rel.bias* drops from ca. 0.9 to 0.4 as D_{diff} increases from 0.1 to 100 m^2/s. The test with both calibration and validation data shows a similar trend, but the *Rel.bias* values are closer to zero. The *Rel.bias* reduction with the increasing D_{diff} means that the degree of overestimating sedimentation (underestimating erosion) reduces. It may be caused by the fact that with larger D_{diff} more (wave) eroded sediment can be transported elsewhere and less sediment will stay around the original location waiting

to settle onto the seabed again. When D_{diff} >10 m^2/s, the *Rel.bias* stays relatively constant at 0.4 in both tests. Thus, the model performance (in term of *Rel.bias*) is not significantly influenced in this range of D_{diff} , and the model has a constant tendency favoring sedimentation or underestimating erosion. The reason of this constant tendency is discussed in the following section.

5.4 Discussion

5.4.1 Testing dynamic equilibrium theory in long-term morphological modeling

In this study, we implemented the dynamic equilibrium theory in the DET-ESTMORF model. The long-term DET-ESTMORF modeling outcome can be compared with previous process-based modeling results that were summarized in (Friedrichs, 2011). As the process-based modeling does not rely on the dynamic equilibrium theory for morphodynamic modeling, the comparison between these two types of model is an independent and direct test of the theory. The long-term morphological predictions agree well with the previous process-based modeling, which implies the validity of the dynamic equilibrium theory.

In the long-term modeling, the model predicts the profile to attain a convex or concave shape when it is forced by pure tide or combined tide and wave actions (Figure 5.4 and 5.5), which agrees with the previous process-based models and the field observations summarized in (*Friedrichs,* 2011). We also show that predicted tidal flat bathymetry varies in a similar way as the previous process-based models when tidal range, incident wave height and offshore sediment supply are changed (Liu et al., 2011; Pritchard et al., 2002; Roberts et al., 2000).

Furthermore, the predicted dynamic behavior of the tidal flat also agrees with the previous studies that are summarized in (Friedrichs, 2011). For the case with only tide force, the predicted seaward migrating tidal flat (see Figure 5.4c) agrees with previous process-based modeling studies and observations from Jiangsu coast for instance (Liu et al., 2011; Pritchard et al., 2002; Waeles et al., 2004). This continuous propagating behavior is induced by a positive feedback process that is the governed by the dynamic equilibrium theory embedded in the DET- ESTMORF model (Figure 5.4a and 5.4b). In previous process-based models, the same profile morphological behavior was explained by nonzero tidal-averaged settling lag that favors a small but persistent net sediment import (Pritchard et al., 2002). The different explana-

tions offered by these two different types of models may seem misleading for the morphodynamic interpretation. However, it should be noted that the dynamic equilibrium theory is meant to describe the tidal flat overall morphological behaviors rather than elaborating the detailed processes like the process-based models. Hence, based on this theory, the DET-ESTMORF model may offer alternative explanations for the same morphological behavior.

Additionally, the model prediction also shows that only when wave forcing is included, the tidal flat may reach a relative stable equilibrium profile (Figure 5.4f), which agrees with the previous process-based modeling studies as well (Waeles et al., 2004; Maan et al., sumbitted). This can be explained by the embedded dynamic equilibrium theory as: the wave force is needed to compensate the damped tidal current force in the shallow areas to minimize the spatial gradients in bed shear stress and eventually achieve a relative static equilibrium. The model further shows that tidal flat concavity increases with the incident wave forcing, which is also in line with the previous modeling (Roberts et al., 2000) and field studies (Friedrichs, 2011).

5.4.2 Testing dynamic equilibrium theory in short-term morphological modeling

Morphological modeling studies often focus on a timescale of years to decades in order to project long-term tidal flat developments with possible influence of sea level rise and/or sediment supply changes (Fagherazzi et al., 2012, 2006; Kirwan et al., 2010; Mariotti and Fagherazzi, 2010; Pritchard and Hogg, 2003; Roberts et al., 2000). However, a long-term concurrent data set including tidal flat bathymetry, offshore sediment concentration and weather conditions (stormy/calm periods) is rare for quantitative model evaluation (Pritchard and Hogg, 2003). In this study, we adjust the DET-ESTMORF model to quantify the short-term bed-level changes so that the high-frequency wave and SED-sensor measurement can be used for quantitative model evaluation.

Moreover, the short-term morphodynamic modeling serves as a demonstration of applying the dynamic equilibrium theory for realistic applications. Recent studies have shown that predicting short-term bed-level fluctuations can be important for the understanding of vegetation establishing patterns on bare tidal flats (Balke et al., 2011, 2013, 2014; Han et al., 2012). Thus, this DET-ESTMORF model can be a relevant tool for vegetation colonization prediction. In contrast, the original analytical model (Friedrichs and Aubrey, 1996) can only provide

the idealized profile bathymetry when a static equilibrium has been achieved. Such a model is helpful in understanding the typical large-scale tidal flat behaviors, but may be less useful for realistic morphological predictions.

Overall, the model prediction fits reasonably well with the bed-level measurement regarding to the *RMSE* and *NRMSE* evaluation (Table 5.2). During some storm events, the prediction clearly follows the sudden daily changes (SED7 in Figure 5.8). The results imply the dynamic equilibrium theory can be trustworthy and useful in explaining the morphodynamics in a daily to monthly timescale. However, it is also noted that the predictions show a bias towards sedimentation and the bed-level changes at the most seaward SED-sensor station cannot be reproduced well by the model. It may be caused by the fact that only a few essential physical processes are included in the DET-ESTMORF model, which may limit the prediction accuracy and will be discussed in the section 4.4.

The ESTMORF-type models quantify the morphological changes over an entire tidal cycle, so that the inter-tidal diffusion coefficient (D_{diff}) is employed to account for the overall sediment mixing due to both tidal and wave motion in a tidal cycle. The D_{diff} used in a modeling is calibrated to be 30 m^2/s, and it is estimated to be 35 m^2/s following Wang et al., (2007). The two values are fairly close, suggesting the usefulness of the parameter setting guidelines in Wang et al., (2007). The sensitivity analysis further shows that the model performance is not sufficiently influenced by D_{diff} if it is in the range between 10 to 100 m^2/s. However, it is also noted that the predictions show a bias towards sedimentation (Figure 5.9). It may be caused by the fact that some of the erosion events cannot be represented accurately in the model, and these errors remain in the following analysis of the accumulative bed-level changes (e.g. SED2 in Figure 5.8). It is also noticed that the short-term morphological changes at the deepest SED-sensor station cannot be reproduced very well (i.e. SED9 in Figure 5.8). It may be because that long-shore currents play an important role in this relatively deep area, which is not accounted for in our 1D model.

5.4.3 Defining uniform bed shear stress τ_E

Defining τ_E is of fundamental importance in the dynamic equilibrium theory as it describes the tidal flat equilibrium state. The dynamic equilibrium of a tidal flat is associated with its local hydrodynamic forcing, sediment supply and other factors (Friedrichs, 2011). Similarly,

the long-term averaged suspended sediment concentration on the tidal flat is also affected by these factors. Hence, we define τ_E as the bed shear stress that can maintain a constant overall equilibrium concentration (c_E) in water column (Equation (5.1)). Effectively, τ_E depends on c_E in the DET-ESTMORF model.

We find this definition of τ_E fits well with the dynamic equilibrium theory and previous findings: 1) the dependency of τ_E on c_E has also been suggested by previous process-based modeling. For instance, (Liu et al., 2011; Pritchard et al., 2002) have shown that on the tidal flats with higher sediment input (higher c_E), τ_E is stronger when a constant profile slope has been reached. Hence, in process-based models, τ_E on the eventual tidal flats may be determined by c_E via long-term morphodynamic feedbacks; 2) in realistic case studies (reference herein), c_E can be determined as the long-term background sediment concentration in the study areas, which generally accounts for the combined effect of the local forcing and sediment supply conditions. If the sediment supply in an area is increased by natural or anthropogenic processes (higher c_E), τ_E will increase accordingly, i.e. move τ_E to a higher level in Figure 5.2a. Thus, the entire system would shift towards the direction favoring deposition. In contrast, if the sediment supply reduces, the whole system will become favoring erosion instead. Similar tidal flat morphological response has been reported in previous studies (Friedrichs, 2011).

5.4.4 Strengths and limitations of the DET-ESTMORF model

Judging from the modeling philosophy, the DET-ESTMORF model clearly adapts a top-down approach (Roelvink and Reniers, 2011; Stive and Wang, 2003). That is the model starts with describing the top feature of tidal flat morphology then move downwards to attend more detailed aspects such as hydrodynamics and sediment conservation. The process-based models (e.g. Delft3D), on the other hand, generally adapt a bottom-up approach. They start with a meticulous elaboration of the relevant physical processes, and then reveal the morphological features.

For all models, the critical question is about understanding and depicting the governing processes and the underlying theories. Depending on the nature of the processes and theories, we may choose a suitable modeling approach to implement such an understanding. In many cas-

es, process-based models are powerful tools to provide insights and predictions of tidal flat morphology (Lesser et al., 2004). Yet, for the primary purpose of the present study, i.e. directly testing the dynamic equilibrium theory, they may have difficulty in satisfying the underlying assumption of the theory, as a uniform bed shear stress distribution rarely exists.

The main strengths of the DET-ESTMORF model can be summarized as: 1) the need of a prescribed equilibrium state in this model gives us a handle to implement and directly test the dynamic equilibrium theory by evaluating the model performance; 2) compared to the original analytical solution (Friedrichs and Aubrey, 1996) that only deals with the idealized uniform forcing condition, the DET-ESTMORF model applies the dynamic equilibrium theory in realistic morphological predictions with spatially and temporally varying bed shear stress, which largely broadens the model application range; 3) for long-term morphological modeling, DET-ESTMORF prediction can always converge to a morphological equilibrium close to reality because of the underlying dynamic equilibrium theory. However, minor errors in process-based models over each tidal cycle may accumulate over time and lead to unrealistic predictions in long-term; 4) for short-term morphodynamic modeling, the DET-ESTMORF model provides a simple but sufficient tool to predict frequent tidal flat bed-level changes that affect critical ecological processes such as vegetation establishment.

In order to test dynamic equilibrium theory, the DET-ESTMORF model only involves the necessary processes for morphological simulations. However, the simple configuration of the model also leads to some limitations. One of the main limitations is that alongshore currents were not considered in the current 1D model, which can be important for the tidal flat morphodynamic activities at the lower elevations (e.g. the station SED9 in Figure 5.8) (Gong et al., 2012). For the sake of simplicity, we neglect the possible influence of multiple sediment fractions, sediment settling lags and potential biogeomorphological interactions on tidal flat morphology. Additionally, model calibration is always needed when applying this model to a new area, since parameters like D_{diff} cannot be derived from measurements directly (Wang et al., 2007). For more precise morphological prediction, more physical processes can be included, such as alongshore currents, mixed sediment type, biostabilisation /bioturbation and etc.

5.5   Conclusion

In this study, we implemented the dynamic equilibrium theory into the hybrid DET-ESTMORF model. Applying this model, we showed that the dynamic equilibrium theory

could be applied for both long-term and short-term morphodynamic predictions with spatio-temporally varying bed shear stress. The long-term modeling not only derives the classic convex or concave profile shape with corresponding force conditions but also presents similar dynamic profile behavior as that found in previous process-based modeling studies. Furthermore, the short-term modeling also showed a reasonable good agreement with the field bed-level change measurements obtained by the SED-sensors. The good model performance of the long-term and short-term modeling test indicates that the embedded dynamic equilibrium theory is valid and the model itself is useful in morphological predictions. It is noted that the current DET-ESTMORF model only considers a limited number of physical processes, which may cause deviations between the morphological observation and prediction. However, the simple model structure may provide an open platform to incorporate relevant biotic and abiotic processes for further understanding of tidal flat landscape evolution.

Chapter 6

Synthesis

6.1 General discussion

The main objectives of this thesis are to increase the understanding of the hydrodynamic processes and their role in the intertidal morphodynamics and ecosystem establishment. To this end, hydrodynamics in vegetated and non-vegetated intertidal areas and its impacts are investigated by various approaches including flume experiments, field measurements and numerical modeling.

The hydrodynamic and morphological processes in intertidal areas are closely related to biogeomorphic feedback mechanisms due to the widespread fauna and flora. The topics included in this thesis address a part of the saltmarsh biogeomorphic feedback rather than cover the full loop of it. In this thesis, Chapter 2 focuses on the wave dissipation in vegetation canopies, which is related to the saltmarshes ecosystem engineering capability (Jones et al., 1994). Chapter 3 illustrates the control of hydrodynamic forcing on marsh establishment in bare areas. This controlling mechanism is prior to the positive biogeomorphic feedbacks related to marsh presence, which only starts after a critical minimum biomass is surpassed (Bouma et al., 2009b). Chapter 5 illustrates the feedback between hydrodynamic forcing and morphodynamics, whereas the effect of biota is not considered. It is noted that the model proposed in Chapter 5 contains only the basic elements for morphological prediction. This model may serve as a platform to incorporate additional biogeomorphic feedback processes. Finally, Chapter 4 introduces a method to accurately monitor the consequences of biogeomorphic feedbacks: sediment surface-elevation changes. These measurements were also essential for the validation of the modeling in chapter 5.

There is an increasing number of numerical models aiming to describe the saltmarsh biogeomorphic evolutions (Temmerman et al., 2007; Fagherazzi et al., 2012a; Schwarz et al., 2014).

Although some progress has been made in recent studies, the biogeomorphic interactions are complex in nature and our knowledge on the feedback mechanisms is still limited. Linking the relevant physical and biology processes remains challenging. Many parts in the feedback loop are currently understudied. This thesis sheds lights on some of the key processes in the salt-marsh related biogeomorphic interactions, which may increase the general understanding of intertidal landscape and our competence to predict its evolutions.

6.2 Conclusions

From both a scientific and management point of view, the most important findings in this thesis are:

1. Wave dissipation capacity of a vegetation canopy is influenced by co-occurring tidal currents. Whether the capacity is increased or decreased depends on the ratio between current velocity and the amplitude of horizontal orbital velocity (α). When α is small, the capacity is decreased compare to pure wave conditions due to the variations in drag coefficient and in-canopy velocity. When α is large, the wave dissipation capacity can be increased due to current-wave interaction. (Chapter 2)

2. Applying vegetated wetlands for coastal protection should take into account the possible negative effect of tidal currents on vegetation wave damping capacity. Flooding tide during storm events (wave and current in a same direction) could be a critical scenario for coastal protection designs that integrates the vegetated habitats. (Chapter 2)

3. To derive the vegetation drag coefficient, the direct force measurement approach is possibly more accurate than the calibration approach and perhaps the only approach for current-wave combined conditions. (Chapter 2)

4. The 'Window of Opportunity' concept provides a framework to explain and predict vegetation establishment patterns. Incorporating hydrodynamic forcing assessments in such a framework can substantially increase the prediction accuracy in space and in time. (Chapter 3)

5. Tidal flat morphology affects the marsh vegetation establishment extent via hydrodynamic forcing distribution. Due to the difference in dissipating wave forcing, con-

vex profiles with gentle slopes can host saltmarshes in a wider elevation range and larger area compared to that on concave steep profiles. Thus, affecting the tidal flat morphology can open up new windows of opportunity to restore and manage salt-marsh ecosystems. (Chapter 3)

6. The novel stand-alone SED-sensor provides a high-resolution automatic method to monitor frequent bed-level dynamics in intertidal environments. (Chapter 4)

7. Observed contrasting short-term (daily) bed-level changes at different sites can be explained by the local hydrodynamic forcing characteristics (wave vs. tidal current). (Chapter 4)

8. The tidal flat dynamic equilibrium theory proposed by Friedrichs (2011) has been operationalized by the incorporated elaborately in the DET-ESTMORF model. Good model performance indicates the validity of this theory in realistic conditions with spatiotemporally varying hydrodynamic forcing. (Chapter 5)

9. In the dynamic equilibrium theory (Friedrichs, 2011), the uniform bed shear stress associated with tidal flat morphological equilibrium can be defined as the shear stress that maintains a constant background sediment concentration in the water column. For a realistic case study, this background concentration can be estimated as the long-term sediment concentration in the study area, which inherently accounts for the effects of the local hydrodynamic forcing and sediment supply conditions on the tidal flat equilibrium. (Chapter 5)

10. The DET-ESTMORF model can be a useful tool for long-term and short-term mor-phodynamic predictions. It may also serve as a platform, to incorporate additional physical and biology processes. (Chapter 5)

6.3   Recommendations

Based on the studies in this thesis, recommendations for further research are summarized as follows:

1. It is important to gather field data of wave dissipation by vegetation in combined cur-rent-wave flows, in such way that the ratio between tidal current velocity and wave orbital velocity is expected to vary greatly. Additionally, it can be interesting to in-

vestigate the conditions with tidal currents flowing in the following and opposing direction (flooding vs. ebbing) relative to the wave propagation.

2. It is recommended to carry out more detailed velocity and drag force measurements in vegetation canopy with sufficient spatial and temporal resolutions. For the cases with flexible vegetation, it is desirable if the stem motion can be registered in a suitable way.

3. Seedlings tolerance to the physical disturbances induced by direct flow drag and bed sediment suspension requires further studies. Specially, it is important to learn the variation of this tolerance with seedling age, species, and abiotic factors that affect growth such as e.g. temperature, salinity and sediment type.

4. It is recommended to increase the frequency of vegetation cover survey at contrasting sites to further test the 'Window of Opportunity' concept.

5. It is preferable to incorporate a self-lighting system to the SED-sensors that allow for underwater measurements as well as measurements during the night, for non-interrupt bed-level monitoring.

6. The SED-sensors are expected to be applicable in a number of geomorphological environments (e.g. tidal flats, beaches, rivers and dunes). It is recommended to use SED-sensors for sediment surface monitoring in various environments to test their applicability.

7. The DET-ESTMORF model would benefit from more case studies to further evaluate the model skills and to create an application routine. Spatially, it is recommended to carry out long-term suspended sediment concentration measurements in the interested areas together with morphological change monitoring in order to check if the theoretical uniform bed shear stress can be adequately defined as the force that maintains a constant sediment concentration.

8. It is recommended to include more ecological and physical processes in the DET-ESTMORF model to explore the relevance of the dynamic equilibrium theory in bio-geomorphic landscapes.

References

Amoudry, L.O., Souza, A.J., 2011. Deterministic coastal morphological and sediment transport modeling: A review and discussion. Rev. Geophys. 49. doi:10.1029/2010RG000341

Andersen, T.J., Pejrup, M., Nielsen, A.A., 2006. Long-term and high-resolution measurements of bed level changes in a temperate, microtidal coastal lagoon. Mar. Geol. 226, 115–125. doi:10.1016/j.margeo.2005.09.016

Anderson, M.E., Smith, J.M., McKay, S.K., 2011. Wave dissipation by vegetation. Coastal and Hydraulics Engineering Technical Note ERDC/CHL CHETN-I-82.U.S. Army Engineer Research and Development Center, Vicksburg, MS.

Anthony, E.J., Gratiot, N., 2012. Coastal engineering and large-scale mangrove destruction in Guyana, South America: Averting an environmental catastrophe in the making. Ecol. Eng. 47, 268–273. doi:10.1016/j.ecoleng.2012.07.005

Arnaud, G., Mory, M., Abadie, S., Cassen, M., 2009. Use of a resistive rods network to monitor bathymetric evolution in the surf/swash zone. J. Coast. Res. 1781–1785.

Augustin, L.N., Irish, J.L., Lynett, P., 2009. Laboratory and numerical studies of wave damping by emergent and near-emergent wetland vegetation. Coast. Eng. 56, 332–340.

Bakker, J.P., 2012. Restoration of Salt Marshes, in: Restoration Ecology: The New Frontier. pp. 248–262.

Bakker, J.P., Esselink, P., Dijkema, K.S., Van Duin, W.E., De Jong, D.J., 2002. Restoration of salt marshes in the Netherlands. Hydrobiologia 478, 29–51. doi:10.1023/A:1021066311728

Balke, T., Bouma, T.J., Herman, P.M.J., Horstman, E.M., Sudtongkong, C., Webb, E.L., 2013a. Cross-shore gradients of physical disturbance in mangroves: Implications for seedling establishment. Biogeosciences 10, 5411–5419. doi:10.5194/bg-10-5411-2013

Balke, T., Bouma, T.J., Horstman, E.M., Webb, E.L., Erftemeijer, P.L.A., Herman, P.M.J., 2011. Windows of opportunity: Thresholds to mangrove seedling establishment on tidal flats. Mar. Ecol. Prog. Ser. 440, 1–9.

Balke, T., Herman, P.M.J., Bouma, T.J., 2014. Critical transitions in disturbance-driven ecosystems: Identifying windows of opportunity for recovery. J. Ecol. 102, 700–708. doi:10.1111/1365-2745.12241

Balke, T., Webb, E.L., van den Elzen, E., Galli, D., Herman, P.M.J., Bouma, T.J., 2013b. Seedling establishment in a dynamic sedimentary environment: A conceptual framework using mangroves. J. Appl. Ecol. 50, 740–747. doi:10.1111/1365-2664.12067

Barbier, E.B., Koch, E.W., Silliman, B.R., Hacker, S.D., Wolanski, E., Primavera, J., Granek, E.F., Polasky, S., Aswani, S., Cramer, L.A., Stoms, D.M., Kennedy, C.J., Bael, D., Kappel, C.V., Perillo, G.M.E., Reed, D.J., 2008. Coastal ecosystem-based management with nonlinear ecological functions and values. Science 319, 321–323. doi:10.1126/science.1150349

Bearman, J.A., Friedrichs, C.T., Jaffe, B.E., Foxgrover, A.C., 2010. Spatial trends in tidal flat shape and associated environmental parameters in South San Francisco Bay. J. Coast. Res. 26, 342–349.

Booij, N., Ris, R.C., Holthuijsen, L.H., 1999. A third-generation wave model for coastal regions 1. Model description and validation. J. Geophys. Res. C Oceans 104, 7649–7666.

Booth, E.G., Loheide, S.P., 2012. Hydroecological model predictions indicate wetter and more diverse soil water regimes and vegetation types following floodplain restoration. J. Geophys. Res. Biogeosciences 117. doi:10.1029/2011JG001831

Borsje, B.W., van Wesenbeeck, B.K., Dekker, F., Paalvast, P., Bouma, T.J., van Katwijk, M.M., de Vries, M.B., 2011. How ecological engineering can serve in coastal protection. Ecol. Eng. 37, 113–122.

Bouma, H., Duiker, J.M.C., De Vries, P.P., Herman, P.M.J., Wolff, W.J., 2001. Spatial pattern of early recruitment of Macoma balthica (L.) and Cerastoderma edule (L.) in relation to sediment dynamics on a highly dynamic intertidal sandflat. J. Sea Res. 45, 79–93. doi:10.1016/S1385-1101(01)00054-5

Bouma, T.J., De Vries, M.B., Low, E., Peralta, G., Tánczos, I.C., Van De Koppel, J., Herman, P.M.J., 2005. Trade-offs related to ecosystem engineering: A case study on stiffness of emerging macrophytes. Ecology 86, 2187–2199.

Bouma, T.J., Friedrichs, M., Klaassen, P., Van Wesenbeeck, B.K., Brun, F.G., Temmerman, S., Van Katwijk, M.M., Graf, G., Herman, P.M.J., 2009a. Effects of shoot stiffness, shoot size and current velocity on scouring sediment from around seedlings and propagules. Mar. Ecol. Prog. Ser. 388, 293–297. doi:10.3354/meps08130

Bouma, T.J., Friedrichs, M., Van Wesenbeeck, B.K., Temmerman, S., Graf, G., Herman, P.M.J., 2009b. Density-dependent linkage of scale-dependent feedbacks: A flume study on the intertidal macrophyte Spartina anglica. Oikos 118, 260–268. doi:10.1111/j.1600-0706.2008.16892.x

Bouma, T.J., van Belzen, J., Balke, T., Zhu, Z., Airoldi, L., Blight, A.J., Davies, A.J., Galvan, C., Hawkins, S.J., Hoggart, S.P.G., Lara, J.L., Losada, I.J., Maza, M., Ondiviela, B., Skov, M.W., Strain, E.M., Thompson, R.C., Yang, S., Zanuttigh, B., Zhang, L., Herman, P.M.J., 2014. Identifying knowledge gaps hampering application of intertidal habitats in coastal protection: Opportunities & steps to take. Coast. Eng. 87, 147–157. doi:10.1016/j.coastaleng.2013.11.014

Bradley, K., Houser, C., 2009. Relative velocity of seagrass blades: Implications for wave attenuation in low-energy environments. J. Geophys. Res. F Earth Surf. 114.

Cahoon, D.R., Lynch, J.C., Hensel, P., Boumans, R., Perez, B.C., Segura, B., Day Jr., J.W., 2002. High-precision measurements of wetland sediment elevation: I. Recent improvements to the sedimentation-erosion table. J. Sediment. Res. 72, 730–733. doi:10.1306/020702720730

Callaghan, D.P., Bouma, T.J., Klaassen, P., van der Wal, D., Stive, M.J.F., Herman, P.M.J., 2010. Hydrodynamic forcing on salt-marsh development: Distinguishing the relative importance of waves and tidal flows. Estuar. Coast. Shelf Sci. 89, 73–88.

Corenblit, D., Baas, A.C.W., Bornette, G., Darrozes, J., Delmotte, S., Francis, R.A., Gurnell, A.M., Julien, F., Naiman, R.J., Steiger, J., 2011. Feedbacks between geomorphology and biota controlling Earth surface processes and landforms: A review of foundation concepts and current understandings. Earth-Sci. Rev. 106, 307–331. doi:10.1016/j.earscirev.2011.03.002

Costanza, R., D'Arge, R., De Groot, R., Farber, S., Grasso, M., Hannon, B., Limburg, K., Naeem, S., O'Neill, R.V., Paruelo, J., Raskin, R.G., Sutton, P., Van Den Belt, M., 1997. The value of the world's ecosystem services and natural capital. Nature 387, 253–260. doi:10.1038/387253a0

Coverdale, T.C., Bertness, M.D., Altieri, A.H., 2013. Regional ontogeny of new england salt marsh die-off. Conserv. Biol. 27, 1041–1048. doi:10.1111/cobi.12052

Dalrymple, R.A., Kirby, J.T., Hwang, P.A., 1984. Wave diffraction due to areas of energy dissipation. J. Waterw. Port Coast. Ocean Eng. 110, 67–79.

Day Jr., J.W., Boesch, D.F., Clairain, E.J., Kemp, G.P., Laska, S.D., Mitsch, W.J., Orth, K., Mashriqui, H., Reed, D.J., Shabman, L., Simenstad, C.A., Streever, B.J., Twilley, R.R., Watson, C.C., Wells, J.T., Whigham, D.F., 2007. Restoration of the Mississippi Delta: Lessons from Hurricanes Katrina and Rita. Science 315, 1679–1684. doi:10.1126/science.1137030

Day, J.W., Christian, R.R., Boesch, D.M., Yáñez-Arancibia, A., Morris, J., Twilley, R.R., Naylor, L., Schaffner, L., Stevenson, C., 2008. Consequences of climate change on the ecogeomorphology of coastal wetlands. Estuaries Coasts 31, 477–491. doi:10.1007/s12237-008-9047-6

Dean, R., Dalrymple, R., 1991. Water Wave Mechanics for Engineers and Scientists. Advanced Series on Ocean Engineering. World Scientific, Tokyo, vol. 2.

Delft Hydraulics, 1990. User's Manual for the Delft Hydraulics Four Quadrant Electromagnetic Liquid Velocity Meter. pp. 5

Delft Hydraulics, year unknown. Manual for Wave Height Meter. pp. 2

Demirbilek Z., Dalrymple R.A., Sorenson R.M., Thompson E.F., Weggel J.R., 1996. Water waves. in: Heggen RJ (ed) Hydrology handbook. ASCE, New York, pp. 627−720

Dijkstra, J.T., Uittenbogaard, R.E., 2010. Modeling the interaction between flow and highly flexible aquatic vegetation. Water Resour. Res. 46.

Donat, M.G., Renggli, D., Wild, S., Alexander, L.V., Leckebusch, G.C., Ulbrich, U., 2011. Reanalysis suggests long-term upward trends in European storminess since 1871. Geophys. Res. Lett. 38. doi:10.1029/2011GL047995

Doody, J.P., 2004. "Coastal squeeze" - An historical perspective. J. Coast. Conserv. 10, 129–138.

Eisma, D., 1998. Intertidal Deposits: River Mouths, Tidal Flats, and Coastal Lagoons, CRC Marine Science. CRC Press, Boca raton.

Ellison, A.M., 2000. Mangrove Restoration: Do We Know Enough? Restor. Ecol. 8, 219–229. doi:10.1046/j.1526-100x.2000.80033.x

Fagherazzi, S., Carniello, L., D'Alpaos, L., Defina, A., 2006. Critical bifurcation of shallow microtidal landforms in tidal flats and salt marshes. Proc. Natl. Acad. Sci. U. S. A. 103, 8337–8341.

Fagherazzi, S., Kirwan, M.L., Mudd, S.M., Guntenspergen, G.R., Temmerman, S., D'Alpaos, A., Van De Koppel, J., Rybczyk, J.M., Reyes, E., Craft, C., Clough, J., 2012. Numerical models of salt marsh evolution: Ecological, geomorphic, and climatic factors. Rev. Geophys. 50. doi:10.1029/2011RG000359

Fagherazzi, S., Mariotti, G., Banks, A.T., Morgan, E.J., Fulweiler, R.W., 2014. The relationships among hydrodynamics, sediment distribution, and chlorophyll in a mesotidal estuary. Estuar. Coast. Shelf Sci. 144, 54–64. doi:10.1016/j.ecss.2014.04.003

Fagherazzi, S., Wiberg, P.L., 2009. Importance of wind conditions, fetch, and water levels on wave-generated shear stresses in shallow intertidal basins. J. Geophys. Res. B Solid Earth 114.

Fan, D., Guo, Y., Wang, P., Shi, J.Z., 2006. Cross-shore variations in morphodynamic processes of an open-coast mudflat in the Changjiang Delta, China: With an emphasis on storm impacts. Cont. Shelf Res. 26,

517–538.

Feagin, R.A., Irish, J.L., Möller, I., Williams, A.M., Colón-Rivera, R.J., Mousavi, M.E., 2011. Short communication: Engineering properties of wetland plants with application to wave attenuation. Coast. Eng. 58, 251–255.

Fonstad, M.A., Dietrich, J.T., Courville, B.C., Jensen, J.L., Carbonneau, P.E., 2013. Topographic structure from motion: a new development in photogrammetric measurement. Earth Surf. Process. Landf. 38, 421–430. doi:10.1002/esp.3366

Fortin, M.-J., Dale, M.R.T., 2005. Spatial Analysis: A Guide for Ecologists. Cambridge University Press.

Foster, N.M., Hudson, M.D., Bray, S., Nicholls, R.J., 2013. Intertidal mudflat and saltmarsh conservation and sustainable use in the UK: A review. J. Environ. Manage. 126, 96–104. doi:10.1016/j.jenvman.2013.04.015

Friedrichs, C.T., 2011. 3.06 - Tidal Flat Morphodynamics: A Synthesis, in: Wolanski, E., McLusky, D. (Eds.), Treatise on Estuarine and Coastal Science. Academic Press, Waltham, pp. 137–170.

Friedrichs, C.T., Aubrey, D.G., 1996. Uniform bottom shear stress and equilibrium hyposometry of intertidal flats, in: Pattiaratchi, C. (Ed.), Coastal and Estuarine Studies. American Geophysical Union, Washington, D. C., pp. 405–429.

Friedrichs, C.T., Wright, L.D., 2004. Gravity-driven sediment transport on the continental shelf: Implications for equilibrium profiles near river mouths. Coast. Eng. 51, 795–811.

Friess, D.A., Krauss, K.W., Horstman, E.M., Balke, T., Bouma, T.J., Galli, D., Webb, E.L., 2012. Are all intertidal wetlands naturally created equal? Bottlenecks, thresholds and knowledge gaps to mangrove and saltmarsh ecosystems. Biol. Rev. 87, 346–366.

Gabet, E.J., 1998. Lateral migration and bank erosion in a saltmarsh tidal channel in San Francisco Bay, California. Estuaries 21, 745–753. doi:10.2307/1353278

Ganthy, F., Sottolichio, A., Verney, R., 2013. Seasonal modification of tidal flat sediment dynamics by seagrass meadows of Zostera noltii (Bassin d'Arcachon, France). J. Mar. Syst., XII International Symposium on Oceanography of the Bay of Biscay 109–110, Supplement, S233–S240. doi:10.1016/j.jmarsys.2011.11.027

Glenn, N.F., Spaete, L.P., Sankey, T.T., Derryberry, D.R., Hardegree, S.P., Mitchell, J., 2011. Errors in LiDAR-derived shrub height and crown area on sloped terrain. J. Arid Environ. 75, 377–382. doi:10.1016/j.jaridenv.2010.11.005

Gong, Z., Wang, Z., Stive, M.J.F., Zhang, C., Chu, A., 2012. Process-Based Morphodynamic Modeling of a Schematized Mudflat Dominated by a Long-Shore Tidal Current at the Central Jiangsu Coast, China. J. Coast. Res. 1381–1392. doi:10.2112/JCOASTRES-D-12-00001.1

Green, M.O., 2011. Very small waves and associated sediment resuspension on an estuarine intertidal flat. Estuar. Coast. Shelf Sci. 93, 449–459.

Green, M.O., Coco, G., 2014. Review of wave-driven sediment resuspension and transport in estuaries. Rev. Geophys. 52, 77–117. doi:10.1002/2013RG000437

Han, Q., Bouma, T.J., Brun, F.G., Suykerbuyk, W., Van Katwijk, M.M., 2012. Resilience of Zostera noltii to burial or erosion disturbances. Mar. Ecol. Prog. Ser. 449, 133–143. doi:10.3354/meps09532

Hasselmann, K., Barnett, T.P., Bouws, E., Carlson, H., Cartwright, D.E., Enke, K., Ewing, J.A., Gienapp, H., Hasselmann, D.E., Kruseman, P., Meerburg, A., Müller, P., Olbers, D.J., Richter, K., Sell, W., Walden, H., 1973. Measurements of wind-wave growth and swell decay during the Joint North Sea Wave Project (JONSWAP).

Henry, P.-Y., Myrhaug, D., 2013. Wave-induced drag force on vegetation under shoaling random waves. Coast. Eng. 78, 13–20.

Hu, Z., Suzuki, T., Zitman, T., Uijttewaal, W.S.J., Stive, M.J.F., 2014. Laboratory study on wave dissipation by vegetation in combined current-wave flow. Coast. Eng. 88, 131–142. doi:10.1016/j.coastaleng.2014.02.009

Huang, Z., Yao, Y., Sim, S.Y., Yao, Y., 2011. Interaction of solitary waves with emergent, rigid vegetation. Ocean Eng. 38, 1080–1088.

Hughes, R.G., Paramor, O.A.L., 2004. On the loss of saltmarshes in south-east England and methods for their restoration. J. Appl. Ecol. 41, 440–448. doi:10.1111/j.0021-8901.2004.00915.x

Hunt, S., Bryan, K.R., Mullarney, J.C., 2015. The influence of wind and waves on the existence of stable intertidal morphology in meso-tidal estuaries. Geomorphology 228, 158–174. doi:10.1016/j.geomorph.2014.09.001

Infantes, E., Orfila, A., Bouma, T.J., Simarro, G., Terrados, J., 2011. Posidonia oceanica and Cymodocea nodosa seedling tolerance to wave exposure. Limnol. Oceanogr. 56, 2223–2232.

Jadhav, R.S., Chen, Q., Smith, J.M., 2013. Spectral distribution of wave energy dissipation by salt marsh vegetation. Coast. Eng. 77, 99–107.

Jestin, H., Bassoullet, P., Le Hir, P., L'Yavanc, J., Degres, Y., 1998. Development of ALTUS, a high frequency

acoustic submersible recording altimeter to accurately monitor bed elevation and quantify deposition or erosion of sediments, in: OCEANS '98 Conference Proceedings. Presented at the OCEANS '98 Conference Proceedings, vol.1. doi: 10.1109/OCEANS.1998.725734 pp. 189–194

Johnson, J.B., Omland, K.S., 2004. Model selection in ecology and evolution. Trends Ecol. Evol. 19, 101–108. doi:10.1016/j.tree.2003.10.013

Jones, C.G., Lawton, J.H., Shachak, M., 1994. Organisms as ecosystem engineers. Oikos 69, 373–386.

Kirby, R., 2000. Practical implications of tidal flat shape. Cont. Shelf Res. 20, 1061–1077.

Kirwan, M., Temmerman, S., 2009. Coastal marsh response to historical and future sea-level acceleration. Quat. Sci. Rev. 28, 1801–1808.

Kirwan, M.L., Guntenspergen, G.R., 2012. Feedbacks between inundation, root production, and shoot growth in a rapidly submerging brackish marsh. J. Ecol. 100, 764–770. doi:10.1111/j.1365-2745.2012.01957.x

Kirwan, M.L., Guntenspergen, G.R., D'Alpaos, A., Morris, J.T., Mudd, S.M., Temmerman, S., 2010. Limits on the adaptability of coastal marshes to rising sea level. Geophys. Res. Lett. 37.

Kirwan, M.L., Megonigal, J.P., 2013. Tidal wetland stability in the face of human impacts and sea-level rise. Nature 504, 53–60. doi:10.1038/nature12856

Kirwan, M.L., Murray, A.B., Donnelly, J.P., Corbett, D.R., 2011. Rapid wetland expansion during European settlement and its implication for marsh survival under modern sediment delivery rates. Geology 39, 507–510. doi:10.1130/G31789.1

Koftis, T., Prinos, P., Stratigaki, V., 2013. Wave damping over artificial Posidonia oceanica meadow: A large-scale experimental study. Coast. Eng. 73, 71–83.

Lawler, D.M., 1991. A new technique for the automatic monitoring of erosion and deposition rates. Water Resour. Res. 27, 2125–2128. doi:10.1029/91WR01191

Lawler, D.M., 2008. Advances in the continuous monitoring of erosion and deposition dynamics: Developments and applications of the new PEEP-3T system. Geomorphology 93, 17–39. doi:10.1016/j.geomorph.2006.12.016

Le Hir, P., Roberts, W., Cazaillet, O., Christie, M., Bassoullet, P., Bacher, C., 2000. Characterization of intertidal flat hydrodynamics. Cont. Shelf Res. 20, 1433–1459.

Lewis III, R.R., 2005. Ecological engineering for successful management and restoration of mangrove forests. Ecol. Eng., Wetland creation 24, 403–418. doi:10.1016/j.ecoleng.2004.10.003

Li, C.W., Yan, K., 2007. Numerical investigation of Wave - Current - Vegetation interaction. J. Hydraul. Eng. 133, 794–803.

Li, X., Ren, L., Liu, Y., Craft, C., Mander, Ü., Yang, S., 2014. The impact of the change in vegetation structure on the ecological functions of salt marshes: The example of the Yangtze estuary. Reg. Environ. Change 14, 623–632. doi:10.1007/s10113-013-0520-9

Liu, P.L.-F., Chang, C.-W., Mei, C.C., Lomonaco, P., Martin, F.L., Maza, M., 2015. Periodic water waves through an aquatic forest. Coast. Eng. 96, 100–117. doi:10.1016/j.coastaleng.2014.11.002

Liu, X.J., Gao, S., Wang, Y.P., 2011. Modeling profile shape evolution for accreting tidal flats composed of mud and sand: A case study of the central Jiangsu coast, China. Cont. Shelf Res. 31, 1750–1760. doi:10.1016/j.csr.2011.08.002

Loon-Steensma, J.M. van, Slim, P.A., Decuyper, M., Hu, Z., 2014. Salt-marsh erosion and restoration in relation to flood protection on the Wadden Sea barrier island Terschelling. J. Coast. Conserv. 1–16. doi:10.1007/s11852-014-0326-z

Lotze, H.K., Lenihan, H.S., Bourque, B.J., Bradbury, R.H., Cooke, R.G., Kay, M.C., Kidwell, S.M., Kirby, M.X., Peterson, C.H., Jackson, J.B.C., 2006. Depletion degradation, and recovery potential of estuaries and coastal seas. Science 312, 1806–1809. doi:10.1126/science.1128035

Lowe, R.J., Falter, J.L., Koseff, J.R., Monismith, S.G., Atkinson, M.J., 2007. Spectral wave flow attenuation within submerged canopies: Implications for wave energy dissipation. J. Geophys. Res. C Oceans 112.

Lowe, R.J., Koseff, J.R., Monismith, S.G., 2005. Oscillatory flow through submerged canopies: 1. Velocity structure. J. Geophys. Res. C Oceans 110, 1–17.

Luhar, M., Coutu, S., Infantes, E., Fox, S., Nepf, H., 2010. Wave-induced velocities inside a model seagrass bed. J. Geophys. Res. C Oceans 115.

Ma, Z., Melville, D.S., Liu, J., Chen, Y., Yang, H., Ren, W., Zhang, Z., Piersma, T., Li, B., 2014. Rethinking China's new great wall. Science 346, 912–914. doi:10.1126/science.1257258

Mancini, F., Dubbini, M., Gattelli, M., Stecchi, F., Fabbri, S., Gabbianelli, G., 2013. Using Unmanned Aerial Vehicles (UAV) for High-Resolution Reconstruction of Topography: The Structure from Motion Approach on Coastal Environments. Remote Sens. 5, 6880–6898. doi:10.3390/rs5126880

Mariotti, G., Fagherazzi, S., 2010. A numerical model for the coupled long-term evolution of salt marshes and tidal flats. J. Geophys. Res. F Earth Surf. 115.

Mariotti, G., Fagherazzi, S., 2012. Wind waves on a mudflat: The influence of fetch and depth on bed shear

stresses.

Mariotti, G., Fagherazzi, S., 2013. Critical width of tidal flats triggers marsh collapse in the absence of sea-level rise. Proc. Natl. Acad. Sci. 110, 5353–5356. doi:10.1073/pnas.1219600110

Martínez, M.L., Intralawan, A., Vázquez, G., Pérez-Maqueo, O., Sutton, P., Landgrave, R., 2007. The coasts of our world: Ecological, economic and social importance. Ecol. Econ. 63, 254–272. doi:10.1016/j.ecolecon.2006.10.022

Marton, J.M., Roberts, B.J., 2014. Spatial variability of phosphorus sorption dynamics in Louisiana salt marshes. J. Geophys. Res. Biogeosciences 119, 451–465. doi:10.1002/2013JG002486

Maza, M., Lara, J.L., Losada, I.J., 2015. Tsunami wave interaction with mangrove forests: A 3-D numerical approach. Coast. Eng. 98, 33–54. doi:10.1016/j.coastaleng.2015.01.002

Mendez, F.J., Losada, I.J., 2004. An empirical model to estimate the propagation of random breaking and non-breaking waves over vegetation fields. Coast. Eng. 51, 103–118.

Mendez, F.J., Losada, I.J., Losada, M.A., 1999. Hydrodynamics induced by wind waves in a vegetation field. J. Geophys. Res. C Oceans 104, 18383–18396.

Millard, K., Redden, A.M., Webster, T., Stewart, H., 2013. Use of GIS and high resolution LiDAR in salt marsh restoration site suitability assessments in the upper Bay of Fundy, Canada. Wetl. Ecol. Manag. 21, 243–262. doi:10.1007/s11273-013-9303-9

Möller, I., Kudella, M., Rupprecht, F., Spencer, T., Paul, M., van Wesenbeeck, B.K., Wolters, G., Jensen, K., Bouma, T.J., Miranda-Lange, M., Schimmels, S., 2014. Wave attenuation over coastal salt marshes under storm surge conditions. Nat. Geosci. 7, 727–731. doi:10.1038/ngeo2251

Morison, J.R., 1950. The Force Exerted by Surface Waves on Piles. Petrol. Trans., AWME 189.

Mudd, S.M., Howell, S.M., Morris, J.T., 2009. Impact of dynamic feedbacks between sedimentation, sea-level rise, and biomass production on near-surface marsh stratigraphy and carbon accumulation. Estuar. Coast. Shelf Sci. 82, 377–389. doi:10.1016/j.ecss.2009.01.028

Murray, A.B., Knaapen, M.A.F., Tal, M., Kirwan, M.L., 2008. Biomorphodynamics: Physical-biological feedbacks that shape landscapes. Water Resour. Res. 44. doi:10.1029/2007WR006410

Nambu, R., Saito, H., Tanaka, Y., Higano, J., Kuwahara, H., 2012. Wave actions and topography determine the small-scale spatial distribution of newly settled Asari clams Ruditapes philippinarum on a tidal flat. Estuar. Coast. Shelf Sci. 99, 1–9.

Nepf, H.M., 1999. Drag, turbulence, and diffusion in flow through emergent vegetation. Water Resour. Res. 35, 479–489.

Nepf, H.M., 2004. Vegetated Flow Dynamics, in: Fagherazzi, S., Marani, M., Blum, L.K. (Eds.), Coastal and Estuarine Studies. American Geophysical Union, Washington, D. C., pp. 137–163.

Nepf, H.M., 2011. Flow Over and Through Biota, in: Wolanski, E., McLusky, D. (Eds.), Treatise on Estuarine and Coastal Science. Academic Press, Waltham, pp. 267–288.

Nepf, H.M., 2012. Flow and Transport in Regions with Aquatic Vegetation. Annu. Rev. Fluid Mech. 44, 123–142. doi:10.1146/annurev-fluid-120710-101048

Nolte, S., Koppenaal, E.C., Esselink, P., Dijkema, K.S., Schuerch, M., De Groot, A.V., Bakker, J.P., Temmerman, S., 2013. Measuring sedimentation in tidal marshes: A review on methods and their applicability in biogeomorphological studies. J. Coast. Conserv. 17, 301–325. doi:10.1007/s11852-013-0238-3

Passarelli, C., Olivier, F., Paterson, D.M., Meziane, T., Hubas, C., 2014. Organisms as cooperative ecosystem engineers in intertidal flats. J. Sea Res. 92, 92–101. doi:10.1016/j.seares.2013.07.010

Paul, M., Bouma, T.J., Amos, C.L., 2012. Wave attenuation by submerged vegetation: -combining the effect of organism traits and tidal current. Mar. Ecol. Prog. Ser. 444, 31–41.

Pawlowicz, R., Beardsley, B., Lentz, S., 2002. Classical tidal harmonic analysis including error estimates in MATLAB using T_TIDE. Comput. Geosci. 28, 929–937. doi:10.1016/S0098-3004(02)00013-4

Pendleton, L., Donato, D.C., Murray, B.C., Crooks, S., Jenkins, W.A., Sifleet, S., Craft, C., Fourqurean, J.W., Kauffman, J.B., Marbà, N., Megonigal, P., Pidgeon, E., Herr, D., Gordon, D., Baldera, A., 2012. Estimating Global "Blue Carbon" Emissions from Conversion and Degradation of Vegetated Coastal Ecosystems. PLoS ONE 7. doi:10.1371/journal.pone.0043542

Pinsky, M.L., Guannel, G., Arkema, K.K., 2013. Quantifying wave attenuation to inform coastal habitat conservation. Ecosphere 4, art95. doi:10.1890/ES13-00080.1

Pontee, N., 2013. Defining coastal squeeze: A discussion. Ocean Coast. Manag. 84, 204–207. doi:10.1016/j.ocecoaman.2013.07.010

Primavera, J.H., Esteban, J.M.A., 2008. A review of mangrove rehabilitation in the Philippines: successes, failures and future prospects. Wetl. Ecol. Manag. 16, 345–358. doi:10.1007/s11273-008-9101-y

Pritchard, D., Hogg, A.J., 2003. Cross-shore sediment transport and the equilibrium morphology of mudflats under tidal currents. J. Geophys. Res. C Oceans 108, 11–1.

Pritchard, D., Hogg, A.J., Roberts, W., 2002. Morphological modelling of intertidal mudflats: The role of cross-shore tidal currents. Cont. Shelf Res. 22, 1887–1895.

Pujol, D., Serra, T., Colomer, J., Casamitjana, X., 2013. Flow structure in canopy models dominated by progressive waves. J. Hydrol. 486, 281–292.

Richardson, A.D., Braswell, B.H., Hollinger, D.Y., Jenkins, J.P., Ollinger, S.V., 2009. Near-surface remote sensing of spatial and temporal variation in canopy phenology. Ecol. Appl. 19, 1417–1428. doi:10.1890/08-2022.1

Ridd, P.V., 1992. A sediment level sensor for erosion and siltation detection. Estuar. Coast. Shelf Sci. 35, 353–362.

Ridderinkhof, H., van der Ham, R., van der Lee, W., 2000. Temporal variations in concentration and transport of suspended sediments in a channel–flat system in the Ems-Dollard estuary. Cont. Shelf Res. 20, 1479–1493. doi:10.1016/S0278-4343(00)00033-9

Roberts, W., Le Hir, P., Whitehouse, R.J.S., 2000. Investigation using simple mathematical models of the effect of tidal currents and waves on the profile shape of intertidal mudflats. Cont. Shelf Res. 20, 1079–1097.

Roelvink, J.A., Reniers, A.J.H.M., 2011. A GUIDE TO MODELLING COASTAL MORPHOLOGY. World Scientific Publishing Company, Singapore.

Saintilan, N., Wilson, N.C., Rogers, K., Rajkaran, A., Krauss, K.W., 2014. Mangrove expansion and salt marsh decline at mangrove poleward limits. Glob. Change Biol. 20, 147–157. doi:10.1111/gcb.12341

Schoneboom, T., Aberle, J., Dittrich, A., 2011. Spatial Variability, Mean Drag Forces, and Drag Coefficients in an Array of Rigid Cylinders, in: Rowinski, P. (Ed.), Experimental Methods in Hydraulic Research, Geoplanet: Earth and Planetary Sciences. Springer Berlin Heidelberg, pp. 255–265.

Schwarz, C., Ye, Q.H., Van Der Wal, D., Zhang, L.Q., Bouma, T., Ysebaert, T., Herman, P.M.J., 2014. Impacts of salt marsh plants on tidal channel initiation and inheritance. J. Geophys. Res. F Earth Surf. 119, 385–400. doi:10.1002/2013JF002900

Schwarz, C., Ysebaert, T., Zhu, Z., Zhang, L., Bouma, T.J., Herman, P.M.J., 2011. Abiotic factors governing the establishment and expansion of two salt marsh plants in the Yangtze Estuary, China. Wetlands 31, 1011–1021. doi:10.1007/s13157-011-0212-5

Shi, B.W., Yang, S.L., Wang, Y.P., Bouma, T.J., Zhu, Q., 2012. Relating accretion and erosion at an exposed tidal wetland to the bottom shear stress of combined current–wave action. Geomorphology 138, 380–389.

Silva, T.A., Freitas, M.C., Andrade, C., Taborda, R., Freire, P., Schmidt, S., Antunes, C., 2013. Geomorphological response of the salt-marshes in the Tagus estuary to sea level rise. J. Coast. Res. 582–587. doi:10.2112/SI65-099

Small, C., Nicholls, R.J., 2003. A global analysis of human settlement in coastal zones. J. Coast. Res. 19, 584–599.

Soulsby, R., 1997. Dynamics of marine sands: a manual for practical applications. Telford, London.

Soulsby, RL 1995. Bed shear-stresses due to combined waves and currents. in: Stive, M.J.F. De Vriend, HJ, Fredsøe, J, Hamm, L, Soulsby, RL, Teisson, C and Winterwerp, JC, (Eds.), Advances in Coastal Morphodynamics, Delft Hydraulics, Delft, NL, pp. 4-20 to 4-23

Spencer, K.L., Harvey, G.L., 2012. Understanding system disturbance and ecosystem services in restored salt-marshes: Integrating physical and biogeochemical processes. Estuar. Coast. Shelf Sci. 106, 23–32. doi:10.1016/j.ecss.2012.04.020

Stive, M.J.F., Wang, Z.B., 2003. Chapter 13 Morphodynamic modeling of tidal basins and coastal inlets, in: V.C. Lakhan (Ed.), Elsevier Oceanography Series, Advances in Coastal Modeling. Elsevier, pp. 367–392.

Stive, M.J.F.; Wang, Z.B.; Capobianco, M.; Ruol, P.; Buijsman, M.C., 1998. Morphodynamics of a tidal lagoon and the adjacent coast, in: Dronkers, J.; Scheffers, M, (Eds.) Physics of estuaries and coastal seas: proceedings of the 8th International Biennial Conference on physics of estuaries and coastal seas, The Hague, Netherlands, AA Balkema: Rotterdam, pp 397-407

Stokes, D.J., Healy, T.R., Cooke, P.J., 2010. Expansion Dynamics of Monospecific, Temperate Mangroves and Sedimentation in Two Embayments of a Barrier-Enclosed Lagoon, Tauranga Harbour, New Zealand. J. Coast. Res. 113–122. doi:10.2112/08-1043.1

Stratigaki, V., Manca, E., Prinos, P., Losada, I.J., Lara, J.L., Sclavo, M., Amos, C.L., Cáceres, I., Sánchez-Arcilla, A., 2011. Large-scale experiments on wave propagation over Posidonia oceanica. J. Hydraul. Res. 49, 31–43.

Sumer, B.M., Fredsøe, J., 2006. Advanced Series on Ocean Engineering, Volume 12: Hydrodynamics around Cylindrical Structures. revised ed. World Scientific Pub., London, pp. 157-160.

Suzuki, T., Zijlema, M., Burger, B., Meijer, M.C., Narayan, S., 2011. Wave dissipation by vegetation with layer schematization in SWAN. Coast. Eng. 59, 64–71.

Tambroni, N., Seminara, G., 2012. A one-dimensional eco-geomorphic model of marsh response to sea level rise: Wind effects, dynamics of the marsh border and equilibrium. J. Geophys. Res. Earth Surf. 117. doi:10.1029/2012JF002363

Tanino, Y., Nepf, H.M., 2008. Laboratory investigation of mean drag in a random array of rigid, emergent cylin-

ders. J. Hydraul. Eng. 134, 34–41.

Temmerman, S., Bouma, T.J., Van de Koppel, J., Van der Wal, D., De Vries, M.B., Herman, P.M.J., 2007. Vegetation Causes Channel Erosion in a Tidal Landscape. Geology 35, 631–634.

Temmerman, S., Meire, P., Bouma, T.J., Herman, P.M.J., Ysebaert, T., De Vriend, H.J., 2013. Ecosystem-based coastal defence in the face of global change. Nature 504, 79–83. doi:10.1038/nature12859

Tucker, M.J., Pitt, E.G., 2001. Waves in Ocean Engineering, 1 edition. ed. Elsevier Science, Amsterdam ; New York.

Van de Koppel, J., van der Wal, D., Bakker, J.P., Herman, P.M., 2005. Self-organization and vegetation collapse in salt marsh ecosystems. Am. Nat. 165, E1–12.

Van der Wegen, M., Jaffe, B.E., 2014. Processes governing decadal-scale depositional narrowing of the major tidal channel in San Pablo Bay, California, USA. J. Geophys. Res. Earth Surf. 119, 2013JF002824. doi:10.1002/2013JF002824

Van Kessel, T., Vanlede, J., de Kok, J., 2011. Development of a mud transport model for the Scheldt estuary. Cont. Shelf Res. 31, S165–S181. doi:10.1016/j.csr.2010.12.006

Van Rijn, L.C., 2007. Unified view of sediment transport by currents and waves. I: Initiation of motion, bed roughness, and bed-load transport. J. Hydraul. Eng. 133, 649–667. doi:10.1061/(ASCE)0733-9429(2007)133:6(649)

Van Slobbe, E., de Vriend, H.J., Aarninkhof, S., Lulofs, K., de Vries, M., Dircke, P., 2013. Building with Nature: In search of resilient storm surge protection strategies. Nat. Hazards 65, 947–966. doi:10.1007/s11069-012-0342-y

Van Wijnen, H.J., Bakker, J.P., 2001. Long-term surface elevation change in salt marshes: A prediction of marsh response to future sea-level rise. Estuar. Coast. Shelf Sci. 52, 381–390. doi:10.1006/ecss.2000.0744

Viles, H.A., Naylor, L.A., Carter, N.E.A., Chaput, D., 2008. Biogeomorphological disturbance regimes: Progress in linking ecological and geomorphological systems. Earth Surf. Process. Landf. 33, 1419–1435. doi:10.1002/esp.1717

Waeles, B., Le Hir, P., Silva Jacinto, R., 2004. Cross-shore morphodynamical modelling of an intertidal mudflat. Comptes Rendus - Geosci. 336, 1025–1033.

Wang, C., Temmerman, S., 2013. Does bio-geomorphic feedback lead to abrupt shifts between alternative landscape states? An empirical study on intertidal flats and marshes. J. Geophys. Res. Earth Surf. n/a–n/a. doi:10.1002/jgrf.20027

Wang, Z.B., Karssen, B., Fokkink, R.J.; Langerak, A.; (1998). A dynamic-empirical model for estuarine morphology, in: Dronkers, J.; Scheffers, M, (Eds.) Physics of estuaries and coastal seas: proceedings of the 8th International Biennial Conference on physics of estuaries and coastal seas, The Hague, Netherlands, AA Balkema: Rotterdam, pp 279-286

Wang, Z.B., Townend, I.H., 2012. Influence of the nodal tide on the morphological response of estuaries. Mar. Geol. 291-294, 73–82. doi:10.1016/j.margeo.2011.11.007

Wang, Z.B., Vriend, H. de, Stive, M., Townend, I., 2007. On the parameter setting of semi-empirical long-term morphological models for estuaries and tidal lagoons, in: River, Coastal and Estuarine Morphodynamics: RCEM 2007, Two Volume Set. Taylor & Francis, pp. 103–111.

Waterman, R.E., Stive, M.J.F., Vrijling, J.K., TU Delft: Civil Engineering and Geosciences: Hydraulic Engineering, TU Delft, Delft University of Technology, 2010. Integrated coastal policy via Building with Nature. PhD thesis

Wiehe, P.O., 1935. A Quantitative Study of the Influence of Tide Upon Populations of Salicornia Europea. J. Ecol. 23, 323. doi:10.2307/2256124

Winterwerp, J.C. and Van Kesteren, W.G. 2004, Introduction to the physics of cohesive sediment dynamics in the marine environment Developments in Sedimentology,56. Elsevier.

Winterwerp, J.C., Erftemeijer, P.L.A., Suryadiputra, N., Van Eijk, P., Zhang, L., 2013. Defining eco-morphodynamic requirements for rehabilitating eroding mangrove-mud coasts. Wetlands 33, 515–526. doi:10.1007/s13157-013-0409-x

Wolters, M., Garbutt, A., Bakker, J.P., 2005. Salt-marsh restoration: Evaluating the success of de-embankments in north-west Europe. Biol. Conserv. 123, 249–268. doi:10.1016/j.biocon.2004.11.013

Wolters, M., Garbutt, A., Bekker, R.M., Bakker, J.P., Carey, P.D., 2008. Restoration of salt-marsh vegetation in relation to site suitability, species pool and dispersal traits. J. Appl. Ecol. 45, 904–912. doi:10.1111/j.1365-2664.2008.01453.x

Woodruff, J.D., Irish, J.L., Camargo, S.J., 2013. Coastal flooding by tropical cyclones and sea-level rise. Nature 504, 44–52. doi:10.1038/nature12855

Yang, S. L., Friedrichs, C.T., Shi, Z., Ding, P.-X., Zhu, J., Zhao, Q.-Y., 2003. Morphological Response of Tidal Marshes, Flats and Channels of the Outer Yangtze River Mouth to a Major Storm. Estuaries 26, 1416–1425.

Yang, S.L., Li, H., Ysebaert, T., Bouma, T.J., Zhang, W.X., Wang, Y.Y., Li, P., Li, M., Ding, P.X., 2008. Spatial

and temporal variations in sediment grain size in tidal wetlands, Yangtze Delta: On the role of physical and biotic controls. Estuar. Coast. Shelf Sci. 77, 657–671.

Yang, S.L., Li, M., Dai, S.B., Liu, Z., Zhang, J., Ding, P.X., 2006. Drastic decrease in sediment supply from the Yangtze River and its challenge to coastal wetland management. Geophys. Res. Lett. 33.

Yang, S.L., Shi, B.W., Bouma, T.J., Ysebaert, T., Luo, X.X., 2012. Wave Attenuation at a Salt Marsh Margin: A Case Study of an Exposed Coast on the Yangtze Estuary. Estuaries Coasts 35, 169–182.

Ysebaert, T., Yang, S.L., Zhang, L., He, Q., Bouma, T.J., Herman, P.M.J., 2011. Wave attenuation by two contrasting ecosystem engineering salt marsh macrophytes in the intertidal pioneer zone. Wetlands 31, 1043–1054.

Zhu, Q., Yang, S., Ma, Y., 2014. Intra-tidal sedimentary processes associated with combined wave–current action on an exposed, erosional mudflat, southeastern Yangtze River Delta, China. Mar. Geol. 347, 95–106. doi:10.1016/j.margeo.2013.11.005

Zhu, Z., Bouma, T.J., Ysebaert, T., Zhang, L., Herman, P.M.J., 2014. Seed arrival and persistence at the tidal mudflat: Identifying key processes for pioneer seedling establishment in salt marshes. Mar. Ecol. Prog. Ser. 513, 97–109. doi:10.3354/meps10920

Acknowledgements

At the end of my PhD days, I feel grateful for many people who have helped me during this journey.

Frist of all, I want to give my gratitude to the promoter Marcel Stive, who gave me the opportunity to pursue my PhD and has been fully supportive ever since. I still remember that it was right before the Chinese New Year 2010 when I received the admission letter from Marcel to come to Delft, which was one of the happiest moments in my family. During my stay in Delft, his guidance, trust and patience have helped me to overcome the difficulties on the way of my PhD.

My gratitude also goes to Tjeerd Bouma at NIOZ, who is also a promoter of this thesis. He is the first researcher who found the value in the 'computer-game-type' marsh dynamic model, which was built at the beginning of my PhD. He taught me how it can become a useful tool for marsh evolution studies. Although this goal is yet to be achieved, the efforts made in this direction have greatly contributed to the current thesis. During my PhD journey, he brought me to world of coastal ecosystem studies with passion and inspiration.

I want to thank Zheng Bing Wang as my third promoter. He has kept an eye on my progress since I started. Through the countless meetings we had during my PhD, he contributed greatly in shaping the current thesis. Specially, his advice on the morphological modeling is the foundation of the Chapter 5 in this thesis.

Tjerk Zitman provided me unlimited support with mathematics and modeling, which made many studies in this thesis possible. As my daily supervisor, he has always been kind and patient. His efforts in revising and translating my manuscripts are also deeply appreciated.

I thank Wim Uijttewaal and Tomohiro Suzuki for their sharpness in our discussions related to the laboratory work (Chapter 2). With their help, the publication process of my first journal article was surprisingly pleasant.

I am lucky to have so many nice colleagues at TU Delft. Special thanks go to my officemate Vana Tsimopoulou and Jan van Overeem, who created a friendly atmosphere in the office and made my PhD life easier. I thank Vana and her family for hosting me in Greece, which

opened my eyes to the Greek culture and the kindness of Greek people. I also thank Marcel Zijlema, Dirk Rijnsdorp, Peng Yao, Min Su, Bram van Prooijen, Cynthia Maan, Sierd de Vries, Matthieu de Schipper, Judith Bosboom, Xuexue Chen, Wei Li, Saulo Meirelles Nunes Da Rocha, Max Radermacher, Wim Kanning, Pieter Smit and James Salmon for discussing on scientific and non-scientific topics. I hope we can keep in touch in the future. Special thanks goes to Mariette van Tilburg for revising my manuscripts from time to time and translating the abstract in this thesis into Dutch.

I also had great colleagues at NIOZ in Yerseke. I thank Peter Herman for letting me work at NIOZ during my PhD. I also thank Jim van Belzen, Daphne van der Wal and Thorsten Balke for their inspiration in the ecology related studies. Big thanks go to Lennart van IJzerloo and Jeroen van Dalen for their great help in the field work, which was very much appreciated. I am deeply grateful to my fellow PhD students at NIOZ: Cheng Hui, Zhigang Ma, Zhenchang Zhu, Qin Zhu and many others who lived in the 'keete'. Their hospitality has been a great comfort after a laborious field trip.

Thanks to Qinghua Ye and Arjen Luijendijk at Deltares, who help me to have a quick start of my PhD.

I want to thank Wiebe de Boer, Joao Mil-Homens and Zhan Luo as my dearest friends in NL, who have supported me through the hardest days and brought great fun into my PhD life.

感谢父母亲的关心，理解及支持。你们是我前进的不竭动力。你们一直盼望早日回家，我却不能在家里陪伴你们，十分愧疚。希望在以后的日子里，能有更多的时间和你们在一起。

南洋，非常幸运有你一路相伴，你的奉献无法用语言描述。美好未来就在眼前，我们共同来开拓。

Zhan Hu

04-Jan-2015

Curriculum Vitae

Zhan Hu was born on 30th of April 1986 in Hubei province, central of China. He graduated from a local high school and started studying Hydraulic Engineering at Hohai University (Nanjing) in 2005. In 2009, he obtained Bachelor of Engineering degree and continued his master degree study in the Department of Ports, Water ways and Coastal Engineering at the same university. In Sep 2010, he received a funding from the China Scholarship Council and started working as a PhD students in Coastal Engineering at TU Delft following the guidance of Prof. Marcel Stive. At the beginning phase of his PhD, he became interested in the study of saltmarshes and tidal flats. Because of such an interest, he was introduced to Prof. Tjeerd Bouma at Royal Netherlands Institute for Sea Research (NIOZ) in Yerseke for collaborative studies. At NIOZ, he participated in two research projects, which constitute a large part of this thesis. After his PhD, he plans to work as a researcher in estuarine and coastal science. Email: zhan.hu@tudelft.nl; huzhan682@gmail.com

List of Publications

Journal Articles - First author

Hu, Z., Suzuki, T., Zitman, T., Uijttewaal, W.S.J., Stive, M.J.F., 2014. Laboratory study on wave dissipation by vegetation in combined current-wave flow. Coast. Eng. 88, 131–142. doi:10.1016/j.coastaleng.2014.02.009

Hu, Z., Lenting, W., van der Wal, D., Bouma, T.J., Continuous monitoring of short-term bed-level dynamics on an intertidal flat: introducing a novel stand-alone high-resolution SED-sensor. Accepted for publication in *Geomorphology.* doi:10.1016/j.geomorph. 2015.05.027

Hu, Z., van Belzen, J., van der Wal, D., Balke, T., Wang, Z.B., Stive, M.J.F., Bouma, T.J., Windows of Opportunity for saltmarsh vegetation establishment on bare tidal flats: the importance of temporal and spatial varia-bility in hydrodynamic forcing. *Submitted*

Hu, Z., Wang, Z.B., Zitman, T., Stive, M.J.F., Bouma, T.J., Predicting long-term and short-term tidal flat morphodynamics using a dynamic equilibrium theory. *Submitted*

Journal Articles - Co-author

Loon-Steensma, J.M. van, Slim, P.A., Decuyper, M., Hu, Z., 2014. Salt-marsh erosion and restoration in relation to flood protection on the Wadden Sea barrier island Terschelling. J. Coast. Conserv. 1–16. doi:10.1007/s11852-014-0326-z

Conference proceedings and abstracts

Hu, Z., Stive, M.J.F., Zitman, T.J., Ye, Q.H., Wang, Z.B., Luijendijk, A., Gong, Z., Suzuki, T., 2011. Interaction between hydrodynamics and salt marsh dynamics: An example from Jiangsu coast. Proc, APAC 2011 - The 6th International Conference on Asian and Pacific Coasts, Hong Kong, posters

Hu, Z., Stive, M.J.F., Zitman, T., Suzuki, T., 2012. Drag coefficient of vegetation in flow modeling. Proc, ICCE 2012 - 33rd International Conference on Coastal Engineering, Santander, posters. doi:10.9753/icce.v33.posters.4

Hu, Z., Suzuki, T., Zitman, T., Uijttewaal, W.S.J., Stive, M.J.F., 2013. Laboratory study on wave dissipation by vegetation in a combined current-wave flow. Proc, EMI 2013 – Engineering Mechanics Institute Conference, oral presentation.

Hu, Z., Bouma, T.J., Zitman, T., Wang, Z.B., Stive, M.J.F., 2013. Non-hydrostatic wave modeling and field measurements on a Western Scheldt tidal flat. Proc, ECSA 2013 – 53rd Estuarine & Coastal Sciences Association Conference, posters.

Hu, Z., Suzuki, T., 2014. Wave dissipation by vegetation in combined current-wave flow. NCK-days2014 Abstract, oral presentation.